Stress Analysis of Metal Cutting Tools

by

Girma Jemal

B. Tech (Honours), Mechanical Engineering

University of Calicut, India

A THESIS SUBMITTED IN PARTIAL FULFILMENT OF

THE REQUIREMENTS FOR THE DEGREE OF

MASTER OF APPLIED SCIENCE

in

THE FACULTY OF GRADUATE STUDIES

MECHANICAL ENGINEERING

We accept this thesis as conforming
to the required standard

THE UNIVERSITY OF BRITISH COLUMBIA

April 1992

In presenting this thesis in partial fulfilment of the requirements for an advanced degree at the University of British Columbia, I agree that the Library shall make it freely available for reference and study. I further agree that permission for extensive copying of this thesis for scholarly purposes may be granted by the head of my department or by his or her representatives. It is understood that copying or publication of this thesis for financial gain shall not be allowed without my written permission.

(Sig

Department of Mechanical Eng

The University of British Columbia
Vancouver, Canada

Date April 23, 1992

DE-6 (2/88)

Abstract

Metal cutting tools experience cutting forces distributed over a small chip-tool contact area. When the magnitude of the stresses induced by the cutting forces exceeds the tool material fatigue strength, failure of the cutting tool results. In this thesis, stress analysis in cutting tools is presented in order to predict the location and modes of tool failures.

The stress analysis of cutting tools is presented using both analytical and numerical (Finite Element) based methods. First, various cutting force distributions on the rake face of the tool and analytical cutting tool stress solutions available in the literature are surveyed. It is then shown that the previous analytical solutions are incorrect because they directly applied the infinite wedge solution to determine stresses in the loaded region of the cutting tool. In this thesis, the tool and the boundary stresses are considered both in the loaded and free region. For a polynomial boundary stresses on the rake face and zero boundary stresses on the flank face, the stresses in a two-dimensional cutting tool are determined using the infinite wedge solution. The analytical cutting tool stress distributions obtained agrees well with finite element solutions and published photoelastic experimental stress distributions. From the stress distribution obtained, it is shown that the critical maximum tensile stress occurs at the end of chip-tool contact and it results in initiation of cracks and final fracture of the whole loaded region. The critical maximum compressive stress occurs on the flank face close to the cutting edge which results on cutting edge permanent deformation. The critical maximum shear stress occurs at the cutting edge and it results in cutting edge chipping.

The possible extension of the two-dimensional solution to determine stresses in

end mill flutes is considered. A comparison of a finite element solution of an end mill flute and the two-dimensional solution obtained above (for the same wedge angle and boundary load distribution) shows agreement at the cutting edge while at the end of chip-tool contact the two-dimensional solution gives an upper bound estimate. Thus the conclusions reached for tool failure in the loaded region from the two-dimensional solution is also applicable in end mill flutes. At the end mill shank, stress predictions using a cantilevered beam solution agrees with a finite element solution. The stress distribution shows shank fracture either at the fixed end of the end mill where it is attached to the chuck or at the flute section closest to the circular portion of the end mill.

In this study for both orthogonal cutting tools and end mills, good correlation is obtained between predicted and observed in-service cutting tool failures. Therefore, the proposed cutting tool stress analysis approach may be recommended for cutting tool design and selection of optimum machining conditions.

Contents

List of Figures

Nomenclature

a	distane from the fixed end of an end mill to force F, mm
a_i, b_i, c_i, d_i	stress distribution constants
b	width of cut, mm
c	end mill flute axial length, mm
d	cutter diameter, mm
d_e	equivalent cutter diameter, mm
δF_t	tangential elemental forces, N
δF_r	radial elemental forces, N
δz	axial element length, mm
f	feed per tooth, mm/tooth
f_σ	fringe constant
F	resultant cutting force in an end mill, N
F_s	shear force on the rake face, kg
F_n	normal force on the rake face, kg
$F.S$	factor of safety
h	tool thickness, mm
k	yield shear strength
K_t	tangential force constant, MPa
K_r	radial force constant, (-)
l_c	contact length, mm
M	bending moment at the shank, $kN - mm$
n	exponent of the parabolic boundary load distribution
N_i	polynomial normal stress distribution coefficients
N_{ri}	rake face polynomial normal stress distribution coefficients
p	hydrostatic pressure
P	resultant cutting force at the cutting edge
(r, θ)	polar coordinate of any point in the cutting wedge
R_i	polynomial radial stress distribution coefficients
S_{ri}	rake face polynomial shear stress distribution coefficients

S_i	polynomial shear stress distribution coefficients
SI	difference of maximum and minimum principal stresses
S_y	tensile yield strength
S_{ut}	ultimate tensile strength, MPa
S_{uc}	ultimate compressive strength, MPa
t	depth of cut, mm
T	cutting torque on end mill, $kN - mm$
w	axial depth of cut, mm
x	rake distance from cutting edge, mm

Greek Symbols

α	wedge angle
β	friction angle
γ	rake angle
θ	angle between finished surface and axial cutting edge element
λ	angle between wedge axis of symmetry and force P
μ	friction coefficient
σ	normal stress on the rake face, kg/mm^2
σ_1	maximum principal stress, kg/mm^2
σ_3	minimum principal stress, kg/mm^2
σ_o	normal boundary stress at the cutting edge
σ_r	radial normal stress in polar coordinate
σ_x	normal stress in the x-direction
σ_y	normal stress in the y-direction
σ_θ	tangential normal stress in polar coordinate
σ_{av}	average normal stress on the rake face
σ_{eq}	equivalent stress
τ	shear stress on the rake face, kg/mm^2
τ_o	shear boundary stress at the cutting edge
τ_{av}	average shear stress on the rake face
$\tau_{r\theta}$	shear stress in polar coordinate
τ_{xy}	shear stress in rectangular coordinate
ϕ	angle between σ_1 and x-axis; swept angle
ϕ	angle between α-line and x-axis
ψ	stress function; helix angle

Acknowledgement

I like to express my deep gratitude to Professor Douglas P. Romilly and Professor Yusuf Altintas for their guidance and advice during all stages of this project. I also want to thank Professor I. Yellowley for the helpful discussions.

My thanks are also extended to Mr. Gerry Rohling for his assistance with the computers.

I want also to thank my family and friends for their moral and emotional support.

Finally, I want to thank CIDA for its financial support during my stay at UBC.

Chapter 1

Introduction

Design and failure analysis of cutting tools and selection of optimum cutting conditions require knowledge of the stress distribution in the cutting tools. The stress analysis approach used to determine the stresses depend on where the stress predictions are required. When the stresses far from the cutting edge (i.e. at the shank) are required, beam equations with a concentrated load at the cutting edge can be used. When the stresses outside the loaded region within the wedge shape are needed, an elasticity solution with a concentrated load at the cutting edge could be used. However, when the stresses within the loaded region must be predicted then the actual load distribution along tool-chip contact should be used in the elasticity solution. The boundary load distributions on cutting tools are determined using one or more of the following techniques:

- Split-tool method,
- Photoelasticity,
- Slip-line solution.

Once the boundary load distribution is determined using one of the methods listed above, the stresses within the cutting tool may be determined either:

- Analytically, or
- Numerically (Finite Element Method or Mellin Transform).

The analytical solution for a concentrated load at the cutting edge is based on the elasticity solution given by Frocht [1]. The analytical solution for the distributed load along tool-chip contact is based on Michell's [4] general stress function for two-dimensional problems which was subsequently applied to an *infinite* wedge problem by Timoshenko [5]. Archibald [6], Betaneli [7], and others applied the *infinite* wedge solution to determine the stress distribution in the *finite* cutting tool, i.e. they assumed the infinite wedge solution to be applicable to determine stresses in two-dimensional cutting tools.

For a given cutting tool geometry and boundary load distribution, numerical methods could be used to determine the stress distribution in a cutting tool. The two numerical methods used in the stress analysis of cutting tools are the Mellin Transform and the Finite Element Method (FEM). The Mellin Transform method is described by Tranter [9], and cutting tool stress solutions using this method are given by Thomason [10].

From the discussion above, the analytical approach available to determine the stresses in the loaded region of a cutting tool is based on the assumption that the infinite wedge solution can be applied to determine the stresses in the finite cutting tool. It is important to verify this assumption because the solutions obtained by using this approach may sometimes lead to incorrect conclusions. To critically investigate

this assumption and to conclude whether and under what conditions this approach could be applied is the purpose of the first phase of this work.

In the second phase of this work, the critical regions of cutting tools where breakage is likely to occur will be predicted. For this an orthogonal cutting tool and an end mill will be considered. Analytical methods are first used to predict the critical stresses then these solutions will be verified with numerical methods. This verification is useful to indicate whether analytical solutions can be applied in cutting tool failure analysis.

A brief description of the contents of the chapters which follow are given below. The principles of the experimental methods used to determine the boundary load distribution in cutting, and some results by previous workers of these distributions are discussed in Section 2.3. In Section 2.4 and 2.5 the analytical stress equations and the solutions obtained by previous workers are presented.

In Section 3.2 the method for calculationg stresses in a cutting tool are calculated for a general boundary load distribution is shown. Section 3.4 gives the finite element solution for the low speed photoelastic boundary load distribution. Finally in this chapter previous analytical solutions and finite element solutions will be compared, and the types of load distributions that the analytical solutions may be used will be identified.

Analytical and finite element solutions will be compared in Chapter 4 for the types of load distributions where the analytical solution may be applied . These results will also be compared to previous experimental results for similar boundary conditions. In Section 4.5 the critical regions in two-dimensional cutting tools and their modes of failure will be determined.

In Chapter 5 the stress analysis of an end mill is presented. The critical regions for breakage of an end mill is shown. The possibility of using a simpler analytical solution to determine the stresses in these critical region is discussed.

Finally in Chapter 6 the results are summarized and conclusions drawn. The recommendations for future work for a better understanding of the stress distribution in cutting tools are given.

Chapter 2

Literature Review

2.1 Introduction

Stress analysis of a metal cutting tool deals with the determination of the stress distribution in the cutting tool produced by cutting forces. This stress distribution provides the critical regions of the cutting tool where breakage is likely to occur, and it also helps in selecting the maximum cutting force that the cutter can withstand without breakage. Experience in metal cutting indicates that tools usually break near the cutting edge where the loads are applied, and therefore to predict these tool failures stresses near the applied loads have to be determined. The method of strength of materials which is only applicable further away from applied loads and fixed boundaries can not be used and therefore in this case the more general theory of elasticity method is used.

Stress-strain relations and the basic equations of theory of elasticity is described by Timoshenko [5]. In elasticity the solution of a two dimensional problem is the stress function which satisfy the biharmonic and the boundary conditions of the problem. Once the stress function for the given problem is known then the stress components

can be determined by differentiation of the stress function and satisfying the boundary conditions of the problem.

In cutting tool stress analysis, the boundary conditions are determined experimentally using one of the following methods:

- Split-tool
- Photoelasticity
- Slip-line field.

The principle behind these methods and some boundary load distribution results by previous workers are reviewed in Section 2.3.

Once the boundary load distributions are known, the stresses within the tool may be determined using one of the following:

1. Analytical methods with:
    - concentrated load approximation.
    - distributed boundary loads.
2. Numerical methods:
    - Mellin transform
    - Finite Element Method (FEM).

The analytical methods are reviewed in Section 2.4. The Mellin Transform method is described by Tranter [9], and cutting tool stress solutions using this method are given by Thomason [10]. The finite element method is described by Cook et al [8].

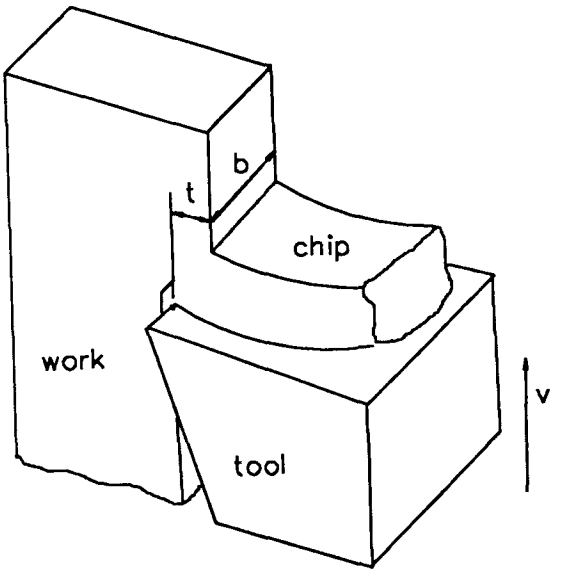

Figure 2.1: Schematics of an orthogonal cutting process

The determination of boundary conditions on cutting tools require the understanding of the principles and terminologies used in metal cutting. Therefore, this chapter is started by reviewing relevant metal cutting principles.

2.2 Metal cutting

Metal cutting principles are discussed by Shaw [12], Trent [13], Boothroyd [14] and others. Here metal cutting principles and terminologies required in this study will be briefly summarized.

All metal-cutting operations are likened to the fundamental process illustrated in Fig. 2.1 in which a wedge-shaped tool with a straight cutting edge is constrained to move relative to the workpiece in such a way that a layer of metal is removed in the form of a chip. The thickness of material removed from the workpiece is known

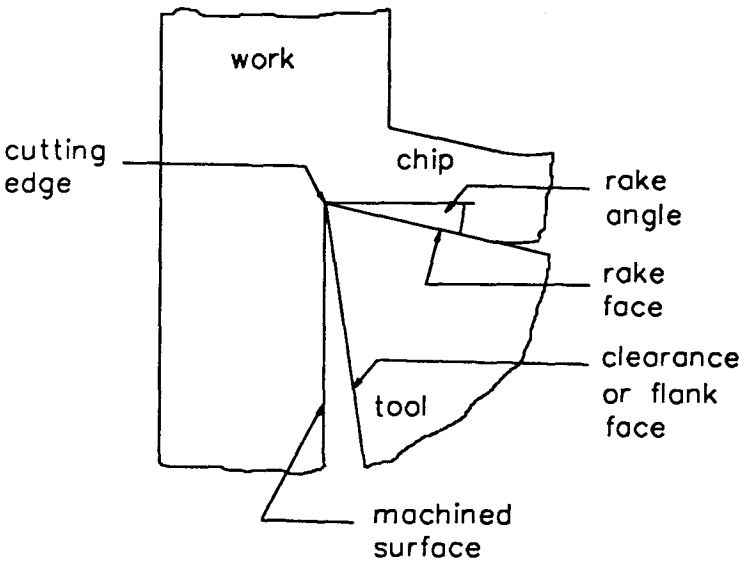

Figure 2.2: Definition of terms used in cutting

as the depth of cut t. The width of the material removed is the width of cut b. If the cutting edge is at right angles to the direction of the relative work-tool motion, Fig. 2.1, the cutting mechanism is said to be orthogonal, otherwise the term oblique cutting is used. Two-dimensional orthogonal cutting is widely used in research works because the principles developed is also generally applicable to the three-dimensional oblique cutting. The surface along which the chip flows (Fig. 2.2) is known as the rake face of the tool, and it intersects the tool flank face to form the cutting edge. The angle the rake face makes with the vertical to the machined surface is called the rake angle γ. The clearance angle is the angle between the machined surface and the flank face. This angle is necessary to prevent rubbing between the tool and the machined surface.

The mechanism of chip formation could be explained using a photomicrograph

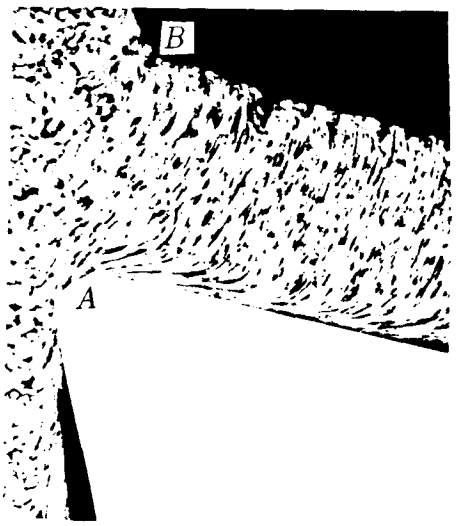

Figure 2.3: Photomicrograph of a partially formed chip, Trent [13]

of a partially formed chip shown in Fig. 2.3, Trent [13]. Such a photomicrograph is obtained by suddenly stopping the cutting operation and taking a photograph through a microscope of a polished and etched section of a partially formed chip. The device used to suddenly stop the cutting operation is called a 'quick stop' mechanism. Examination of Fig. 2.3 shows there is a plane AB in which some change in the metal structure is taking place. This plane is called the shear plane. If the work material is ductile so that it does not fracture first, then there will be plastic flow along that plane and the chip will be created and will glide along the rake face of the tool. The second point to be observed from Fig. 2.3 is that close to the cutting edge, where the normal loads are very high, the chip is in intimate contact or is under seizure with the rake face of the tool. Under this condition relative movement cannot occur at the interface between tool and chip and instead the movement involves shearing within

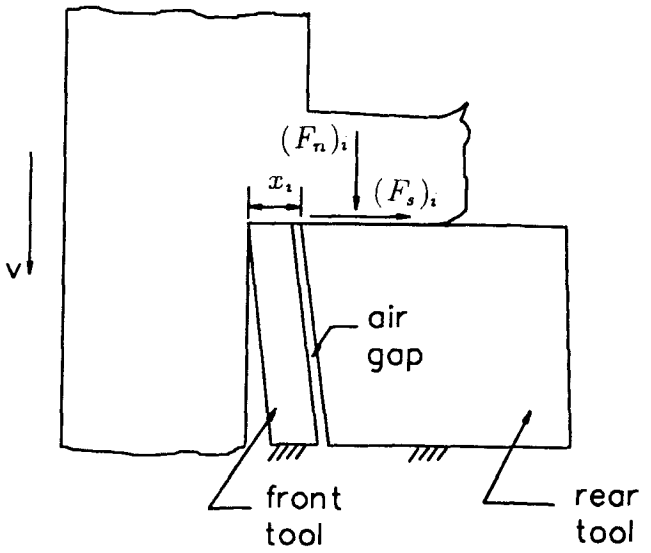

Figure 2.4: Principles of split-tool dynamometer

the chip close to the interface. Thus, the shear stress applied on the cutting tool at the cutting edge is close to the yield shear strength of the workpiece material.

2.3 Boundary load distributions

2.3.1 Split-tool method

Stress analysis of a cutting tool requires prior knowledge of the applied normal and shear cutting force distributions or boundary stresses along chip-tool contact. Boundary stresses in cutting tools have been determined using split-tool dynamometers by Kato et al [15], Barrow et al [16] and Childs et al [17].

The working principle of the split-tool dynamometer can be described using the schematic diagram of the dynamometer shown in Fig. 2.4. The dynamometer consists of two parts separated by an air gap (about 0.1 mm) and supported independently.

The air gap on the rake face is parallel to the cutting edge. The two tool parts are identified as the front-tool and the rear-tool which indicate their relative position in the composite tool. Usually, only forces transmitted through the rear-tool are measured.

For a given machining condition, the distance of the rear-tool from the cutting edge x_i, the shear and normal forces transmitted through the rear-tool $(F_s)_i$ and $(F_n)_i$ respectively, are measured (Fig. 2.4). Then the front-tool of the composite tool is replaced by a front-tool having a different land width resulting in a new value x_{i+1} for the distance of the rear-tool from the cutting edge. For the same machining conditions, the change in x_i results in a change in the chip and rear-tool contact length, and therefore change in the forces on the rear-tool. For the new value of x_{i+1}, the shear and normal forces $(F_s)_{i+1}$ and $(F_n)_{i+1}$ transmitted through the rear-tool are measured.

From the above measurements, the boundary stresses at a distance of $(x_i + x_{i+1})/2$ from the cutting edge can be calculated using

$$\sigma_i = \frac{(F_n)_{i+1} - (F_n)_i}{b(x_{i+1} - x_i)} \tag{2.1}$$

$$\tau_i = \frac{(F_s)_{i+1} - (F_s)_i}{b(x_{i+1} - x_i)} \tag{2.2}$$

where,

b = width of cut

x_i = distance of the rear-tool from the cutting edge for the i^{th} front-tool

σ_i = normal stress at a distance of $(x_i + x_{i+1})/2$ from the cutting edge

τ_i = shear stress at a distance of $(x_i + x_{i+1})/2$ from the cutting edge

$(F_n)_i$ = normal force on the rear-tool for the i^{th} front-tool

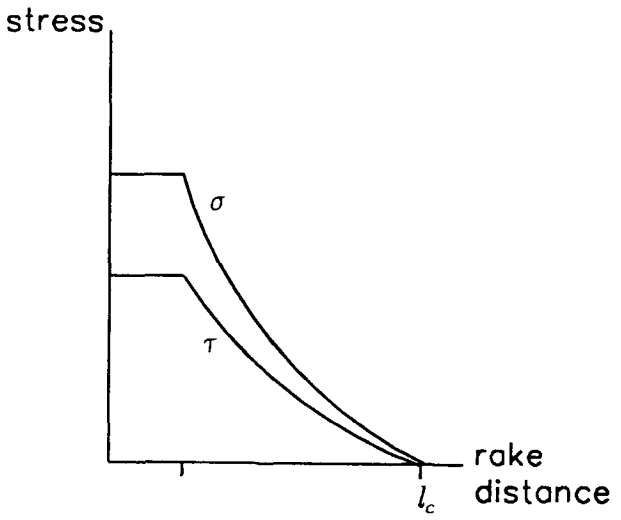

Figure 2.5: Cutting boundary load distribution result from split-tool dynamometer, Kato [15], Barrow [16], and Childs [17]

$(F_s)_i$ = shear force on the rear-tool for the i^{th} front-tool

Barrow [16] has shown that a better way to obtain a smoothed boundary stresses is to first plot the normal and shear force versus rake distance curves and to use the instantaneous slope of the curves to determine the stresses instead of the average slopes indicated by Eqs. (2.1) and (2.2).

Previous boundary stress distribution results using split-tool dynamometer

As mentioned above, various workers have used the split-tool technique to determine the boundary load distribution on a cutting tool.

Kato et al [15] determined the boundary load distribution using high-speed steel split-tool dynamometer while machining aluminium, copper, zinc and lead workpieces. The general boundary load distribution obtained is shown in Fig. 2.5. They found

that the region of constant shear stress (also called sticking region) is equal to the chip thickness and the contact length l_c is about twice the chip thickness. They also found that the ratio of the contact length to the depth of cut depend on the workpiece material, being maximum for aluminium and minimum for zinc.

Barrow et al [16] used a carbide split-tool dynamometer to determine the boundary load distribution while machining a nickel-chromium-steel workpiece. The results obtained are also as shown in Fig. 2.5. They found that the sticking region and contact length increase with increasing depth of cut, but decrease with increasing velocity.

Childs et al [17] modified the conventional split-tool by changing the inclination of the air gap with the cutting edge from 0^0 to 45^0. They used brass, aluminium, and mild steel workpieces. Their results are again similar to those shown in Fig. 2.5. However, in this case the ratio of sticking region to contact length for steel is much higher (about 0.7). In their conclusions, Childs et al. have indicated that more work is required to assess the reliability of their method.

Due to design limitations in these experiments (i.e. minimum front-tool strength and air-gap requirement) it was not possible to determine the boundary stresses near the cutting edge (within 0.2 mm). It was also observed (Barrow [16]) that at a low depth of cut, the air-gap interferes in the chip formation processes and therefore alters the forces. This implies that the boundary load distribution near the cutting edge from this method may not be reliable.

2.3.2 Photoelasticity

Another technique used to determine the boundary load distribution in a cutting tool is the photoelastic method. The photoelastic method of stress analysis is described

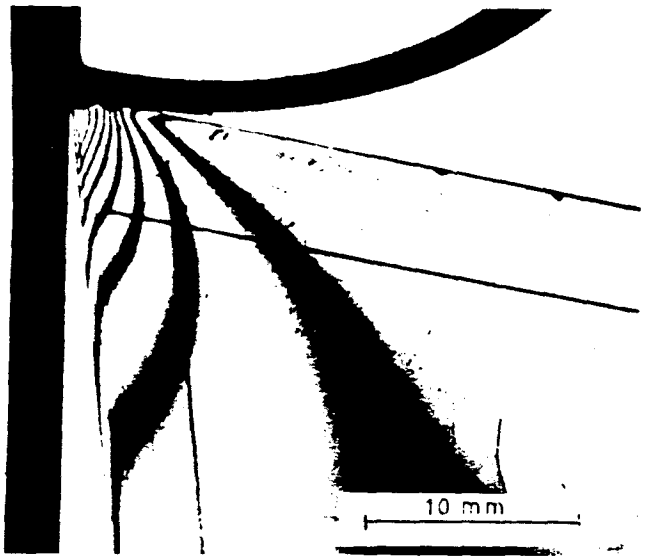

Figure 2.6: Orthogonal cutting of a lead workpiece with a photoelastic tool, Amini [20]

in detail by Frocht [1]. Here a brief review of this technique applied to cutting will be made.

Certain materials, notably plastics such as epoxy resin, celluloid and bakelite transmit polarized light along the principal stress axes at different velocities when stressed. This difference in velocity of the transmitted light produce interference fringe patterns called *isochromatics* which are used in the measurement of stresses in the photoelastic method. The apparatus used to determine stresses in the photoelastic method is called a polariscope.

In the photoelastic method of cutting tool stress analysis, a photoelastic tool is used to machine a low strength workpiece at low cutting speeds (Fig. 2.6). Lead is typically selected as the workpiece because it is soft enough to be cut without breaking the photoelastic cutting tool. The cutting tests are conducted at low speeds

to avoid the rapid drop in strength with increase in temperature of the plastic tool. A milling machine is generally used in these orthogonal machining tests.

The cutting loads on the photoelastic tool produce fringe patterns, like those shown in Fig. 2.6, which are related to the principal stress difference by

$$\sigma_1 - \sigma_3 = f_\sigma N/h \tag{2.3}$$

where,

N = fringe order

h = tool thickness

σ_1 = the algebraically larger principal stress

σ_3 = the algebraically smaller principal stress

f_σ = fringe constant

In addition to the fringe patterns, the polariscope also gives the angle ϕ between σ_1 and the $x-$axis. The locus of points having the same angle of inclination ϕ is called an *isoclinic*. Once the isochromatic N and isoclinic ϕ are determined, the shear stresses everywhere in the body are calculated using Eq. (2.3) and the shear stress equation

$$\tau_{yx} = \frac{\sigma_1 - \sigma_3}{2} \sin 2\phi \tag{2.4}$$

Then one of the normal stresses is determined by numerical integration of the equation of equilibrium

$$\frac{\partial \sigma_y}{\partial y} + \frac{\partial \tau_{xy}}{\partial x} + Y = 0 \tag{2.5}$$

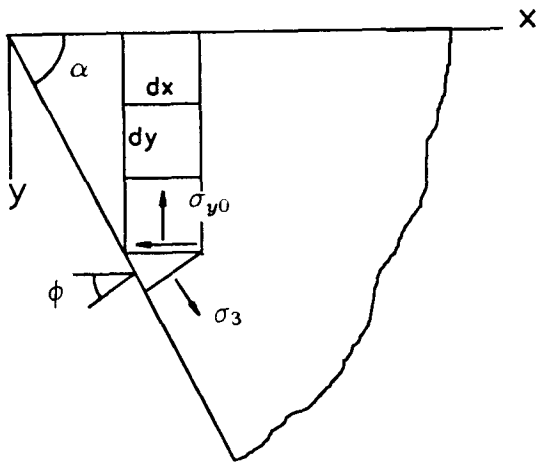

Figure 2.7: Numerical integration of the equation of equilibrium to determine normal stresses

for zero body forces ($Y = 0$), as (see Fig. 2.7)

$$\begin{aligned} \sigma_y &= \sigma_{y0} - \int_{y0}^{y} \frac{\partial \tau_{xy}}{\partial x} dy \\ &= \sigma_{y0} - \sum_{i=1}^{n} \frac{\delta \tau_{xy}}{\delta x} \delta y \end{aligned} \tag{2.6}$$

In the above equation σ_{y0} is determined from the principal stresses at the clearance face (Fig. 2.7) using the normal stress equation

$$\sigma_y = \sigma_1 \sin^2 \phi + \sigma_3 \cos^2 \phi \tag{2.7}$$

and Eq. (2.3). The clearance face is a free boundary; as a result $\sigma_1 = 0$. Therefore along the clearance face where $\alpha + \phi = \pi/2$, $\sigma_{y0} = -f_\sigma N \sin^2 \alpha \ / h$ and is directly determined from the fringe patterns and tool geometry.

Once the stress in the y-direction everywhere in the tool is determined using Eq. (2.6), then the normal stress in the x-direction is determined using the normal stress relation given by

$$\sigma_x = \sigma_y \pm \sqrt{(\sigma_1 - \sigma_3)^2 - 4\tau_{xy}^2} \tag{2.8}$$

Thus, the photoelastic method can be used to determine the stress distribution throughout the photoelastic tool including the boundary load distribution at tool-chip interface.

Many workers have used the photoelastic method to determine the stress distribution in a cutting tool. The boundary load distribution results obtained by this method can be roughly divided into two categories. The first category is the distribution for low cutting speeds of about 1 in/min as obtained by Usui [18], Chandrasekaran [19] and Betaneli [7] and is shown in Fig. 2.8. The second category is for the distribution at relatively higher cutting speeds of about 100 in/min as obtained by Amini [20] and Ahmad [21] and is shown in Fig. 2.9. The fringe patterns which are proportional to the maximum shear stress contour lines, from the photoelastic cutting tests of Amini [20], are shown in Fig. 2.6.

Boundary load distributions at lower cutting speeds.

Photoelastic boundary load distribution results at lower cutting speeds will be discussed here. Usui [18] obtained a value of 0.7 for the ratio of the sticking region to the contact length for a tool having a seven degree rake angle. Chandrasekaran [19] showed that the load distribution depends on the rake angle used: the sticking region and the contact length for a positive rake tool increase with decrease in rake angle. However, the ratio between sticking region to contact length was found to be almost

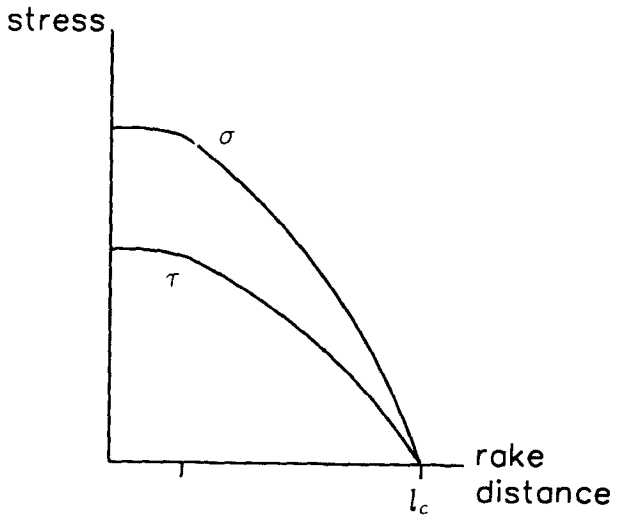

Figure 2.8: Cutting boundary load distribution result from photoelasticity at low cutting speeds, Betaneli [7], Usui [18], and Chandrasekaren [19]

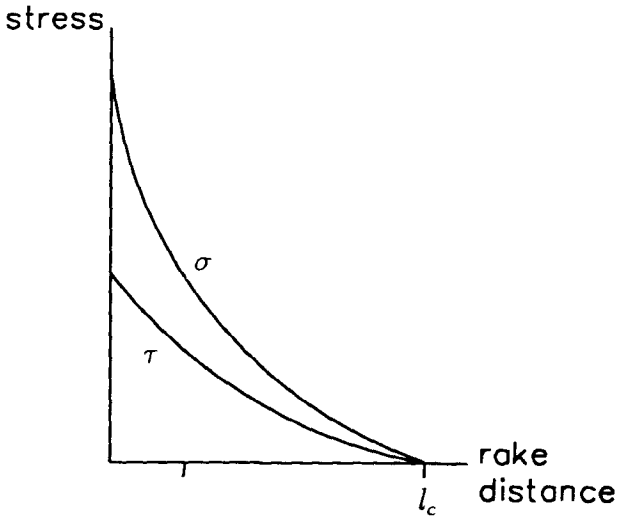

Figure 2.9: Cutting boundary load distribution result from photoelasticity at higher cutting speeds, Amini [20] and Ahmad [21]

independent of the rake angle and has a value close to 0.4. Betaneli [7], for a tool having a 20^0 rake angle, obtained a value of 0.4 for the ratio of the sticking region to the contact length.

Betaneli [7] has fitted a power law function for his lower cutting speed boundary load distribution. This function is

$$\sigma' = \sigma_o'(1 - (r'/l_c')^n) \tag{2.9}$$

where,

σ_o' = maximum normal stress at the cutting edge of the photoelastic tool

l_c' = contact length in photoelastic cutting

r' = rake distance from cutting edge of the photoelastic tool

n = exponent of the parabola

By cutting lead with a photoelastic tool at 25.4 mm/min, depth of cut of .75 mm, rake angle of 20^0 and wedge angle of 62^0, Betaneli [7] found that the exponent of the power law function $n = 3.3$.

The photoelastic normal distribution given by Eq. (2.9) can be used to determine the boundary load distribution on metal cutting tools. If the shapes of the boundary load distribution obtained from photoelasticity are assumed to be similar to those in metal cutting, then the linear relationship between the two distributions can be written as

$$\sigma' = \frac{\sigma_o'}{\sigma_o}\sigma \tag{2.10}$$

$$r' = \frac{l_c'}{l_c}r \tag{2.11}$$

where,

σ, σ' = normal stresses distribution in metal cutting and photoelastic cutting

r, r' = rake distance in metal cutting and photoelastic cutting respectively

$\sigma_o, \sigma_o^{'}$ = cutting edge applied normal stresses in metal cutting and photoelastic cutting

Substituting Eqs. (2.10) and (2.11) into Eq. (2.9), the boundary normal load distribution on the metal cutting tool is obtained as

$$\sigma = \sigma_o(1 - (r/l_c)^n) \tag{2.12}$$

where,

σ_o = maximum normal stress at the cutting edge of a metal cutting tool

l_c = contact length in metal cutting

r = rake distance from cutting edge of a metal cutting tool

n = exponent of the parabola

To determine the boundary load distribution from Eq. (2.12) for a metal cutting tool, the contact length l_c and the maximum normal stress σ_0 should be determined from metal cutting tests and the exponent n is obtained from photoelastic cutting tests.

The maximum normal stress in Eq. (2.12) could be determined from the average normal stress on the cutting tool. This average stress is given by

$$\sigma_{av} = \frac{F_n}{bl_c} \tag{2.13}$$

where,

σ_{av} = average normal stress

F_n = cutting force normal to rake face

b = width of cut

l_c = contact length

The average normal stress is also related to the normal boundary load distribution by

$$\sigma_{av} = \frac{1}{l_c}\int_0^{l_c} \sigma dr \tag{2.14}$$

Substituting the parabolic distribution given by Eq. (2.12) into Eq. (2.14) and simplifying, the expression obtained for the maximum normal boundary stress is

$$\sigma_0 = \frac{n+1}{n}\sigma_{av} \tag{2.15}$$

The normal boundary load distribution of Eq. (2.12) is thus completely determined from the photoelastic results which gives the exponent n, and from actual metal cutting tests which provide the contact length, normal cutting force, width of cut and the average normal stress. The boundary shear stress is determined by assuming the shear stress to be related to the normal stress through the coefficient of friction. Therefore, the boundary shear stress is given by

$$\tau = \mu\sigma \tag{2.16}$$

In the above equation the friction coefficient is calculated using the relation

$$\mu = \frac{F_s}{F_n} \tag{2.17}$$

where,

F_n = boundary force normal to rake face

F_s = boundary force parallel to rake face

Boundary load distribution for higher cutting speeds

Photoelastic boundary load distribution result at higher cutting speeds will be discussed here. Ahmad [21] has fitted a polynomial function for his higher speed boundary load distributions and they are given by

$$\sigma' = 2.91 - 1.53r' + .214r'^2 - .0033r'^3 \tag{2.18}$$

$$\tau' = 1.63 - 1.24r' + .315r'^2 - .0266r'^3 \tag{2.19}$$

where,

σ' = normal boundary stress on the photoelastic tool, kg/mm^2

τ' = shear boundary stress on the photoelastic tool, kg/mm^2

r' = rake face distance from the cutting edge of the photoelastic tool, mm.

These equations were obtained for a photoelastic tool model having a rake angle of 6^0, depth of cut of .203 mm, width of cut of 5.1 mm, cutting speed of 2.93 m/min and contact length of 4.5 mm. As described in the previous section, the above equations can also be used to determine the stress distribution in metal cutting tools by assuming the shape of the boundary stress on both photoelastic tool and metal cutting tool to be similar.

In the photoelastic boundary load distribution for higher cutting speeds shown in Fig. 2.9, there is little sticking region (constant shear stress near the cutting edge) and this fact has been confirmed by Barrow [16] using split-tool dynamometer where he shows a decrease in the sticking region with increase in cutting speed. Therefore, at higher cutting speeds where the sticking region is small, the shape of the boundary load distribution from split-tool and photoelasticity are approximately similar.

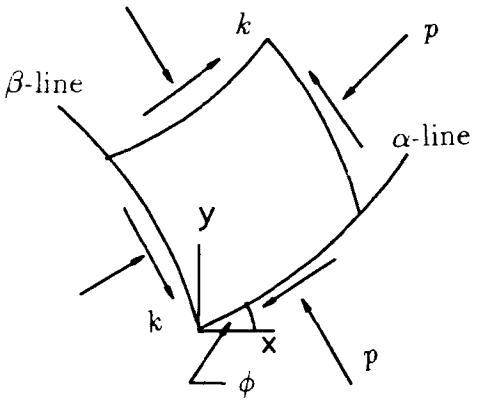

Figure 2.10: Stress components on shear planes on an infinitesimal element

2.3.3 Slip-line theory

In the previous sections the experimental methods used to estimate the boundary load distribution in metal cutting tools were discussed. In this section a purely theoretical method from plasticity theory can be used to approximate the applied normal and shear stresses at the cutting edge is discussed.

This plasticity solution, as proposed by Loladze [37], makes use of the properties of slip-lines along the shear plane to determine the normal and shear stresses at the cutting edge. The state of stress throughout a rigid, perfectly plastic solid material under deformation can be represented by a constant yield shear stress k in plane strain, and a hydrostatic stress p which in general varies from point to point throughout the material. The two maximum shear stress planes at each point of the material under deformation are perpendicular to each other and form two orthogonal families of

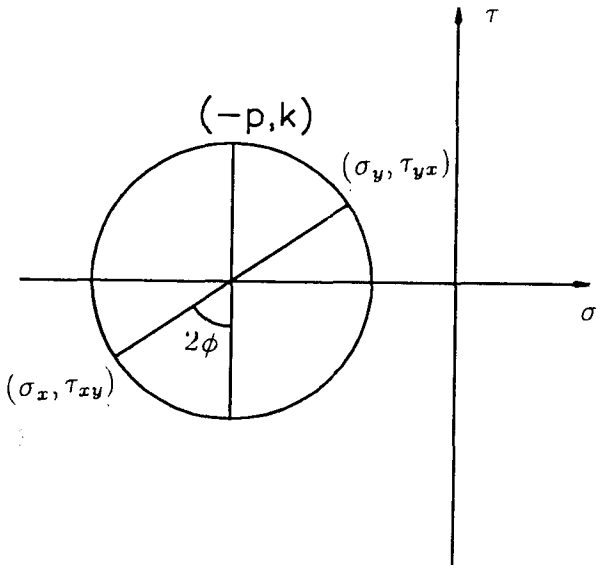

Figure 2.11: Derivation of co-ordinate stresses from the shear plane stresses

curves known as slip-lines. These slip-lines are labelled as α and β as shown in Fig. 2.10. The directions of these slip-lines are not arbitrary and are determined from the direction of the shear stresses. The shear stress directions and the corresponding direction of the slip-lines are as shown in Fig. 2.10. Another parameter which is important in slip-line theory is the angle ϕ measured in the counter-clockwise direction from the x-axis to the α slip-line, Fig. 2.10. The stresses in the x and y-directions in terms of the hydrostatic pressure and yield shear stress can be derived from the Mohr's circle shown in Fig. 2.11, and are given by

$$\sigma_x = -p - k \sin 2\phi \tag{2.20}$$

$$\sigma_y = -p + k \sin 2\phi \tag{2.21}$$

$$\tau_{xy} = k \cos 2\phi \tag{2.22}$$

In the above equations p is considered positive when in compression. Substituting the above equations into the equations of equilibrium for the case of no body forces, and taking the α-line to coincide with the x-axis at the origin (Johnson [23]) yields along an α-line

$$\delta p = -2k\delta\phi \tag{2.23}$$

and along β-line

$$\delta p = 2k\delta\phi \tag{2.24}$$

where,

δp = change in hydrostatic pressure

k = shear yield stress

$\delta\phi$ = change in the angle between x-axis and a slip-line (radian).

These equations are known as the Hencky equations and together with the component stresses given by Eqs. (2.20) to (2.22) are all that are required to determine the normal and shear boundary stresses at the cutting edge.

The use of the above equations to estimate the applied stresses at the cutting edge B of Fig. 2.12 is discussed next. Since the shear plane passing through A and B of Fig. 2.12 is a maximum shear stress line it is a slip-line. From the knowledge of the direction of the shear stress along the shear plane, the orientation of the slip lines are as shown in Fig. 2.12 and the shear plane is a β-line. At point A the plane perpendicular to the x-direction is a free boundary ($\sigma_x = 0$ and $\tau_{xy} = 0$), therefore it is a principal plane. The angle between the normal to the principal plane and the maximum shear plane is $\pi/4$, and therefore at point A the angle between the x-axis and the α-line is $\phi_A = \pi/4 + \pi/2 = 3\pi/4$. Applying Eq. (2.20) to point A, the

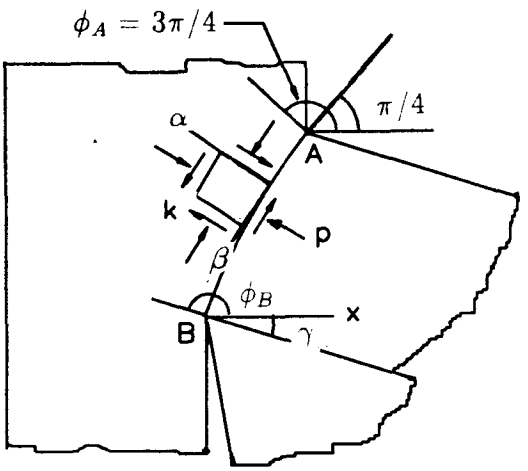

Figure 2.12: Boundary stresses at the cutting edge using slip line theory

hydrostatic compressive stress is found to be $p_A = k$. It is known that along the rake face, at the cutting edge, the work material is in shear yielding and therefore this face is an α-slip line. From Fig. 2.12 it can be seen that at point B, $\phi_B = \pi - \gamma$ and therefore the change in angle ϕ from A to B is $\delta\phi = \pi/4 - \gamma$. For a β slip-line, from Eq. (2.24) the hydrostatic stress at the cutting edge therefore is $p_B = 2k(1/2 + \pi/4 - \gamma)$. Finally, from Fig. 2.12 at point B it can be seen that the applied normal stress is equal to the hydrostatic pressure and the applied shear stress is equal to the yield shear strength of the workpiece, and these yield

$$\sigma_o = 2k(1/2 + \pi/4 - \gamma) \tag{2.25}$$

$$\tau_o = k \tag{2.26}$$

where,

σ_o = normal boundary stress at the cutting edge

τ_o = shear boundary stress at the cutting edge

k = yield shear strength of the work material

γ = rake angle

The above equations provide the applied normal and shear stresses at the cutting edge and they can be used to estimate the cutting edge stresses. They do not take into account the strain-hardening and strain-rate effects of real materials, and therefore their correlation with experimental values are approximate. However, as shown by Chandrasekaren [19] for non-strain hardening material at lower strain-rates good correlation is obtained.

2.4 Analytical stress analysis of cutting tools

2.4.1 Analytical stress analysis of cutting tools for a concentrated load approximation.

When the stresses far from the cutting edge within the wedge shape are required, the solution with single load approximation by Frocht [1] may be used. This solution is derived from the stress function

$$\psi = Cr\theta \sin\theta \tag{2.27}$$

where,

C = a constant,

r and θ are as defined in Fig. 2.13.

The stress components are derived from the stress function using the relations

$$\sigma_\theta = \frac{\partial^2 \psi}{\partial r^2} \tag{2.28}$$

$$\sigma_r = \frac{1}{r}\frac{\partial \psi}{\partial r} + \frac{1}{r^2}\frac{\partial^2 \psi}{\partial \theta^2} \tag{2.29}$$

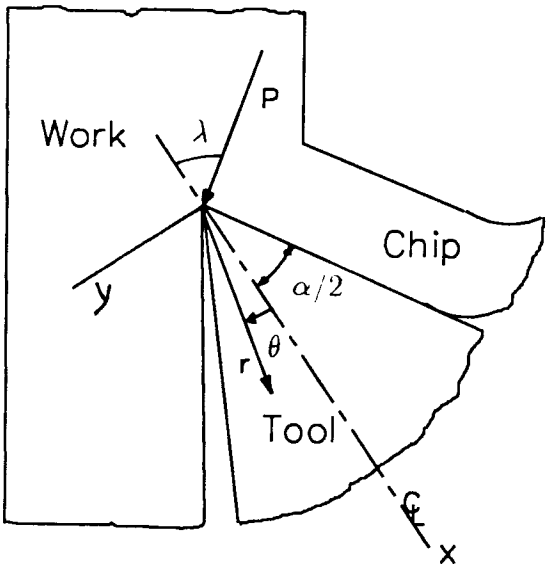

Figure 2.13: Concentrated cutting load at the cutting edge

$$\tau_{r\theta} = -\frac{\partial}{\partial r}\left(\frac{1}{r}\frac{\partial \psi}{\partial \theta}\right) \tag{2.30}$$

where ψ is the stress function.

By substituting Eq. (2.27) into Eqs. (2.28) to (2.30), and applying force equilibrium for the cutting tool in Fig. 2.13, the stress distributions within the tool are obtained as

$$\sigma_r = -\frac{2P}{rb}\left(\frac{\cos\lambda\cos\theta}{\alpha+\sin\alpha} + \frac{\sin\lambda\sin\theta}{\alpha-\sin\alpha}\right) \tag{2.31}$$

$$\sigma_\theta = 0. \tag{2.32}$$

$$\tau_{r\theta} = 0. \tag{2.33}$$

where,

P = concentrated load on the tool, $P = \sqrt{F_n^2 + F_s^2}$

F_s = shear force on rake face

F_n = normal force on rake face

b = width of cut

α = wedge angle

r = radial distance from cutting edge

μ = average friction coefficient, $\mu = F_s/F_n$

λ = angle between tool axis of symmetry and force P, $\lambda = tan^{-1}(1/\mu) - \alpha/2$

θ = angle measured from tool axis of symmetry, positive when as shown in Fig. 2.13

The component stresses are shown in Fig. 2.15.

The above equations were used by Kaldor [2] to determine the optimal tool geometry and by Chandrasekaran [3] to calculate fracture stresses in milling cutters. Examination of Eq. (2.31) shows that at the cutting edge where $r = 0$, the radial stresses is undefined and therefore this solution can not be used to estimate stresses close to the cutting edge. However, far from the cutting edge within the wedge shape this solution may be applicable. This will be investigated in the current study. An important conclusion that can be made from Eq. (2.31) is that for a given cutting tool and cutting conditions, further from the cutting edge (i.e. as r increases) the radial stress decreases. This decrease in stress further from the cutting edge is due to the increase in resisting area or section modulus of the wedge.

2.4.2 Analytical stress analysis of cutting tools for distributed boundary loads.

When the stresses near the cutting edge where the cutting loads are applied are required, the actual load distribution along tool-chip contact should be used. Elasticity solution applicable for a distributed load on an infinite wedge may be used to determine the stress distribution in the loaded region of the cutting tool. The infinite

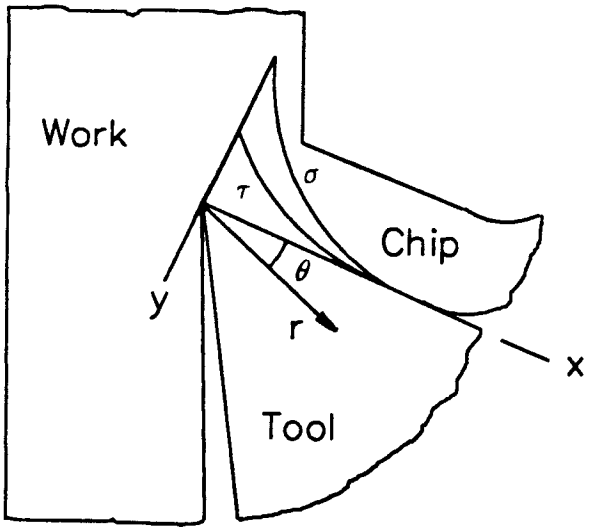

Figure 2.14: Distributed load on the rake face

wedge solution for distributed loads is discussed in this section.

The generalized stress function for two dimensional problems in polar coordinates was derived by Michell [4]. This stress function was then used by Timoshenko [5] to determine the stress distribution in an infinite wedge for polynomial boundary load distributions. The infinite wedge solution was letter used by Archibald [6] and Betaneli [7] and others to determine the stress distribution in metal cutting tools.

The generalized stress function derived by Michell [4] is given as

$$\psi = a_0 \log r + b_0 r^2 + c_0 r^2 \log r + d_0 r^2 \theta + a_0' \theta$$

$$+ \frac{a_1}{2} r\theta \sin\theta + (b_1 r^3 + a_1' r^{-1} + b_1' r \log r) \cos\theta$$

$$- \frac{c_1}{2} r\theta \cos\theta + (d_1 r^3 + c_1' r^{-1} + d_1' r \log r) \sin\theta$$

$$+\sum_{n=2}^{\infty}(a_n r^n + b_n r^{n+2} + a_n^{'} r^{-n} + b_n^{'} r^{-n+2})\cos n\theta$$

$$+\sum_{n=2}^{\infty}(c_n r^n + d_n r^{n+2} + c_n^{'} r^{-n} + d_n^{'} r^{-n+2})\sin n\theta \qquad (2.34)$$

where,

r and θ are as defined in Fig. 2.14 and $a_0, b_0, c_0, d_0, \ldots$ are constants.

The stress components are determined by substituting Eq. (2.34) into the component stress equations (2.28) to (2.30) and taking only terms containing r^n with $n \geq 0$. The results of this substitution as given by Timoshenko [5] and Archibald [6] for the tangential (σ_θ), radial (σ_r) and shear ($\tau_{r\theta}$) stress components as shown in Fig. 2.15 are:

$$\sigma_\theta = 2b_0 + 2d_0\theta + 2a_2\cos 2\theta + 2c_2\sin 2\theta$$

$$+\sum_{n=1}^{\infty}(n+1)(n+2)r^n[b_n\cos n\theta + d_n\sin n\theta$$

$$+ a_{n+2}\cos(n+2)\theta + c_{n+2}\sin(n+2)\theta], \qquad (2.35)$$

$$\sigma_r = 2b_0 + 2d_0\theta - 2a_2 cos2\theta - 2c_2\sin 2\theta$$

$$-\sum_{n=1}^{\infty}(n+1)r^n[(n-2)(b_n\cos n\theta + d_n\sin n\theta)$$

$$+ (n+2)\{a_{n+2}\cos(n+2)\theta + c_{n+2}\sin(n+2)\theta\}], \qquad (2.36)$$

$$\tau_{r\theta} = -d_0 + 2a_2\sin 2\theta - 2c_2\cos 2\theta$$

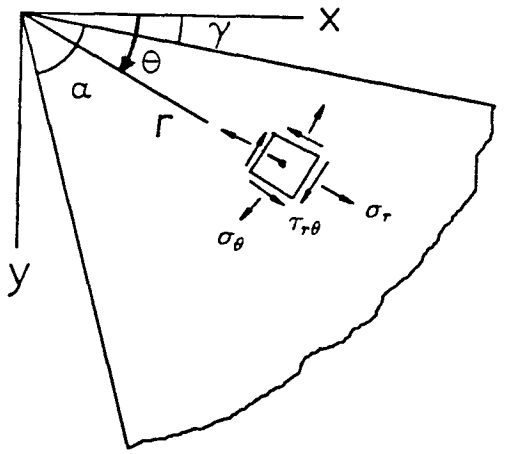

Figure 2.15: Stress components in polar co-ordinate on an infinitesimal element of a cutting tool

$$+\sum_{n=1}^{\infty} r^n(n+1)[n(b_n \sin n\theta - d_n \cos n\theta)$$

$$+ (n+2)\{a_{n+2} \sin (n+2)\theta - c_{n+2} \cos (n+2)\theta\}] \tag{2.37}$$

How the above equations may be used to determine the stress distribution within the loaded region of the tool will be discussed in the following section and in Chapter 3.

2.5 Previous analytical cutting tool stress solutions

2.5.1 Cutting edge stresses

Archibald [6] used the stress component equations (2.35) to (2.37) to determine the stresses at the cutting edge ($r = 0$ and $\theta = 0$). He assumed a linear boundary

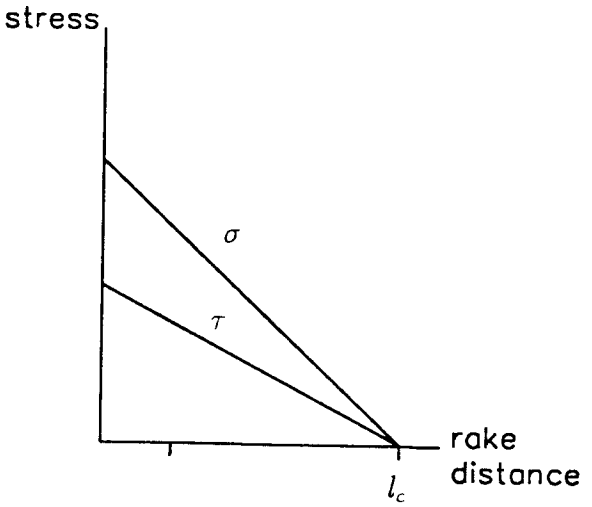

Figure 2.16: Linear cutting load distribution assumption, Archibald [6]

load distribution to determine the boundary stresses from cutting forces. This linear normal load distribution is given by

$$\sigma = \sigma_0(1 - r/l_c) \tag{2.38}$$

where,

σ = normal boundary load distribution

r = rake distance from cutting edge

l_c = contact length.

The normal stress at the cutting edge determined by Archibald [6] from his linear load distribution assumption and power measurements is given by

$$\sigma_o = 3.36(88.24 - \gamma)\frac{\cos\beta}{\cos(\beta - \gamma)} \tag{2.39}$$

where,

γ = rake angle (deg)

β = friction angle (deg)

σ_o = maximum boundary normal stress at the cutting edge (kpsi)

In his analysis, Archibald used a chip-tool contact length of twice the depth of cut ($l_c = 2t$). He indicated this length to be determined experimentally. The boundary shear stress is determined from the coefficient of friction and the normal boundary load distribution as $\tau = \mu\sigma$. The clearance angle used was 5^0 and the wedge angle α is related to the rake angle γ by $\alpha = 85 - \gamma$.

For the linear boundary load distribution, from the stress component equations (2.35) and (2.37), $n = 0$ and 1 and the eight constants $b_0, d_0, a_2, c_2, b_1, d_1, a_3$, and c_3 can be determined by substituting the linear boundary load distributions on the rake face, and the zero load distributions on the flank face, into Eqs. (2.35) and (2.37) and solving the equations obtained simultaneously for the constants. Then the stress components at the cutting edge are determined by substituting the determined constants back into equations (2.35) to (2.37). The solution obtained for the rake face radial stress at the cutting edge by Archibald [6] using this procedure is given by

$$\sigma_r = \frac{\alpha}{\tan\alpha - \alpha}|\sigma_0| - \frac{\tan\alpha(\alpha\tan\alpha + 1) - \alpha}{(\tan\alpha - \alpha)\tan\alpha}|\tau_0| \tag{2.40}$$

where,

σ_r = radial stress parallel to the rake face at the cutting edge

α = wedge angle, radians

$|\sigma_0|$ = magnitude of normal stress at the cutting edge on the rake face

$|\tau_0|$ = magnitude of shear stress at the cutting edge on the rake face

The radial stresses from Archibald's [6] solution for various coefficients of friction ($\mu = \tau_0/\sigma_0$) as a function of the wedge angle α, as determined from Eq. (2.40) and Eq. (2.39), are shown in Fig. 2.17. In the current study the applicability of Eq. (2.40) in cutting edge stress analysis will be verified numerically.

2.5.2 Stress distribution in the loaded region for parabolic load

As discussed in the previous section, Archibald [6] used the stress component equations for distributed loads, Eqs. (2.35) to (2.37), to determine the stresses at the cutting edge of a tool. Betaneli [7] then went further and used these equations to determine the stress distribution in the whole loaded region.

The method used by Betaneli [7] was similar to that used by Archibald [6] except he replaced the linear load assumption by an experimental one. The experimental boundary load distribution result by Betaneli [7] was described in Section 2.3.2. In Section 2.3.2 it was noted that in addition to the results from photoelasticity, force and contact length measurements are required to completely determine the boundary stresses in metal cutting tools. Betaneli [7] took data from Zorev's [24] extensive machining test results in order to determine the boundary load distribution on a metal cutting tool. Zorev's results which were used by Betaneli [7] as discussed in Section 2.3.2 are given in Table (2.1).

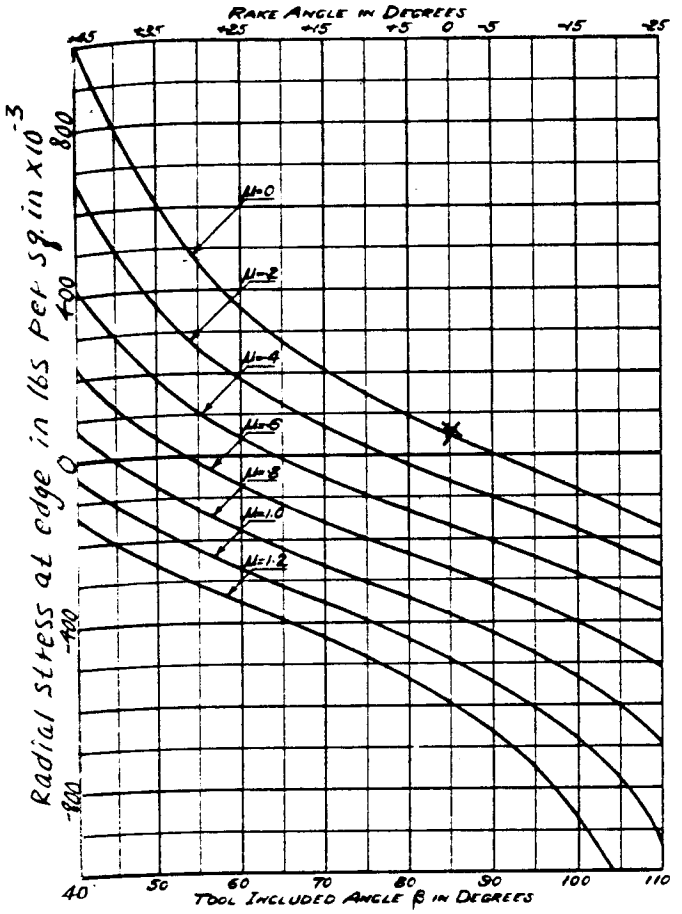

Figure 2.17: Radial cutting edge stresses as a function of wedge angle and friction coefficient, Archibald [6]. Here β is the wedge angle

Table 2.1. Machining parameters
when cutting steel in water, Zorev [24].

$\gamma = 20^0$, v =.7m/min			
t mm	l_c mm	μ	σ_{av} kg/mm^2
0.2	0.5	0.36	60.0

where,

γ = rake angle

t = depth of cut

l_c = contact length

v = velocity of tool relative to the workpiece

μ = coefficient of friction at chip-tool contact

σ_{av} = average normal stress along chip-tool contact

Using the relations given in Section 2.3.2 and the data from Table (2.1), the boundary load distributions on a metal cutting tool can be determined completely. For this load distribution, the stress distribution in the loaded region is determined from the stress component equations (2.35) to (2.37). The principal stresses from Betaneli's [7] solution are shown in Fig. (2.18).

The results discussed in the previous sections are the available analytical approaches in analytical cutting tool stress analysis. The limitation of these approaches and the objectives of the current study are discussed in the next section.

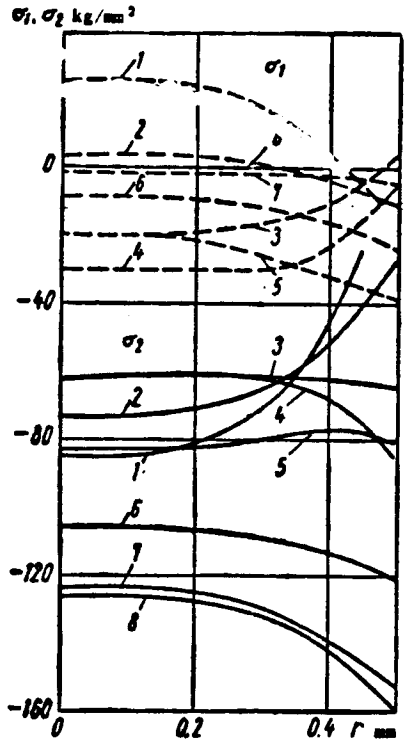

Principal stresses σ_1 and σ_2 plotted against r and θ (with γ = 20°; β = 62°; a = 0.2mm and n = 3.33):
1 - θ = γ = 20°; 2 - θ = 30°; 3 - θ = 40°; 4 - θ = 50°;
5 - θ = 60°; 6 - θ = 70°; 7 - θ = 80°; 8 - θ = β + γ = 82°.

Figure 2.18: Principal stress distributions in the loaded region for a parabolic load, Betaneli [7]. Here a is the depth of cut and β is the wedge angle

2.6 Objectives of the present work and methods of investigation

From the discussion in the previous sections, stress on cutting tools have been estimated analytically both at the cutting edge and in the whole loaded region. However, these solutions were obtained on the assumption that the infinite wedge solution can be applied to determine the stresses in the finite cutting tool. It is important to verify this assumption because the solutions obtained by using this approach may sometimes lead to incorrect conclusions. To critically investigate this assumption and come up with a conclusion as to whether this approach could be applied or not, and if it could be applied then to identify the conditions is the purpose of the first phase of this work.

In the second phase of this work, the critical regions of cutting tools where breakage is likely to occur will be predicted. For this an orthogonal cutting tool and an end mill will be considered. Analytical methods will first be used to predict the critical stresses then these solutions will be verified numerically. This comparison will indicate whether analytical solutions could be applied in the failure analysis of cutting tools.

The steps that will be taken in this study are listed below:

- Compare the analytical solution by previous researchers with a finite element solution for the same geometry and 'same' boundary load distribution.
- If there is difference between the two solutions then determine the cause for this difference.
- From the understanding of the reason for the difference between the two solutions identify the conditions (boundary load distribution) where the analytical

solution may be used and verify this using an example.

- Compare the solution reached in the last step above with previous experimental result for similar geometry and boundary load distribution.
- From the solution obtained above identify the critical regions of the two-dimensional cutting tool and its modes of failure.
- Determine the stresses at critical regions of an end mill for shank breakage using analytical methods.
- Verify the analytical solution for shank stresses obtained above numerically. This result will indicate whether analytical methods are applicable in end mill shank stress analysis.
- Compare the analytical solution obtained for the orthogonal cutting tool above with numerical solution for an end mill flute. This result will indicate whether analytical methods are applicable or not in end mill flute stress analysis.
- Finally give a conclusion of this work and suggest what future work should be done to get an improved understanding of stress distribution in cutting tools.

Chapter 3

Stress Calculation in Orthogonal Cutting Tools

3.1 Introduction

The analytical stress equations (2.35), (2.36), and (2.37) of the previous chapter were used by Archibald [6], Betaneli [7] and others to determine stresses in cutting tools. This analytical approach is based on the assumption that the infinite wedge solution could be used to determine the stress distribution in the finite cutting tool. One of the motivations of the present research is to critically investigate this assumption. We begin this investigation by first verifying previous analytical solutions and then comparing these results with numerical solutions.

The boundary load distribution used by Archibald [6] is linear and that of Betaneli [7] is parabolic. These boundary load distributions are limited since they can not include the different possible boundary load distributions on a cutting tool. In Section 3.2 an analytical solution for a polynomial load distribution which provides a more general case is developed. The previous analytical solutions are compared with current analytical solutions in Section 3.3. This is done to verify the previous analytical

solutions and also to test the computer program for our analytical solutions. In Section 3.4 these analytical solutions are compared with FEM results for 'identical' boundaries and geometry. In Section 3.5 the results of this chapter are discussed and conclusions regarding these analysis is drawn.

3.2 Analytical cutting tool stress calculation

In this section, the analytical method used to determine the stress distribution in a cutting tool for a general polynomial boundary load distribution is discussed.

The stress equations (2.35), (2.36), and (2.37), can be rewritten in the following form

$$\begin{aligned}\sigma_\theta &= 2a_0 + 2b_0\theta + 2c_0\cos 2\theta + 2d_0\sin 2\theta \\ &+ \sum_{i=1}^{\infty}(i+1)(i+2)r^i[a_i\cos i\theta + b_i\sin i\theta \\ &\quad + c_i\cos(i+2)\theta + d_i\sin(i+2)\theta],\end{aligned} \tag{3.1}$$

$$\begin{aligned}\sigma_r &= 2a_0 + 2b_0\theta - 2c_0 cos2\theta - 2d_0\sin 2\theta \\ &- \sum_{i=1}^{\infty}(i+1)r^i[(i-2)(a_i\cos i\theta + b_i\sin i\theta) \\ &+ (i+2)\{c_i\cos(i+2)\theta + d_i\sin(i+2)\theta\}],\end{aligned} \tag{3.2}$$

$$\tau_{r\theta} = -b_0 + 2c_0 \sin 2\theta - 2d_0 \cos 2\theta$$

$$+ \sum_{i=1}^{\infty} r^i (i+1)[i(a_i \sin i\theta - b_i \cos i\theta)$$

$$+ (i+2)(c_i \sin (i+2)\theta - d_i \cos (i+2)\theta)] \tag{3.3}$$

where

σ_θ = tangential stress

σ_r = radial stress

$\tau_{r\theta}$ = shear stress a_i, b_i, c_i, and d_i for $i \geq 0$ are constants

r and θ, and the positive direction of the component stresses are as shown in Fig. 2.15.

The above equations can be written in a simplified form in terms of normal (N_i), radial (R_i) and shear (S_i) polynomial coefficients as given below:

$$\sigma_\theta = \sum_{i=0}^{\infty} N_i r^i \tag{3.4}$$

$$\sigma_r = \sum_{i=0}^{\infty} R_i r^i \tag{3.5}$$

$$\tau_{r\theta} = \sum_{i=0}^{\infty} S_i r^i \tag{3.6}$$

where the coefficients of the polynomial in the above three equations, determined from equations (3.1) to (3.3), are given by

for $i = 0$,

$$N_0 = \lfloor 2 \;\; 2\theta \;\; 2\cos 2\theta \;\; 2\sin 2\theta \rfloor \begin{Bmatrix} a_0 \\ b_0 \\ c_0 \\ d_0 \end{Bmatrix} \tag{3.7}$$

$$R_0 = \lfloor 2 \;\; 2\theta \;\; -2\cos 2\theta \;\; -2\sin 2\theta \rfloor \begin{Bmatrix} a_0 \\ b_0 \\ c_0 \\ d_0 \end{Bmatrix} \tag{3.8}$$

$$S_0 = \lfloor 0 \;\; -1 \;\; 2\sin 2\theta \;\; -2\cos 2\theta \rfloor \begin{Bmatrix} a_0 \\ b_0 \\ c_0 \\ d_0 \end{Bmatrix} \tag{3.9}$$

and for i ≥ 1,

$$N_i = j \left\lfloor \frac{\cos i\theta}{i} \;\; \frac{\sin i\theta}{i} \;\; \frac{\cos(i+2)\theta}{i} \;\; \frac{\sin(i+2)\theta}{i} \right\rfloor \begin{Bmatrix} a_i \\ b_i \\ c_i \\ d_i \end{Bmatrix} \tag{3.10}$$

$$R_i = m \left\lfloor \frac{\cos i\theta}{i+2} \;\; \frac{\sin i\theta}{i+2} \;\; \frac{\cos(i+2)\theta}{i-2} \;\; \frac{\sin(i+2)\theta}{i-2} \right\rfloor \begin{Bmatrix} a_i \\ b_i \\ c_i \\ d_i \end{Bmatrix} \tag{3.11}$$

$$S_i = j \left[\frac{\sin i\theta}{i+2} \quad -\frac{\cos i\theta}{i+2} \quad \frac{\sin(i+2)\theta}{i} \quad -\frac{\cos(i+2)\theta}{i} \right] \begin{Bmatrix} a_i \\ b_i \\ c_i \\ d_i \end{Bmatrix} \tag{3.12}$$

where,

$j = i(i+1)(i+2)$

$m = (i-2)(i+1)(i+2)$

N_i = Normal polynomial distribution coefficients

R_i = Radial polynomial distribution coefficients

S_i = Shear polynomial distribution coefficients

a_i, b_i, c_i, and d_i are constants to be determined from the boundary load distributions.

The stress components in Eqs. (3.1) to (3.3) at any point (r, θ) can be determined if the constants a_i, b_i, c_i, and d_i for $i \geq 0$ are known. These constants are determined from the boundary load distributions of σ_θ and $\tau_{r\theta}$ at the rake and flank faces. From Eqs. (3.4) and (3.6), the boundary loads can be written in polynomial form so that at the boundaries N_i and S_i take the values of the coefficients of the polynomial normal and shear boundary load distributions respectively. From these boundary conditions, as is shown below, the arbitrary constants and therefore the stresses within the cutting tool can be determined. The coordinate axes and tool geometry used are shown in Fig. 2.15.

If the normal (σ_θ) and shear $(\tau_{r\theta})$ boundary load distributions on the rake and flank faces are assumed to be represented by $(n+1)$ finite terms of a polynomial, then they can be written as

$$(\sigma_\theta)_{\theta=\theta_r} = \sum_{i=0}^{n} N_{ri} r^i \tag{3.13}$$

$$(\sigma_\theta)_{\theta=\theta_f} = \sum_{i=0}^{n} N_{fi} r^i \tag{3.14}$$

$$(\tau_{r\theta})_{\theta=\theta_r} = \sum_{i=0}^{n} S_{ri} r^i \tag{3.15}$$

$$(\tau_{r\theta})_{\theta=\theta_f} = \sum_{n=0}^{n} S_{fi} r^i \tag{3.16}$$

where,

$\theta_r = \gamma$

$\theta_f = \gamma + \alpha$

r = radial distance from cutting edge

n = degree of the polynomial boundary load distribution

$(\sigma_\theta)_{\theta=\theta_r}$ and N_{ri} are the rake face normal load distribution and its coefficients

$(\sigma_\theta)_{\theta=\theta_f}$ and N_{fi} are the flank face normal load distribution and its coefficients

$(\tau_{r\theta})_{\theta=\theta_r}$ and S_{ri} are the rake face shear load distribution and its coefficients

$(\tau_{r\theta})_{\theta=\theta_f}$ and S_{fi} are the flank face shear load distribution and its coefficients

Substituting the polynomial coefficients for the normal and shear load distributions at the rake and flank faces into the equations for N_i (Eqs. (3.7) and (3.10)) and S_i (Eqs. (3.9) and (3.12)), for $0 \leq i \leq n$ yields (n+1) sets of matrix equations:

for $i = 0$

$$\begin{Bmatrix} N_{r0} \\ N_{f0} \\ S_{r0} \\ S_{f0} \end{Bmatrix} = \begin{bmatrix} 2 & 2\theta_r & 2\cos 2\theta_r & 2\sin 2\theta_r \\ 2 & 2\theta_f & 2\cos 2\theta_f & 2\sin 2\theta_f \\ 0 & -1 & 2\sin 2\theta_r & -2\cos 2\theta_r \\ 0 & -1 & 2\sin 2\theta_f & -2\cos 2\theta_f \end{bmatrix} \begin{Bmatrix} a_0 \\ b_0 \\ c_0 \\ d_0 \end{Bmatrix} \tag{3.17}$$

for $1 \leq i \leq n$

$$\begin{Bmatrix} N_{ri} \\ N_{fi} \\ S_{ri} \\ S_{fi} \end{Bmatrix} = j \begin{bmatrix} \frac{\cos i\theta_r}{i} & \frac{\sin i\theta_r}{i} & \frac{\cos(i+2)\theta_r}{i} & \frac{\sin(i+2)\theta_r}{i} \\ \frac{\cos i\theta_f}{i} & \frac{\sin i\theta_f}{i} & \frac{\cos(i+2)\,\theta_f}{i} & \frac{\sin(i+2)\,\theta_f}{i} \\ \frac{\sin i\theta_r}{i+2} & -\frac{\cos i\theta_r}{i+2} & \frac{\sin(i+2)\theta_r}{i} & -\frac{\cos(i+2)\theta_r}{i} \\ \frac{\sin i\theta_f}{i+2} & -\frac{\cos i\theta_f}{i+2} & \frac{\sin(i+2)\,\theta_f}{i} & -\frac{\cos(i+2)\,\theta_f}{i} \end{bmatrix} \begin{Bmatrix} a_i \\ b_i \\ c_i \\ d_i \end{Bmatrix} \tag{3.18}$$

where,

$j = i(i+1)(i+2)$

$\theta_r = \gamma$

$\theta_f = \gamma + \alpha$

γ = rake angle

α = wedge angle

i = powers of the polynomial

N_{ri} = rake face polynomial normal load distribution coefficients

N_{fi} = flank face polynomial normal load distribution coefficients

S_{ri} = rake face polynomial shear load distribution coefficients

S_{fi} = flank face polynomial shear load distribution coefficients

a_i, b_i, c_i and d_i for $i \geq 0$ are constants.

Eqs. (3.17) and (3.18), with the knowledge of the boundary normal and shear load distribution and the geometry of the tool, are sufficient to determine the constants that appear in the stress equations (3.1), (3.2) and (3.3). From Eqs. (3.17)

and (3.18), for each term i of the boundary load distribution there are four unknown constants and four equations, and therefore each of the 4x4 matrix equation are sufficient to determine the unknowns a_i, b_i, c_i and d_i. The number of arbitrary constants to be determined depends on the number of terms of the polynomial boundary load distribution. For a polynomial expression of degree n, the number of terms are $n+1$ and therefore $4(n+1)$ constants must be determined which can then be substituted into equations (3.1) to (3.3) to obtain the stress components.

The equations given here is used in the next section to determine stresses in cutting tools for a parabolic load distribution, and in Chapter 5 to determine stresses for a general polynomial load distribution.

3.3 Analytical cutting tool stresses for parabolic load distributions

The solution developed to determine stress distribution for the general polynomial load in the previous section is used here to solve the particular case of a parabolic load distribution. This is done to verify the stress distribution result obtained by Betaneli [7] and also to test the computer program results of the current study.

The experimentally determined normal boundary load distribution by Betaneli [7] (Section 2.3.2) has a parabolic distribution given by

$$\begin{aligned} \sigma &= \sigma_o - (\sigma_o / l_c^{\,n}) r^n \\ &= N_{r0} + N_{rn} r^n \end{aligned} \tag{3.19}$$

and the shear boundary stress distribution is determined from the normal boundary

stress as

$$\begin{aligned} \tau &= \mu\sigma_o - (\mu\sigma_o/l_c^n)r^n \\ &= S_{r0} + S_{rn}r^n \end{aligned} \tag{3.20}$$

From the above equations for σ and τ, the coefficients of the boundary stresses on the rake face are

$$\begin{Bmatrix} N_{r0} \\ N_{rn} \\ S_{r0} \\ S_{rn} \end{Bmatrix} = \begin{Bmatrix} \sigma_0 \\ -\sigma_0/l_c^n \\ \mu\sigma_0 \\ -\mu\sigma_0/l_c^n \end{Bmatrix} \tag{3.21}$$

The flank face is assumed to be free from loads and as a result N_{f0}, N_{fn}, S_{f0} and S_{fn} are zero. Substituting these coefficients into Eqs. (3.17) and (3.18), the equations that are sufficient to obtain the constants and therefore the stress distribution in cutting tools for the parabolic boundary load distribution assumption are

for $i = 0$

$$\begin{Bmatrix} \sigma_o \\ 0 \\ \mu\sigma_o \\ 0 \end{Bmatrix} = \begin{bmatrix} 2 & 2\theta_r & 2\cos 2\theta_r & 2\sin 2\theta_r \\ 2 & 2\theta_f & 2\cos 2\theta_f & 2\sin 2\theta_f \\ 0 & -1 & 2\sin 2\theta_r & -2\cos 2\theta_r \\ 0 & -1 & 2\sin 2\theta_f & -2\cos 2\theta_f \end{bmatrix} \begin{Bmatrix} a_0 \\ b_0 \\ c_0 \\ d_0 \end{Bmatrix} \tag{3.22}$$

for $i = n$

$$\begin{Bmatrix} -\sigma_o/{l_c}^n \\ 0 \\ -\mu\sigma_o/{l_c}^n \\ 0 \end{Bmatrix} = j \begin{bmatrix} \frac{\cos n\theta_r}{n} & \frac{\sin n\theta_r}{n} & \frac{\cos(n+2)\theta_r}{n} & \frac{\sin(n+2)\theta_r}{n} \\ \frac{\cos n\theta_f}{n} & \frac{\sin n\theta_f}{n} & \frac{\cos(n+2)\theta_f}{n} & \frac{\sin(n+2)\theta_f}{n} \\ \frac{\sin n\theta_r}{n+2} & -\frac{\cos n\theta_r}{n+2} & \frac{\sin(n+2)\theta_r}{n} & -\frac{\cos(n+2)\theta_r}{n} \\ \frac{\sin n\theta_f}{n+2} & -\frac{\cos n\theta_f}{n+2} & \frac{\sin(n+2)\theta_f}{n} & -\frac{\cos(n+2)\theta_f}{n} \end{bmatrix} \begin{Bmatrix} a_n \\ b_n \\ c_n \\ d_n \end{Bmatrix} \tag{3.23}$$

where,

$j = n(n+1)(n+2)$

$\theta_r = \gamma$

$\theta_f = \gamma + \alpha$

γ = rake angle

α = wedge angle

μ = coefficient of friction

n = exponent of the parabolic boundary load distribution

σ_o = applied normal stress at the cutting edge

l_c = contact length $a_0, b_0, c_0, d_0, a_n, b_n, c_n, d_n$ are the constants to be determined.

In the above equations a consistent sign convention for stresses must be used. Normal tensile stresses are positive. Positive shear stresses relative to the coordinate axes chosen are as shown in Fig. 2.15.

For given values of σ_0, contact length l_c, parabolic exponent n, average friction coefficient μ, rake angle γ and wedge angle α, the eight constants can be determined

by solving Eqs (3.22) and (3.23) simultaneously. The constants obtained can then be substituted into Eqs. (3.1) to (3.3) to determine the stress distribution in the loaded region of the cutting tool.

For expedience, these equations were programmed using Fortran and this program is given in Jemal [40] (Appendix C.1). The outputs from this computer program are the polynomial coefficients N_i, R_i and S_i; the component stresses σ_θ, σ_r and $\tau_{r\theta}$; and the principal stresses

$$\sigma_{1,3} = (\sigma_r + \sigma_\theta)/2 \pm \sqrt{(\sigma_r - \sigma_\theta)^2/4 + \tau_{r\theta}^2} \tag{3.24}$$

which can then be used to determine the region of maximum stresses and thus predict failure in the cutting tool.

For a given boundary load distribution and tool geometry, the stress distribution is independent of the choice of the coordinate axes and therefore the rake face can be taken as the x-axis by substituting $\gamma = 0$ (see Fig. 2.14). Thus, at the rake face $\sigma_\theta = \sigma_y$, $\sigma_r = \sigma_x$ and $\tau_{r\theta} = \tau_{xy}$.

The boundary load distribution used by Betaneli [7] (Section 2.3.2) is shown in Fig. 3.1. This boundary load distribution, as discussed in Section 2.5.2, is for a cutting condition having a contact length l_c=.5 mm, parabolic exponent n=3.3, friction coefficient μ=0.36 and average normal stress σ_{av}=60 kg/mm^2. For the parabolic boundary load distribution, the applied maximum stress at the cutting edge is related to the average normal stress by $\sigma_o = (n+1)\sigma_{av}/n$ (Eq. 2.15), therefore $\sigma_o = 78$ kg/mm^2. The wedge angle of the tool considered is 62^0, so $\theta_f = 62\pi/180$ radians. Substituting these values into Eqs. (3.22) and (3.23) yields

for $i = 0$

$$\begin{Bmatrix} -78.0 \\ 0.0 \\ -28.1 \\ 0.0 \end{Bmatrix} = \begin{bmatrix} 2 & 0.000 & 2.000 & 0.000 \\ 2 & 2.164 & -1.118 & 1.658 \\ 0 & -1.000 & 0.000 & -2.000 \\ 0 & -1.000 & 1.658 & 1.118 \end{bmatrix} \begin{Bmatrix} a_0 \\ b_0 \\ c_0 \\ d_0 \end{Bmatrix}$$

for $i = n = 3.3$

$$\begin{Bmatrix} 768.2 \\ 0.0 \\ 276.6 \\ 0.0 \end{Bmatrix} = \begin{bmatrix} 22.79 & 0.000 & 22.79 & 0.000 \\ -20.72 & -9.49 & 19.45 & -11.87 \\ 0.00 & -14.19 & 0.000 & -22.79 \\ -5.91 & 12.90 & -11.87 & -19.45 \end{bmatrix} \begin{Bmatrix} a_n \\ b_n \\ c_n \\ d_n \end{Bmatrix}$$

Solving the above equations simultaneously, the results obtained for the non zero constants are:

$$\begin{Bmatrix} a_0 \\ b_0 \\ c_0 \\ d_0 \end{Bmatrix} = \begin{Bmatrix} -14.7 \\ -15.8 \\ -24.3 \\ 21.9 \end{Bmatrix}, \qquad \begin{Bmatrix} a_n \\ b_n \\ c_n \\ d_n \end{Bmatrix} = \begin{Bmatrix} 19.8 \\ 1.8 \\ 13.9 \\ -13.3 \end{Bmatrix}$$

These constants are then substituted into Eqs. (3.1) to (3.3) to determine the stress components at any point (r, θ) of the cutting tool. From these stress components the principal stresses are determined using Eq. (3.24) and the maximum shear stress from

$$\tau_{max} = (\sigma_1 - \sigma_3)/2 \tag{3.25}$$

The analytical solution for the principal stress distribution in the loaded region is shown in Fig. 3.2. This figure shows the maximum principal stress distribution for different values of angle θ (see Fig. 2.14) as a function of distance from the cutting edge.

The rake face stress distributions from the analytical solution, together with the boundary loads, are shown in Fig. 3.3. In this figure σ_y and τ_{xy} are the normal and

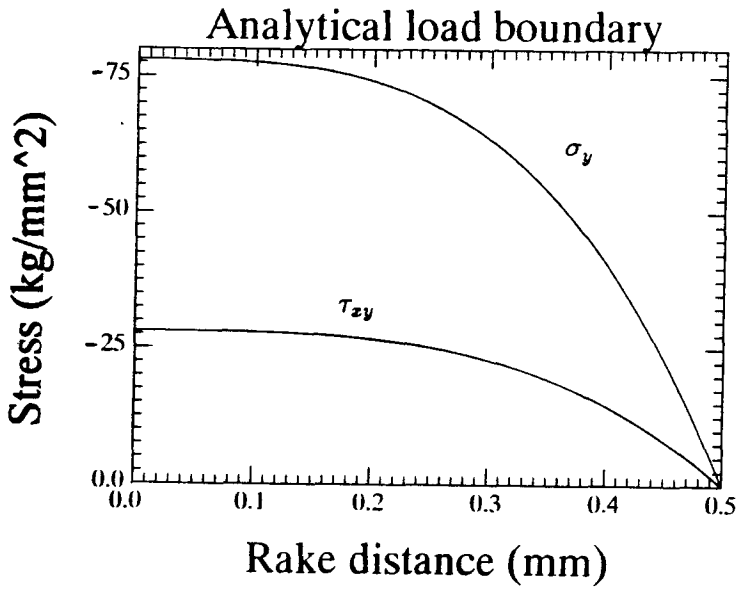

Figure 3.1: Polynomial boundary load distribution determined by photoelasticity at low cutting speeds, Betaneli [7]

shear boundary load distributions respectively and σ_x is the normal stress parallel to the rake face. This result predicts the maximum principal stress σ_1 at the cutting edge while giving zero stress at the end of chip-tool contact. This conclusion is identical with that given by Betaneli's [7] which is shown by the dashed curve labelled '1' in Fig. 2.18.

This result of a zero maximum principal stress at the end of chip-tool contact does not explain breakage of cutting tools that are observed in practice in this region. This result, as shown below, also does not agree with conclusions reached of stresses from the elastic deformation of the loaded region of the cutting tool. During cutting the loaded region of the cutting tool elastically deforms as shown in Fig. 3.4. As shown in this figure, the rake face locally bends about point A near the end of chip-tool contact, producing a bending stress (non zero tensile stress) at this point.

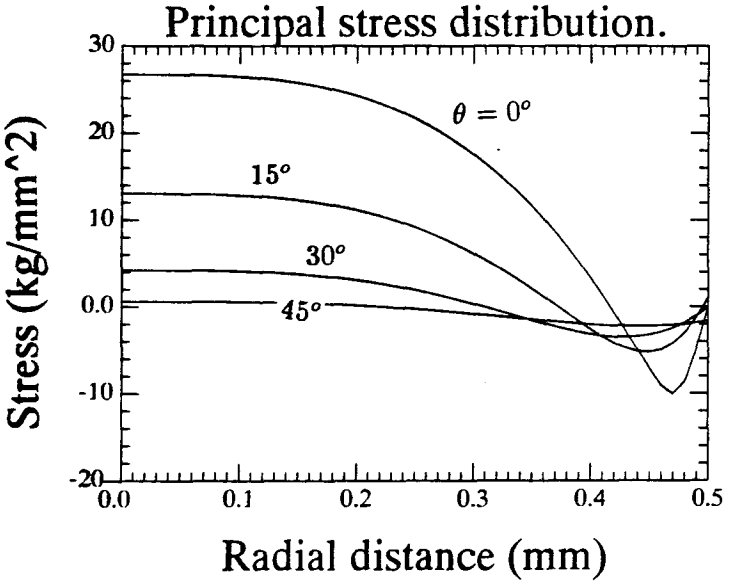

Figure 3.2: Analytical principal stress distributions in the loaded region of a cutting tool done to verify Betaneli's result

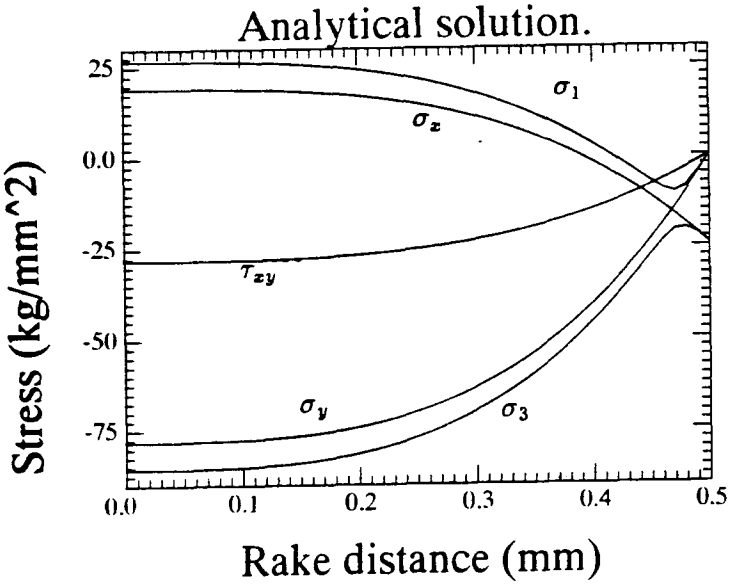

Figure 3.3: Analytical solution of rake face stresses for the parabolic boundary load distribution made to verify Betaneli's result

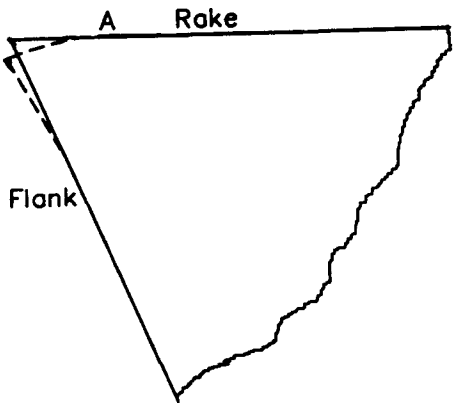

Figure 3.4: Elastic deformation of the loaded region of a cutting tool

Thus, the validity of Betaneli's [7] analytical result needs be investigated. To verify this result a finite element model as described in the next section is used.

3.4 Finite element cutting tool stress analysis for parabolic load distributions

In the previous section it was mentioned that the analytical solution obtained for the rake face principal stress distribution by Betaneli [7] does not explain cutting tool failure near the end of chip-tool contact and therefore this solution need be verified. To verify this analytical result the finite element method will be used.

One of the more powerful methods of numerical analysis is the Finite Element Method (FEM). By means of FEM, solutions can be obtained for a wide range of practical problems. The finite element method is described by Cook et al [8] and others. To assist in development of the finite element model, ANSYS [25] finite

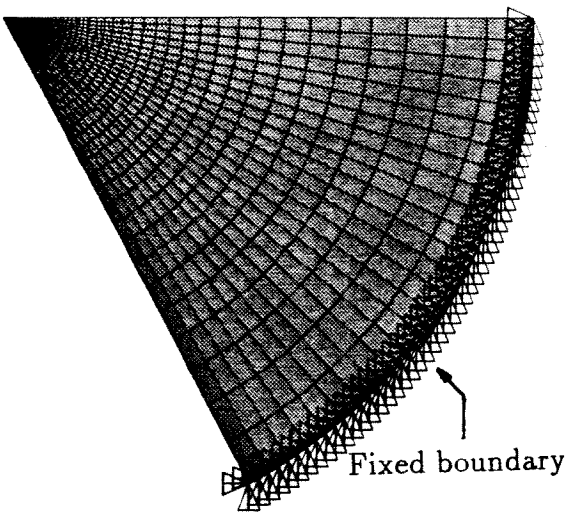

Figure 3.5: Finite element model of the cutting tool

element software was employed.

The finite element model of the tool developed in this study is shown in Fig. 3.5. The zero displacement boundary were applied at a radial distance of 1 cm from the cutting edge. This distance was chosen because its further increase does not have any significant effect on the accuracy of the FEM solution. A combination of two-dimensional quadrilateral and triangular isoparametric elements with mid-side nodes were used. These types of element were selected to obtain a reasonable representation of the steep stress gradient in the loaded region. These elements were generated automatically after the element sizes around the tool boundary were chosen. A magnified view of the loaded region of the tool is shown in Fig. 3.6. The finite element boundary load distribution in the loaded region was determined from the parabolic equations (2.12) and (2.16) at the mid-point of each element (Fig. 3.6) along the rake face. The normal stresses were applied directly to the element sides as

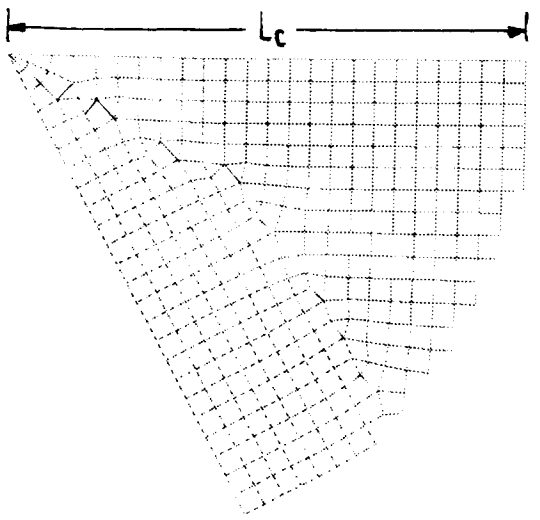

Figure 3.6: Finite element model of the loaded region of the cutting tool, contact length $=l_c$

pressures. The shear stresses were first converted to forces by multiplying them by the element length in the loaded region (0.02 mm in this case) and then were applied at the nodes. Very small elements were used to accurately represent the steep stress gradient that exists in the loaded region. The thickness of the tool was taken as unity.

The ANSYS finite element input data and other programs used in this analysis are given in Jemal [40] (Appendix C.2). The results of the FEM analysis for the principal stress distribution for the parabolic load distribution of Fig. 3.1 is shown in Fig. 3.7. This figure shows that the principal stress σ_1 at the rake face reaches its maximum at the end of chip-tool contact, and within the wedge it increases from flank face to the rake face.

The rake face stress distributions from the FEM solution together with the boundary load distributions (σ_y and τ_{xy}) are shown in Fig. 3.8. In this figure σ_x is the normal

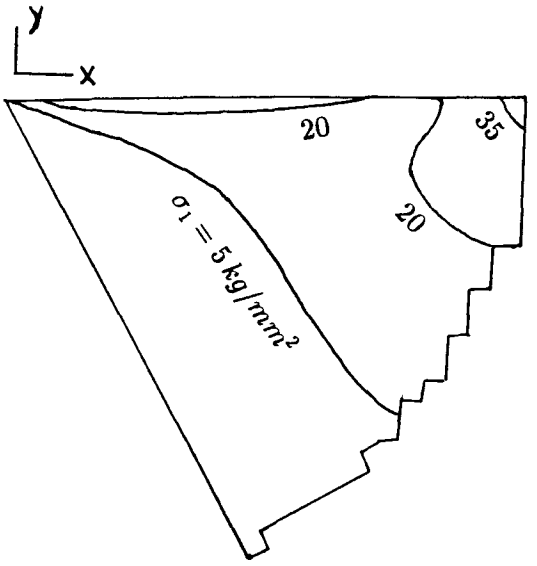

Figure 3.7: FEM solution for the maximum principal stress distributions in the loaded part of the tool for the boundary shown in Fig. 3.1

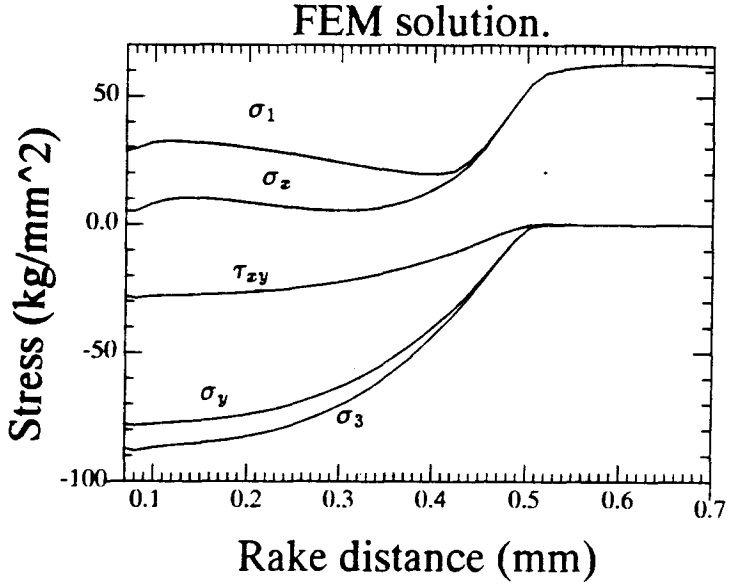

Figure 3.8: FEM solution for the rake face stresses for the parabolic boundary load distribution of Fig. 3.1, contact length $l_c = 0.5$ mm

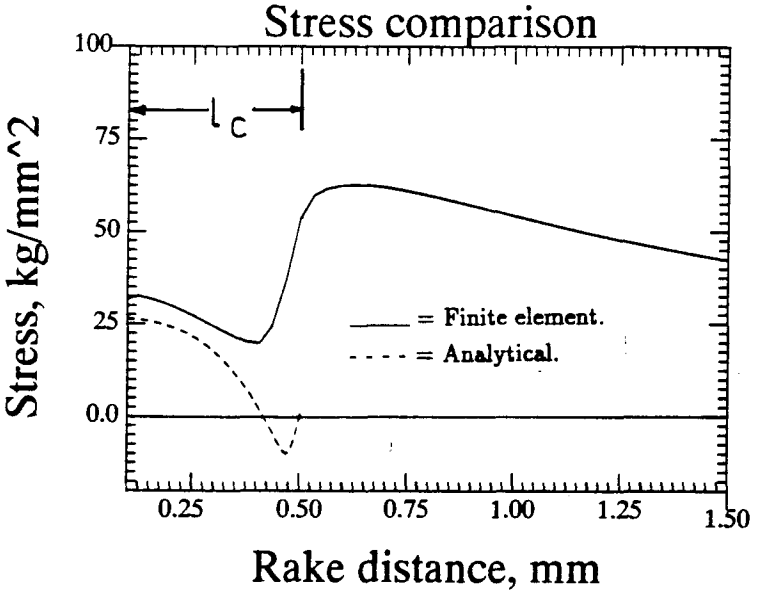

Figure 3.9: Comparison of FEM and analytical maximum principal stresses σ_1 along the rake face for the boundary shown in Fig. 3.1, contact length $l_c = 0.5$ mm

stress parallel to the rake face. The above FEM results and the analytical result of the previous section are compared in Fig. 3.9, and will be discussed in the next section.

3.5 Discussion and conclusions

From the analytical and FEM solutions obtained in the previous sections, the maximum principal stresses σ_1 on the rake face from the two solutions are compared in Fig. 3.9. From this figure, it is clear that the principal stress results from the analytical and FEM solution for the parabolic load distribution of Fig. 3.1 do not agree. The analytical solution shows the maximum principal stress at the cutting edge, while the numerical solution shows the maximum principal stress just after chip-tool contact length l_c. In addition, the maximum principal stress in the tool given by the numerical solution is more than two times that given by the analytical solution. The reason

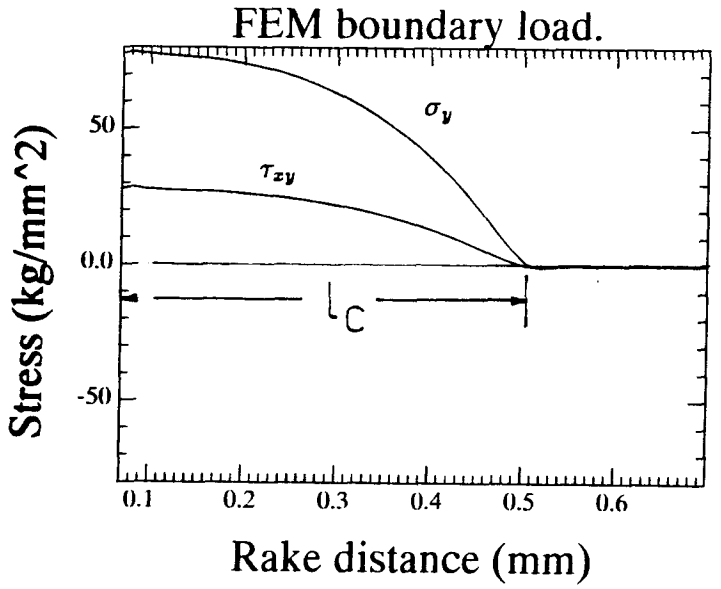

Figure 3.10: The FEM solution satisfies the boundary load conditions both in the loaded and free region of the rake face, contact length l_c = .5 mm

for this disagreement between the two solutions is explained below.

Since identical geometry were used in both solutions, clearly the geometry is not the cause of the difference in the results shown in Fig. 3.9. The next step should be to check to see if the applied boundary load distribution are the same *everywhere* in the tool for the two solutions.

Upon comparison in the loaded region, both the FEM and analytical boundary load distributions are the same. Outside of the loaded region, the finite element solution satisfies the zero boundary load conditions as shown in Fig. 3.10. To determine the boundary load distribution value taken by the analytical solution outside the region of chip-tool contact it is necessary to extrapolate the parabolic normal boundary curve of equation (2.12) beyond the chip-tool contact length $l_c = 0.5$ mm. This extrapolation is shown in Fig. 3.11 and this clearly does not satisfy the free

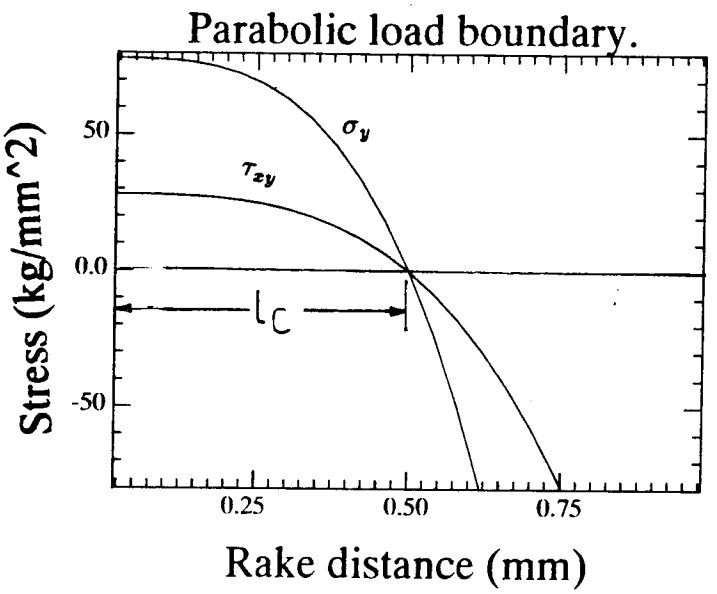

Figure 3.11: The Analytical solution does not satisfy the boundary load conditions in the free region of the rake face, contact length $l_c = .5mm$

boundary condition after chip-tool contact. It is this difference in applied boundary loading which is responsible for the difference between the analytical and FEM solutions. Thus, the comparison made was for two different problems where in the first (analytical) there is load after chip-tool contact while in the second (FEM) there is no load after chip-tool contact. To check this hypothesis, the extrapolated analytical boundary load distribution was applied on the FEM model. The finite element inputs for this problem are given in Jemal [40] (Appendix C.3) and the results are shown in Fig. 3.12. From this figure it can be seen that the two solutions are now in agreement. This result shows the analytical solutions can be used to determine stress distribution in a wedge geometry whose applied loading is continuous. However, when analytical solutions are used to determine the stress distribution in *cutting tools*, it should be made sure that the analytical expression chosen to represent the boundary

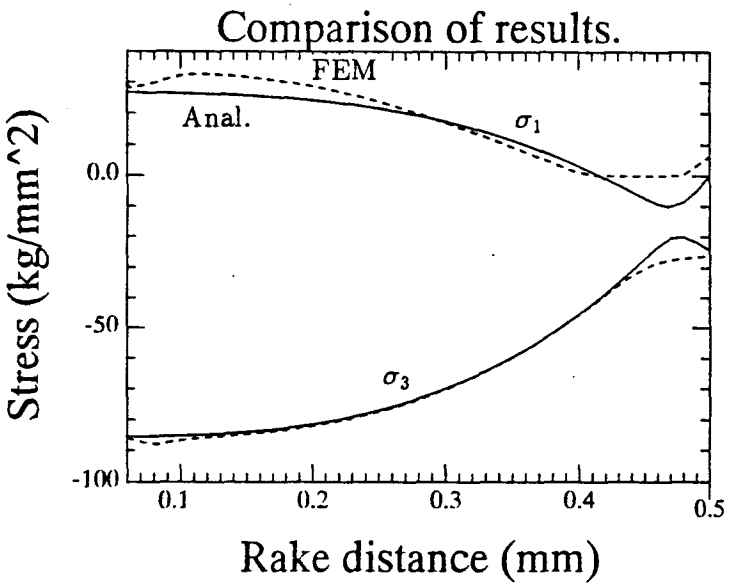

Figure 3.12: Comparison of FEM and analytical solutions for the boundary load distribution shown in Fig. 3.11

load distribution satisfy the zero loading condition after chip-tool contact, otherwise the solution obtained might be for an entirely unrealistic boundary load distribution where there are loads on the cutting tool after chip-tool contact.

The result of applying the boundary load distribution which does not satisfy the zero loading condition after the end of chip tool-contact is shown in Fig. 3.13. In this figure the position of the cutting edge before the load is applied was at the origin of the coordinate system. Thus, it can be seen that for this condition the cutting tool deforms upwards, i.e. *opposite* to the direction of the cutting force. Since Betaneli's [7] results were for a tool which behaved as shown in Fig. 3.13, his conclusions are incorrect. Further examination of Fig. 3.12 shows a negative maximum principal stress σ_1 near the end of chip-tool contact. This is because the analytical solution is based on the two-dimensional case and therefore does not include the zero principal

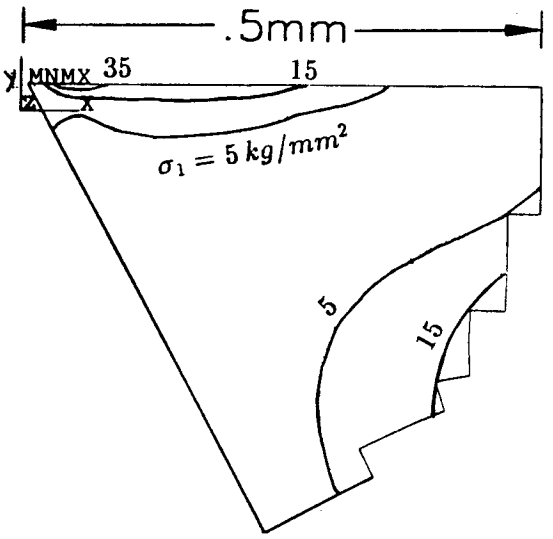

Figure 3.13: Tool deformation and maximum principal stress distribution for the boundary shown in Fig. 3.11

stress perpendicular to the plane of the tool when the value for the algebraically greatest stress σ_1 is calculated. Thus, whenever both the principal stresses in the plane of the tool, from the analytical solution, are negative then the maximum principal stress σ_1 should be zero as shown by the FEM solution.

Other conclusions that can be drawn from the results in this chapter are:

- Analytical and FEM solutions for the maximum principal stress at the cutting edge *do agree* (Figs. 3.9 and 3.12). This result supports Archibald's [6] analytical solution for cutting edge stresses.

- The maximum principal stress increases from flank face towards the rake face (Fig. 3.7).

In the boundary load distribution types shown in Fig. 3.10 there is a discontinuity

of slope at the end of chip tool contact, $l_c = .5$ mm. For these type of boundaries it is difficult to get a polynomial expression that can reasonably represent the curve shown in Fig. 3.10 both in the loaded and free regions of the rake face. However, for the boundary load distribution types of Amini [20] and Ahmad [21] as determined from photoelastic studies at higher cutting speeds (see Fig. 2.9), it is possible to get a polynomial expression which approximately satisfies the boundary condition both in the loaded and free region of the rake face. This is because in these particular boundary load distributions there is little discontinuity of slope at the end of chip-tool contact and therefore it can be approximated by a polynomial function. Then it can be proposed that for these types of boundary load distributions, the solutions from the analytical and FEM solutions will be close and as a result the analytical method could be used to determine the stress distribution in the loaded region of cutting tools. This is verified in the next chapter.

The split-tool dynamometer result by Barrow [16] shows reduced constant shear stress region (sticking region) with increase in cutting speed. Therefore for this case the shape of the boundary load distribution from the high speed photoelastic cutting and split-tool dynamometer are approximately similar (see Figs. 2.9 and 2.5). Thus, the high speed photoelastic boundary load distribution can be assumed to reasonably represent the boundary load distribution in metal cutting at higher cutting speeds.

Chapter 4

Stresses for Higher Speed Photoelastic Boundaries

4.1 Introduction

In Chapter 3 it was shown that when an analytical solution is used to determine cutting tool stresses, the analytical function chosen to represent the boundary load distribution should satisfy the zero loading condition after chip-tool contact. The photoelastic boundary load distribution at higher cutting speeds shown in Fig. 2.9 are almost tangent to the rake face at the end of chip-tool contact. For such a continuous distribution it is possible to fit a polynomial which can approximately satisfy the boundary condition both in the loaded and free regions of the rake face.

In this chapter, the stress distribution in a cutting tool for such polynomial boundary load distribution is determined analytically, and then these results are verified with numerical solutions. The result is compared with a photoelastic experimental result given by Amini [20] for a similar boundary load distribution and tool geometry. Finally, from the stress distributions obtained, the critical regions of the orthogonal cutting tool and its modes of failure will be discussed.

4.2 Analytical solution for high speed photoelastic boundary load distributions

The boundary load distribution determined from photoelasticity at higher cutting speeds by Ahmad [21], as discussed in Section 2.3.2, is given by

$$\sigma' = 2.91 - 1.53r' + .214r'^2 - .0033r'^3 \tag{4.1}$$

$$\tau' = 1.63 - 1.24r' + .315r'^2 - .0266r'^3 \tag{4.2}$$

where,

σ' = normal boundary stress on the photoelastic tool, kg/mm^2

τ' = shear boundary stress on the photoelastic tool, kg/mm^2

r' = rake face distance from the cutting edge of the photoelastic tool, mm.

In order to determine whether this polynomial boundary load distribution satisfies the free loading condition after chip-tool contact, these equations are plotted beyond the contact length of 4.5 mm in Fig. 4.1. From this figure, it can be seen that the free boundary conditions on the rake face are not satisfied. Therefore, Eqs. (4.1) and (4.2) as they are cannot be used as boundary conditions to determine the stress distribution in cutting tools. The second reason why these equations cannot be used directly in metal cutting tool stress analysis is because these boundary stresses were determined from photoelastic cutting test where the magnitude of the stresses are very low and the contact length is very high for metal cutting tools.

A boundary load distribution which approximately satisfies the boundary conditions in the free region of the rake face and having stress magnitudes experienced by metal cutting tools is shown in Fig. 4.2. The least squares method was used to

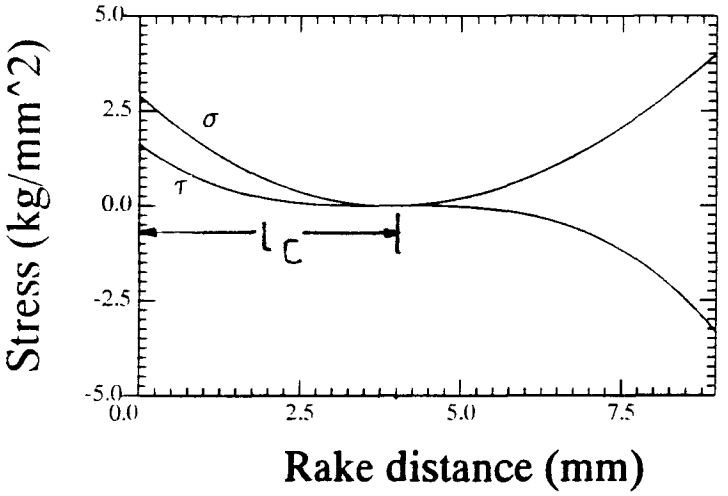

Figure 4.1: Ahmads's [21] polynomial functions for his photoelastic data do not satisfy the free boundary condition after chip-tool contact (l_c = 4.5 mm)

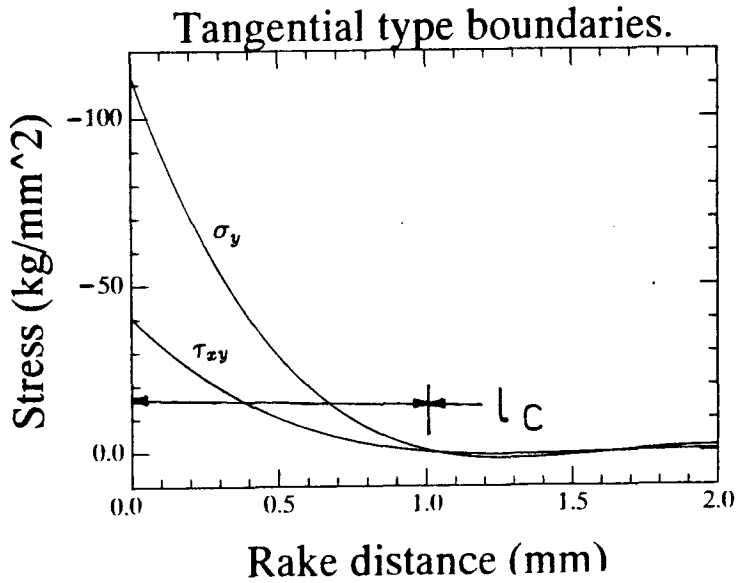

Figure 4.2: A polynomial function which approximately satisfy the free loading condition after chip-tool contact for a metal cutting tool (l_c = 1 mm)

determine the polynomial function which provides a satisfactory approximation of the free loading condition after chip-tool contact. In the determination of this boundary load distribution function, Zorev's [24] cutting data which gives a friction coefficient of 0.36 when cutting steel in water with a cutting tool having a rake angle 20^0 was taken. These data were used by Betaneli [7] in his analytical cutting tool stress analysis. This particular metal cutting condition was selected in this current study because it is similar to the cutting conditions used in photoelasticity and therefore the analytical results to be obtained could be compared with previous photoelastic results. The contact length and the width of cut were assumed to be 1 mm. At the cutting edge, the shear stress applied on the cutting tool was assumed to reach the yield shear strength of the workpiece material being machined, Fig. 2.3. For N.E. 9445 steel, the shear yield strength quoted by Merchant [26] is 40.5 kg/mm^2. This value was assumed as the applied shear stress value at the cutting edge. The shear stress and the normal stresses were assumed to obey the relation $\tau = \mu\sigma$. The equations for the boundary load distributions shown in Fig. 4.2 are given by

$$\sigma = -112.5 + 242.1r - 170.5r^2 + 38.4r^3 + 3.1r^4 - 1.5r^5 \tag{4.3}$$

$$\tau = -40.5 + 87.2r - 61.4r^2 + 13.8r^3 + 1.1r^4 - .5r^5 \tag{4.4}$$

or they could be represented in simplified form as:

$$\sigma = \sum_{i=0}^{5} N_{ri} r^i \tag{4.5}$$

$$\tau = \sum_{i=0}^{5} S_{ri} r^i \tag{4.6}$$

where,

$$\begin{Bmatrix} N_{r0} \\ N_{r1} \\ N_{r2} \\ N_{r3} \\ N_{r4} \\ N_{r5} \end{Bmatrix} = \begin{Bmatrix} -112.5 \\ 242.1 \\ -170.5 \\ 38.4 \\ 3.1 \\ -1.5 \end{Bmatrix}, \quad \begin{Bmatrix} S_{r0} \\ S_{r1} \\ S_{r2} \\ S_{r3} \\ S_{r4} \\ S_{r5} \end{Bmatrix} = \begin{Bmatrix} -40.5 \\ 87.2 \\ -61.4 \\ 13.8 \\ 1.1 \\ -0.5 \end{Bmatrix}$$

where,

σ = rake face normal stress distribution, kg/mm^2

τ = rake face shear stress distribution, kg/mm^2

N_{ri} = rake face normal load distribution coefficients

S_{ri} = rake face shear load distribution coefficients

r = rake face distance from cutting edge, mm.

From Fig. 4.2, it can be seen that there is a good approximation of the free boundary after chip-tool contact ($1 < r < 2$) mm and for this distribution analytical and FEM solutions will be compared. The FEM boundary can be made to satisfy the free loading conditions completely as shown in Fig. 4.3.

As described in Section 3.2, the arbitrary constants that appear in the stress equations (3.1) to (3.3) can be determined from the boundary conditions and the geometry of the tool using Eqs. (3.17) and (3.18). For quick reference Eqs. (3.17) and (3.18) are also given by Eqs. (4.7) and (4.8) below.

for $i = 0$

$$\begin{Bmatrix} N_{r0} \\ N_{f0} \\ S_{r0} \\ S_{f0} \end{Bmatrix} = \begin{bmatrix} 2 & 2\theta_r & 2\cos 2\theta_r & 2\sin 2\theta_r \\ 2 & 2\theta_f & 2\cos 2\theta_f & 2\sin 2\theta_f \\ 0 & -1 & 2\sin 2\theta_r & -2\cos 2\theta_r \\ 0 & -1 & 2\sin 2\theta_f & -2\cos 2\theta_f \end{bmatrix} \begin{Bmatrix} a_0 \\ b_0 \\ c_0 \\ d_0 \end{Bmatrix} \tag{4.7}$$

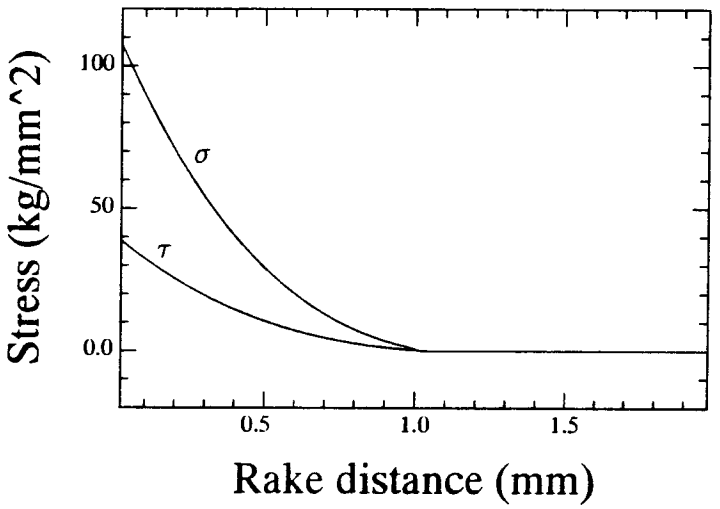

Figure 4.3: The FEM boundary completely satisfy the free loading condition after chip-tool contact ($l_c = 1mm$)

for $1 \leq i \leq n$

$$\begin{Bmatrix} N_{ri} \\ N_{fi} \\ S_{ri} \\ S_{fi} \end{Bmatrix} = j \begin{bmatrix} \frac{\cos i\theta_r}{i} & \frac{\sin i\theta_r}{i} & \frac{\cos(i+2)\theta_r}{i} & \frac{\sin(i+2)\theta_r}{i} \\ \frac{\cos i\theta_f}{i} & \frac{\sin i\theta_f}{i} & \frac{\cos(i+2)\theta_f}{i} & \frac{\sin(i+2)\theta_f}{i} \\ \frac{\sin i\theta_r}{i+2} & -\frac{\cos i\theta_r}{i+2} & \frac{\sin(i+2)\theta_r}{i} & -\frac{\cos(i+2)\theta_r}{i} \\ \frac{\sin i\theta_f}{i+2} & -\frac{\cos i\theta_f}{i+2} & \frac{\sin(i+2)\theta_f}{i} & -\frac{\cos(i+2)\theta_f}{i} \end{bmatrix} \begin{Bmatrix} a_i \\ b_i \\ c_i \\ d_i \end{Bmatrix} \tag{4.8}$$

where,

$j = i(i+1)(i+2)$

$\theta_r = \gamma$

θ_f $= \gamma + \alpha$

γ $=$ rake angle

α $=$ wedge angle

i $=$ powers of the polynomial

N_{ri} $=$ rake face polynomial normal load distribution coefficients

N_{fi} $=$ flank face polynomial normal load distribution coefficients

S_{ri} $=$ rake face polynomial shear load distribution coefficients

S_{fi} $=$ flank face polynomial shear load distribution coefficients

a_i, b_i, c_i and d_i for $i \geq 0$ are constants.

The calculation of the constants and then the stress distribution in the cutting tool is discussed below. The boundary conditions are already given by Eqs. (4.5) and (4.6), where the degree of the polynomial $n = 5$. The x-axis is taken along the rake face and therefore $\theta_r = 0$ (Fig. 2.14). The wedge angle is 62^0, so $\theta_f = 62\pi/180$ radians. The flank face is assumed to be free from loads, therefore, $N_{fi} = 0$ and $S_{fi} = 0$. Substituting these values into Eqs. (4.7) and (4.8) yields

for $i = 0$

$$\begin{Bmatrix} -112.5 \\ 0.0 \\ -40.5 \\ 0.0 \end{Bmatrix} = \begin{bmatrix} 2 & 0.000 & 2.000 & 0.000 \\ 2 & 2.164 & -1.118 & 1.658 \\ 0 & -1.000 & 0.000 & -2.000 \\ 0 & -1.000 & 1.658 & 1.118 \end{bmatrix} \begin{Bmatrix} a_0 \\ b_0 \\ c_0 \\ d_0 \end{Bmatrix}$$

for $i = 1$

$$\begin{Bmatrix} 242.1 \\ 0.0 \\ 87.2 \\ 0.0 \end{Bmatrix} = \begin{bmatrix} 6.000 & 0.000 & 6.000 & 0.000 \\ 2.817 & 5.298 & -5.967 & -0.627 \\ 0.000 & -2.000 & 0.000 & -6.000 \\ 1.766 & -0.939 & -0.627 & 5.967 \end{bmatrix} \begin{Bmatrix} a_1 \\ b_1 \\ c_1 \\ d_1 \end{Bmatrix}$$

. . . . . .

for $i = 5$

$$\begin{Bmatrix} -1.5 \\ 0.0 \\ -0.5 \\ 0.0 \end{Bmatrix} = \begin{bmatrix} 42.000 & 0.000 & 42.000 & 0.000 \\ 26.997 & -32.174 & 11.577 & 40.373 \\ 0.000 & -30.000 & 0.000 & -42.000 \\ -22.981 & -19.284 & 40.373 & -11.577 \end{bmatrix} \begin{Bmatrix} a_5 \\ b_5 \\ c_5 \\ d_5 \end{Bmatrix}$$

Solving the above equations simultaneously, the results obtained for the non zero constants are:

$$\begin{Bmatrix} a_0 \\ b_0 \\ c_0 \\ d_0 \end{Bmatrix} = \begin{Bmatrix} -21.2 \\ -22.7 \\ -35.1 \\ 31.6 \end{Bmatrix}, \begin{Bmatrix} a_1 \\ b_1 \\ c_1 \\ d_1 \end{Bmatrix} = \begin{Bmatrix} 33.3 \\ -11.0 \\ 7.1 \\ -10.8 \end{Bmatrix}, \ldots, \begin{Bmatrix} a_5 \\ b_5 \\ c_5 \\ d_5 \end{Bmatrix} = \begin{Bmatrix} -0.02 \\ -0.00 \\ -0.01 \\ 0.02 \end{Bmatrix}$$

These determined constants are then substituted into Eqs. (3.1) to (3.3) to determine the stress components at any point (r, θ) of the cutting tool. From these stress components, the principal normal stresses can be determined from Eq. (3.24, and the maximum shear stress from Eq. (3.25). For convenience, the above calculations were performed using a Fortran program which is given in Jemal [40] (Appendix D.1).

The analytical result for the principal stress distribution in the loaded region within the cutting tool is shown in Fig. 4.4. This result shows increase in principal stress from the flank face towards the rake face. The stress distributions along the rake face are shown in Fig. 4.5. In this figure σ_y is the applied normal load distribution, τ_{xy} is the applied shear stress distribution and σ_x is the normal stress parallel to the rake face. In the next section this analytic solution is compared to an FEM solution for the boundary load distribution shown in Fig. 4.3.

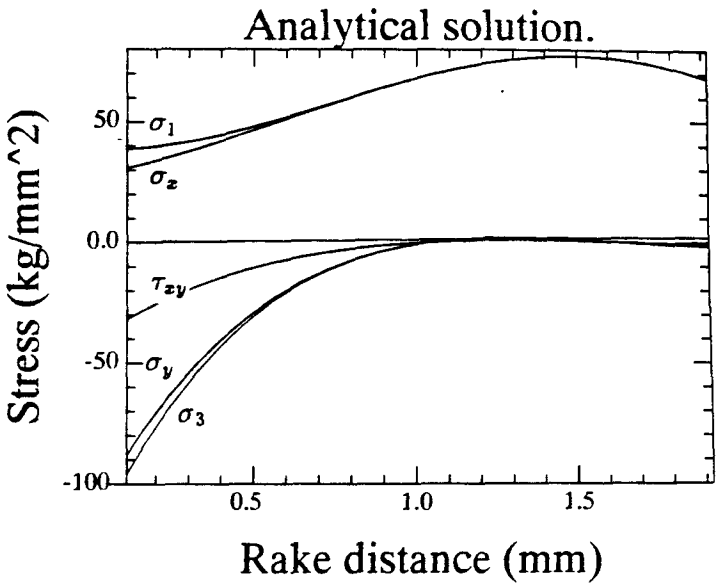

Figure 4.4: Analytical solution for the maximum principal stress distribution for the boundary shown in Fig. 4.2

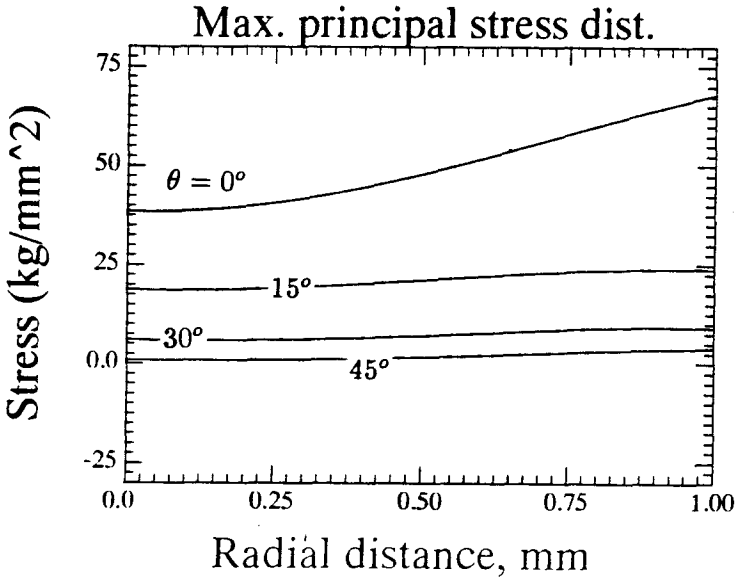

Figure 4.5: Analytical solution for rake face stresses for the boundary shown in Fig. 4.2

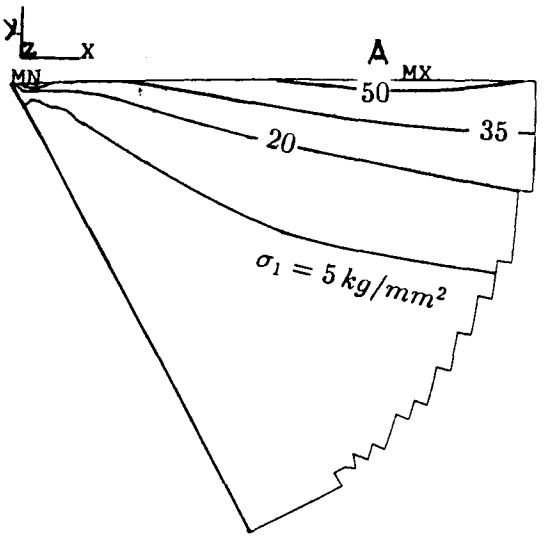

Figure 4.6: FEM solution for the maximum principal stress distribution for the boundary shown in Fig. 4.3

4.3 FEM solution for higher cutting speed photoelastic boundary load distributions

The FEM procedure described in Section 3.4 was again used to determine the stress distribution in a cutting tool for the boundary load distributions shown in Fig. 4.3. The finite element model used is shown in Figs. 3.5 and 3.6. The element length along the rake face in the loaded region was 0.04 mm. The input data files and other programs used in this analysis are given in Jemal [40] (Appendix D.2).

The FEM solution for the maximum principal stress in the loaded region, for the boundary load distribution of Fig. 4.3, is shown in Fig. 4.6. This result shows an increase in maximum principal stress magnitude from flank face towards the rake face. On the rake face, the principal stress is a maximum at the end of chip-tool

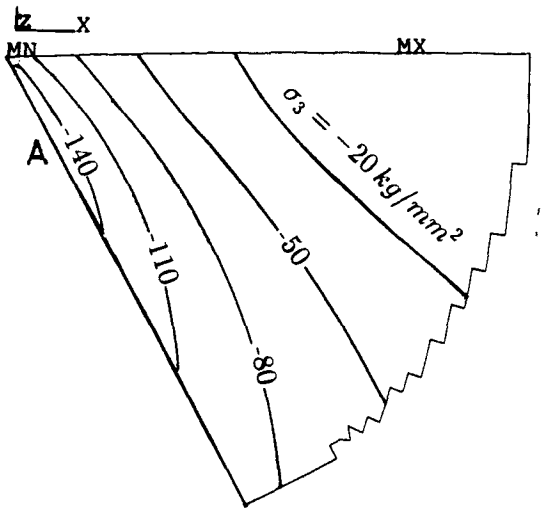

Figure 4.7: FEM solution for the minimum principal stress distribution for the boundary shown in Fig. 4.3

contact (point A). These conclusions agree with those given in Section 3.4. These two solutions were for two different types of boundary load distributions, but the location of the maximum principal stress from both solutions was found to be at the end of chip-tool contact.

The minimum principal stress distribution is shown in Fig. 4.7. This figure shows that the magnitude of the compressive stress is a maximum in the flank face close to the cutting edge (point A).

The FEM solutions of the rake face stress distributions are shown in Fig. 4.8. In this figure, σ_y is the applied normal load distribution and τ_{xy} is the applied shear stress distribution. The maximum principal stress reaches its maximum value at the end of chip-tool contact (l_c=1 mm) and then drops off gradually. A comparison between the analytical and FEM solution is shown in Fig. 4.9. This figure shows a satisfactory

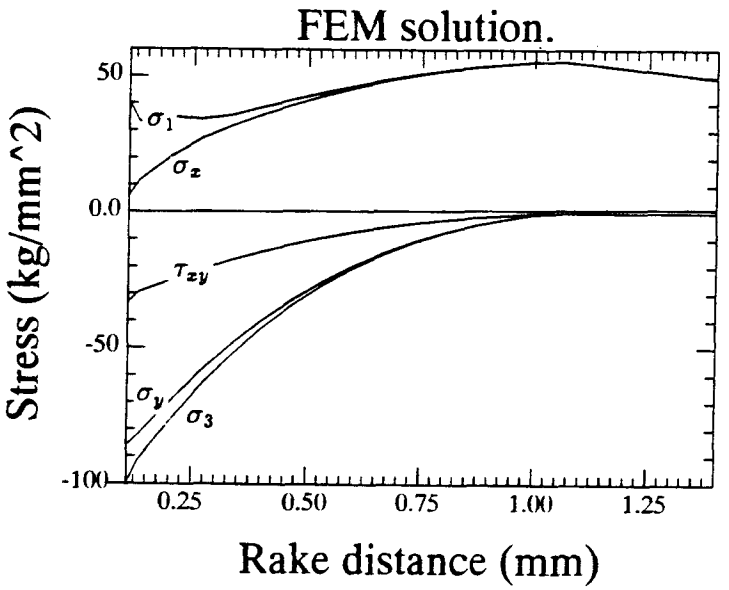

Figure 4.8: FEM solutions for rake face stresses for boundaries shown in Fig. 4.3

agreement between the two results and therefore indicates that analytical methods can be used to determine stresses in cutting tools for certain types of boundary load distributions with reasonable accuracy. The results obtained in the previous sections will be discussed in Section 4.6.

4.4 Point-load analytical solution for higher cutting speed photoelastic boundary load distributions

As discussed in Section 2.4.1, the point load analytical solution was used by Kaldor [2] to determine optimal tool geometry and by Chandrasekaran [3] to determine fracture stresses in milling cutters. The point load solution (Eq. 2.31) cannot be used to estimate stresses close to the cutting edge. In this section, the way in which the point load solution and the current analytical solution may together be used to estimate the stress distribution close to and far from the cutting edge is examined.

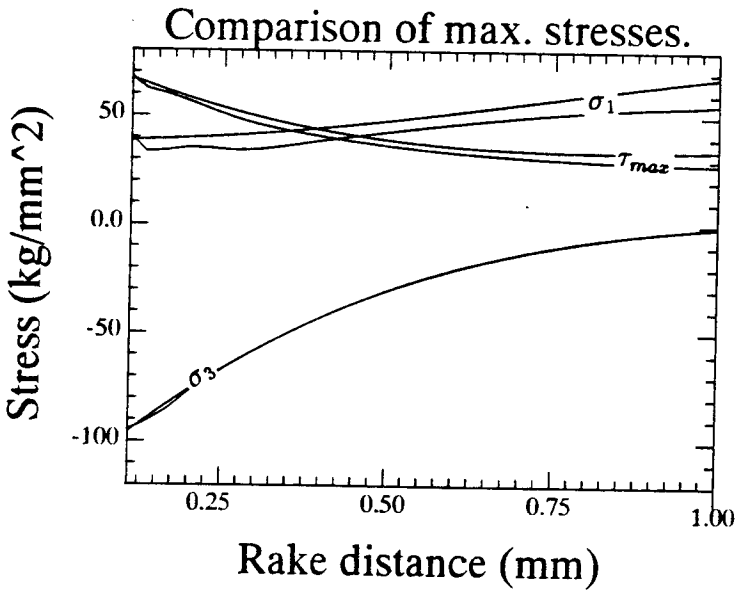

Figure 4.9: Comparison of analytical and FEM principal and maximum shear stress distributions for the boundary shown in Fig. 4.3

The maximum principal stress distribution σ_1 at the rake face from the point-load approximation (Eq. 2.31) is compared with the analytical and finite element solutions obtained in the previous sections in Fig. 4.10. The magnitude of the concentrated force P was calculated from the areas of the distributed shear and normal boundary stresses (Fig. 4.3 in this case). From Fig. 4.10, it can be seen that in the loaded region (rake distance < 1 mm) the point-load approximation provides a significantly less accurate result. However, after the chip-tool contact the result from the point-load approximation improves indicating that an estimate of the maximum principal stress in the cutting tool could be made by using the value of the point load solution where it intersects the current analytical distributed load solution (Fig. 4.10). The advantages of this method are that it is very simple to use, and the maximum principal stress is linearly related to the resultant cutting force by Eq. (2.31). Since the cutting force

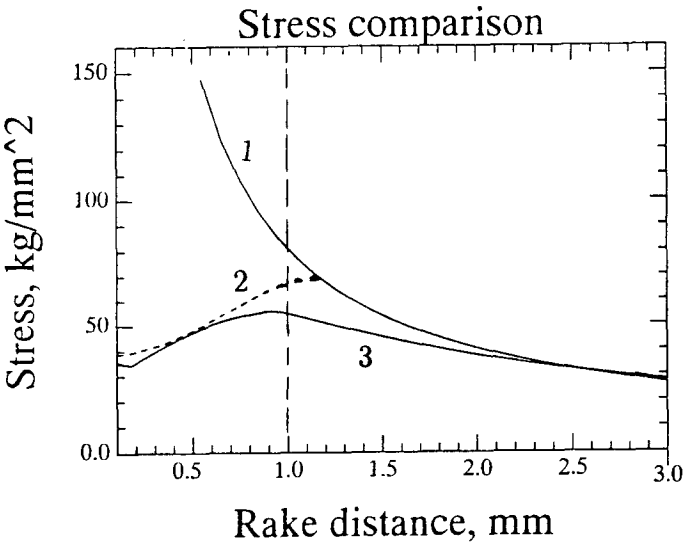

Figure 4.10: A comparison of rake face principal stress σ_1 by different methods for a 62^0 wedge angle and boundary load distribution shown in Fig. 4.3, chip-tool contact $l_c = 1$ mm

is also considered to be linearly related to the uncut chip thickness, the point load solution gives a linear relation between the uncut chip thickness and the maximum principal stress. This relationship can be used to determine the maximum uncut chip thickness (i.e. feed) corresponding to the allowable tensile stress of the tool material. Thus the current distributed analytical solution can be used to estimate the stress distribution in the loaded region while the point load distribution can be used to estimate the principal stress distribution outside the loaded region. This procedure provides a complete analytical solution for the prediction of the critical stresses that causes failure in the cutting tool.

It is noted from Fig. 4.10 that the maximum normal stresses given by the point-load solution are higher than the solutions given by the other methods. This feature can be explained by the fact that the resultant of the normal distributed boundary stresses which act at the distribution's centroid is instead applied at the cutting edge in the point-load solution. This results in a larger bending moment and consequently higher bending stresses. Thus the solution obtained from the above procedure for the critical maximum principal stress and its location on the rake face, as shown in Fig. 4.10, are higher than the numerical results.

In order to use the stress analysis results obtained in the previous sections to predict the critical regions of cutting tools and their types of failures, cutting tool failures will be considered next.

4.5 Failure in cutting tools

The two modes of failure of a loaded body are ductile and brittle failure. If the amount of permanent deformation occurring in the loaded body at rupture is large,

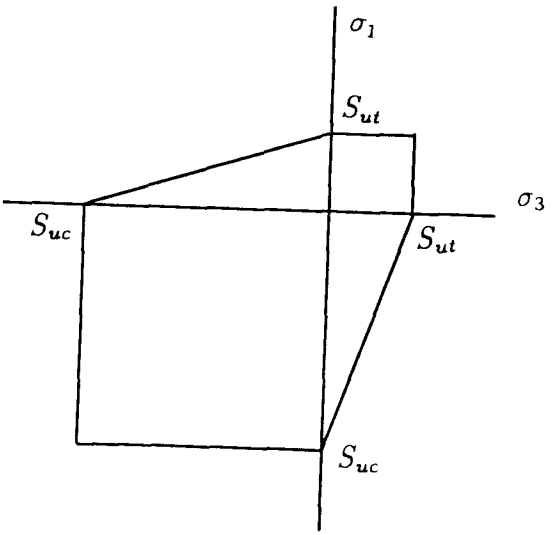

Figure 4.11: Fracture locus of a brittle material

the failure is ductile, if the deformation is small it is brittle.

Brittle failure

The Coulumb-Mohr theory is often used to predict fracture of brittle materials. This theory indicates that for plane stress conditions, $\sigma_2 = 0$, the loaded body is safe as long as (σ_1, σ_3) falls within the area shown in Fig. 4.11. In this figure, the ultimate compressive stress $|S_{uc}|$ is typically greater than the ultimate tensile strength S_{ut}. This is because flows such as microcracks or cavities which are present in materials weaken it in tension, while it does not appreciably affect its compressive strength.

When the principal stresses σ_1 and σ_3 at a critical point in the tool are both greater or equal to zero then the factor of safety $F.S = S_{ut}/\sigma_1$. If both the principal stresses are less than or equal to zero, the factor of safety $F.S = |S_{uc}|/|\sigma_3|$. When

$\sigma_1 > 0$ and $\sigma_3 < 0$, the equation to be used is

$$\frac{\sigma_1}{S_{ut}} + \frac{\sigma_3}{S_{uc}} = \frac{1}{F.S.} \tag{4.9}$$

In this equation both S_{uc} and σ_3 are negative quantities.

From the above discussion, the stresses to be considered for brittle failure of a cutting tool are the maximum principal stress σ_1 and the minimum principal stresses σ_3. Since in Fig. 4.9, the results obtained in the loaded region from the analytical and numerical solutions are similar, either solution can be used to determine the critical regions of the cutting tool. The principal stress distributions are shown in Figs. 4.6 and 4.7, where the critical points are shown by point A in both figures. These results can be explained from the elastic deformation of the loaded region. During cutting, the loaded region of the cutting tool deforms as shown in Fig. 3.4 and results in the shortening of the flank face close to the cutting edge and bending of the rake face at a point near the end of chip tool contact. The shortening of the flank face results in the minimum principal stress to be in this face close to the cutting edge as shown in Fig. 4.7. The rake face bending about the point near the end of chip-tool contact results in the maximum principal stress to be at this point as shown in Fig. 4.6. Inside the cutting tool wedge, the stresses are within these two extreme values increasing algebraically from the flank face towards the rake face. From Figs. 4.6 and 4.7, since the maximum stresses occur on free surfaces, the other principal stresses at these critical points are zero.

From the principal stress distributions shown in Figs. 4.6 and 4.7 the ratio of the critical minimum principal stress to the critical maximum principal stress is 2.7. This ratio, when compared with the ratio of the compressive strength to tensile strength of the tool material used, provides an indication of whether the tool failure is due to

compressive stress on the flank face close to the cutting edge, or due to maximum tensile stress near the end of chip-tool contact. If the ratio of the critical compressive stress to the critical tensile stress is assumed not to vary with change in cutting forces, then when the magnitude of the critical maximum principal stress $\sigma_1 = S_{ut}$ (say) then the magnitude of the critical compressive stress $\sigma_3 = 2.7S_{ut}$. Also, if the tensile strength of the tool material is S_{ut} and its compressive strength $S_{uc} = NS_{ut}$, then the factor of safety for tool failure due to maximum principal stress is $F.S_{\sigma_1} = S_{ut}/\sigma_1 = 1$, and the factor of safety for tool failure due to minimum principal stress is $F.S_{\sigma_3} = S_{uc}/\sigma_3 = N/2.7$. When $F.S_{\sigma_1} > F.S_{\sigma_3}$, the tool fails due to compressive stresses, while when the inequality is reversed it fails due to tensile stresses. Therefore, when $N = S_{uc}/S_{ut}$ for the tool material is lower than 2.7, then the tool fails due to critical compressive stress at the cutting edge and if higher it fails due to critical tensile stress at the end of chip-tool contact. For example, the typical ratio of the compressive strength to the tensile strength of high-speed steel is 2, of carbide is 3 and that of ceramics is 5 (Loladze [37]). From these values, for the boundary load distribution and tool geometry considered in this study ($\sigma_3/\sigma_1 = 2.7$), the high-speed steel fails due to maximum compressive stress at the cutting edge while both the carbide and ceramic tools fail due to the maximum tensile stress near the end of chip-tool contact. This result explains why tool materials that have low tensile strength (carbides, ceramics and diamond) are used only with robust tool geometry (large wedge angles or low rake angles) where the maximum tensile stresses are low. The above analysis is an example of the use of cutting tool stress distributions in selection of tool material properties.

With increase in depth of cut in the carbide and ceramic tools, cracks initiate

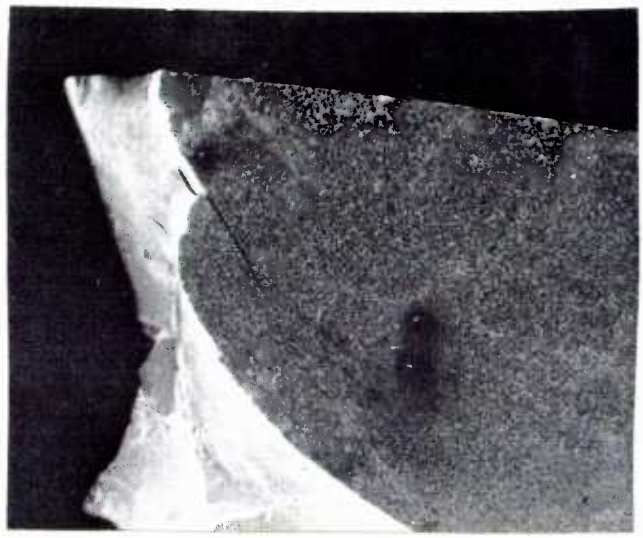

Figure 4.12: Brittle failure of a cutting tool near the end of chip-tool contact, Tlusty [27]

near the end of chip tool contact, point A in Fig. 4.6, due to maximum principal stresses and results in breakage of the whole loaded region of the cutting tool. A photograph by Tlusty [27] which shows this failure of the whole loaded region of a carbide cutting tool due to maximum tensile stresses is shown in Fig. 4.12. Failure due to compressive stresses result in permanent deformation of the cutting edge as shown in Fig. 4.13, Wright [36]. Thus the analytical results obtained for tool failures correlate well with observed cutting tool failures and this verifies the approach used in this study.

Experimental investigations by Trent [34] show, cutting tool materials loose their strength with increase in temperature. Therefore, the effect of temperature on the properties of the tool material should be taken into account when failure analysis of the cutting tool is performed.

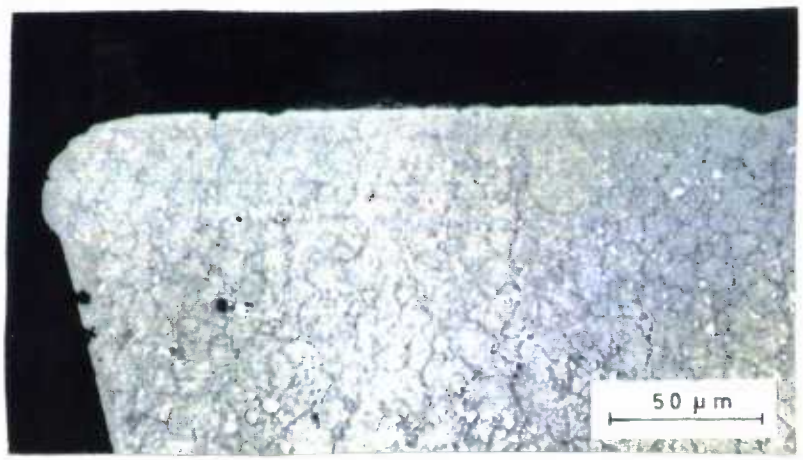

Figure 4.13: Cutting edge deformation due to maximum compressive stress, Wright [36]

Ductile failure

The theory of failure commonly used to predict ductile failure is the *von Mises-Hencky theory.* According to this theory, also known as the distortion energy theory, a loaded body is safe as long as the maximum value of the elastic distortion energy per unit volume in that material remains smaller than the distortion energy per unit volume required to cause yield in a tensile-test specimen of the same material. For the plane stress case this theory indicates that a loaded body is safe as long as $\sigma_{eq} < S_y$, where

$$\sigma_{eq} = \sqrt{\sigma_1^2 - \sigma_1\sigma_3 + \sigma_3^2} \tag{4.10}$$

where,

σ_1, σ_3 are the algebraically largest and smallest stresses

σ_{eq} = an equivalent stress

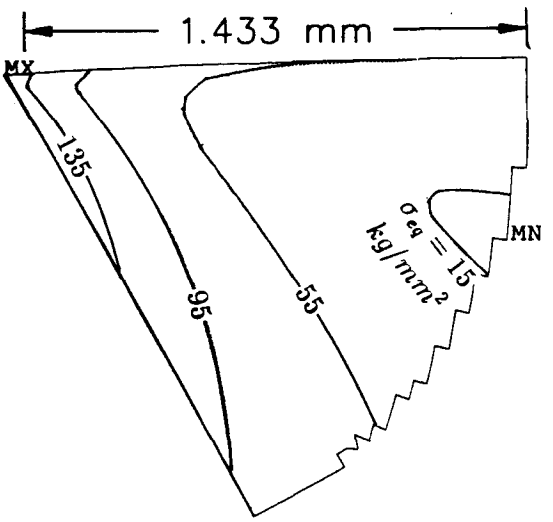

Figure 4.14: Equivalent stress contour lines for the boundary shown in Fig. 4.3

S_y = yield tensile strength of the material.

To determine the ductile cutting tool failure regions, the equivalent stress contour lines in the loaded region were plotted and are shown in Fig. 4.14. The results in this figure can be explained from the maximum and minimum principal stress distributions shown in Figs. 4.6 and 4.7. At a free surface the equivalent stress is proportional to the non zero principal stress. Since the magnitude of the minimum principal stress close to the cutting edge in Fig. 4.7 is about three times the maximum principal stress at the end of chip tool contact in Fig. 4.6, the equivalent stress therefore will be maximum near the cutting edge as shown in Fig. 4.14.

From Fig. 4.14, it can be seen that the region of maximum distortion energy is close to the cutting edge. Near the cutting edge the temperature is very high and this reduces the strength of the tool and increases its ductility and results in the shearing of the cutting edge which is known as edge chipping. A photograph by Tlusty [27]

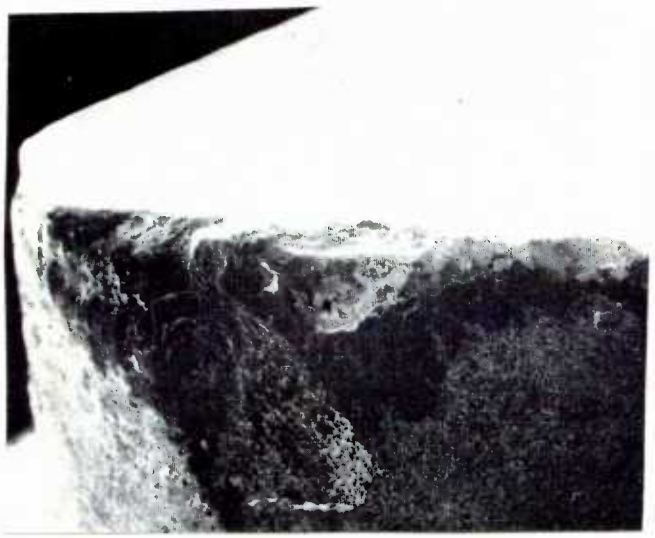

Figure 4.15: cutting edge chipping, Tlusty [27]

which shows chipping of the cutting edge is shown in Fig. 4.15. It is interesting to see the good correlation between the equivalent stress lines in Fig. 4.14 and the profile of the chipped surface.

To complete the failure analysis of the cutting tool its stress at the shank where it is attached to the tool post needs to be considered. This was done by considering the bending stresses at the fixed end for a width of cut of 5 mm. This analysis for the tool geometry shown in Fig. 4.16 shows the maximum tensile stresses near the cutting edge is four times the bending stress at the fixed end (point A). This result shows shank design is not only based on cutting tool breakage at the fixed end but also is based on the rigidity of the tool.

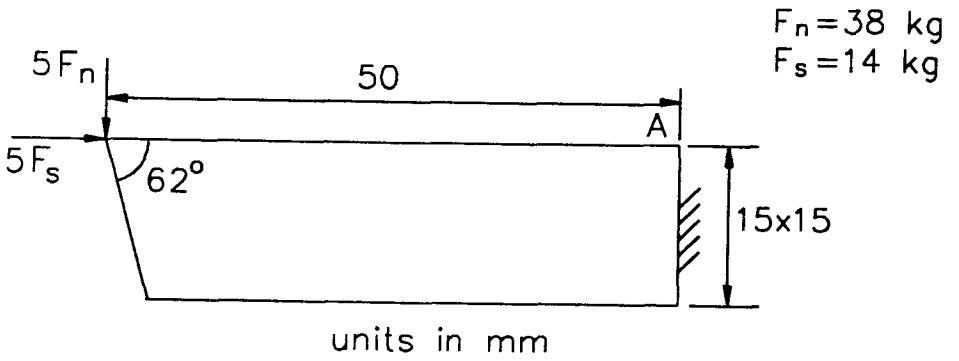

Figure 4.16: Bending stress calculation at the fixed end (point A) of a cutting tool

4.6 Discussions and conclusions

In the above sections, both analytical and FEM cutting tool stress distributions for high speed photoelastic boundary load distribution were determined. The results for the principal stresses and maximum shear stress distribution from both solutions in the loaded region are in good agreement. The results are identical at the cutting edge (verifying Archibald's [6] result), however, further from the cutting edge the difference between the two solution increases. The value for this difference at half the chip-tool contact length is 8% for the maximum principal and shear stresses. The results for the minimum principal stress are almost identical everywhere in the loaded region. If the boundary conditions after the tool-chip contact were completely satisfied then the above differences would vanish.

From Fig. 4.9, the analytical solution for the distributed boundary load gives a

similar result to the finite element solution in the loaded region where the stresses are most critical. Therefore, either solution can be used to predict the failure regions and their mode of failure of the cutting tool. From these results it was found that the maximum principal stress in the cutting tool occurs on the rake face (Fig. 4.6) and the minimum principal stress on the flank face (Fig. 4.7). These results can be explained from the local deflection of the loaded region shown in Fig. 4.18. Due to cutting forces the *loaded region* bends downwards about point A creating a maximum bending stress (tensile) at this point. On the other hand, the flank face, as shown in the figure, shortens and is therefore under compression. Thus cutting tool failures are either at the cutting edge or near the end of chip-tool contact. At the cutting edge the failures are either due to maximum shear stress (Fig. 4.14) which causes cutting edge chipping as shown in Fig. 4.15, or due to maximum compressive stress (Fig. 4.7) which causes permanent deformation of the cutting edge as shown in Fig. 4.13. At the end of chip tool contact the failure is due to the maximum tensile stresses (Fig. 4.6) which causes initiation of cracks at this point and results in the fracture of the whole loaded region of the cutting tool as shown in Fig. 4.12.

The stress distribution at the rake face from the analytical and finite element solutions were compared with point-load elasticity solutions. This comparison is shown in Fig. 4.10. From this figure the two analytical solutions together can be used to determine the stress distribution in a cutting tool, where the distributed load solution is used in the loaded region while the point load solution is used after the loaded region. It is interesting to note that after twice the contact-length the result from the point load solution and finite element solution in Fig. 4.10 are in agreement and therefore in this region the point load solution is very satisfactory.

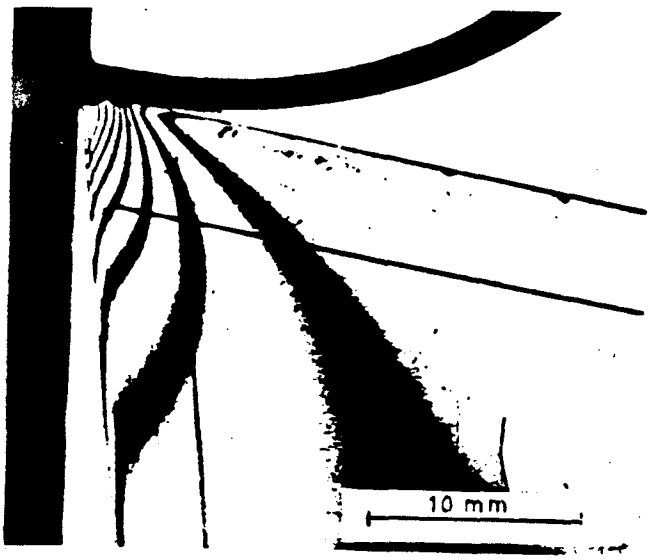

Figure 4.17: Maximum shear stress distribution from photoelasticity , Amini [20]

The stress distribution obtained can also be compared with a photoelastic result by Amini [20]. The photoelastic result is shown in Fig. 4.17. In this figure the isochromatics or fringe patterns (see Section 2.3.2) are proportional to maximum shear stress lines. Amini used a tool having a wedge angle of 76^0, but the analysis made in this study was for a 62^0 wedge angle. Therefore, in order to get good comparison of our solution with the experimental result the analysis was repeated for a wedge angle of 76^0. The contour lines which are equal to twice the maximum shear stress, obtained for the boundary load distribution of Fig. 4.3 and wedge angle of 76^0, are shown in Fig. 4.18. Comparison of this figure with Fig. 4.17 shows the experimental and maximum shear stress contour lines of this study agree verifying the proposed solution.

To see the effect of the wedge angle on stresses in a cutting tool, minimum principal

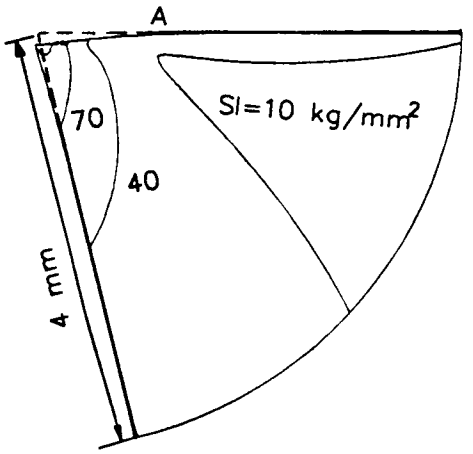

Figure 4.18: Twice the maximum shear stress distribution obtained for the photoelastic cutting boundary of Fig. 4.3

stresses at the flank face and maximum principal stresses at the rake face for two wedge angles (62^0 and 76^0) were compared. This comparison is shown in Fig. 4.19. This figure shows the effect the wedge angle has on the principal stresses distribution. At the end of chip-tool contact length, $l_c = 1$ mm, the maximum principal stress has decreased by 60% for the same boundary load distribution with the increase in the wedge angle. This result explains why tool materials having low transverse rupture strength (like carbide, ceramics and diamonds) are made with higher wedge angles or have low rake angles. At the cutting edge, with the increase in the wedge angle for the same boundary load distribution the magnitude of the minimum principal stress has decreased by 45%. These are the reasons why rough cutting operations are performed using tools that have high wedge angles.

Close to the cutting edge the temperatures and the compressive stresses are very

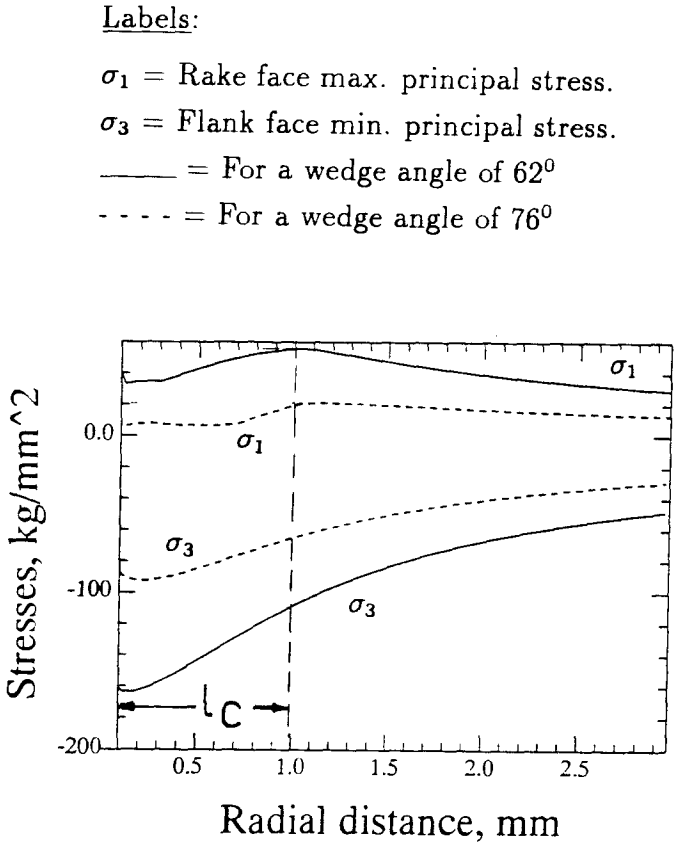

Figure 4.19: Effect of change in wedge angle on the critical principal stresses of a cutting tool

high, and therefore tool materials that maintain their compressive strength at this high temperature are superior. This is the main reason why carbide tools are better than high speed steel tools in their cutting performance.

This chapter is summarized by listing the important results obtained:

- An analytical stress distribution in a cutting tool which agrees with numerical and previous experimental results for the high speed photoelastic boundary load distribution was obtained.

- From the solutions obtained the failure regions of the cutting tool and their modes of failure were identified. These failure predictions were found to correlate well with observed cutting tool in-service failures.

Chapter 5

Stress Analysis of an End Mill

5.1 Introduction

Maximum production in metal cutting requires a large chip load. However, at very high chip loads breakage of the cutting tool may occur. Therefore, to select the optimum cutting condition (maximum cutting force) for maximum production, without the danger of tool breakage, knowledge of the relationship between cutting tool forces and tool stresses is required. These stress distributions also help to predict the location and types of failures in the cutting tool.

The stress distribution in an end mill can be determined using numerical methods, however, these methods require much time and effort. Analytical solutions may not have these shortcomings, and therefore the possible use of analytical solutions in end mill stress analysis is investigated.

An end mill could fail in two ways due to stresses developed in the tool during cutting. It could fail at the shank section due to excessive bending stresses or it could fail within the flutes where the cutting forces are applied. Thus, both of these critical regions must be considered for potential failure of the end mill.

The cutting force distribution along the flutes of the end mill must be known to

determine the stress distribution in an end mill. When the stress distribution far away from the cutting edges (shank stresses) are required, the cutting forces can be assumed to be distributed as concentrated forces along the cutting edge. However, when stresses close to the cutting edge are required, then the actual cutting force distributions across tool-chip contact along the cutting edge (like those determined from photoelastic cutting) must be used.

Once the cutting force distribution and the geometry of the end mill are selected, the stress distribution in the tool (at the shank or the flute) may be determined analytically or numerically. The analytical solution to be obtained in this study will be verified with numerical solutions. In the literature there is little work done on end mill stress analysis, while there is sufficient work done on end mill deflection and cutting force analysis. In the end mill *shank* stress analysis, the cutting force distribution models established in the literature will be used. The critical regions for shank breakage obtained in this study will be compared with shank failure regions observed in practice. Shank stress analysis will be considered in Section 5.2.

In end mill flute stress analysis, the stresses required are close to the application of the cutting forces. In this case, the actual force distribution across tool-chip contact must be used. Photoelastic cutting force distributions will be used in these flute stress analysis. From the two-dimensional stress analysis done in the previous chapters, it was seen that the critical stresses occur close to the loaded region, because further from the loaded region the load resisting area or section modulus of the wedge increases and this reduces the magnitude of the stresses. Thus, in the end mill flute stress analysis only a portion of the end mill close to the loaded region will be considered. Finite element solutions of flute stresses are obtained, and they will be compared with the two-dimensional solutions. End mill flute stress analysis

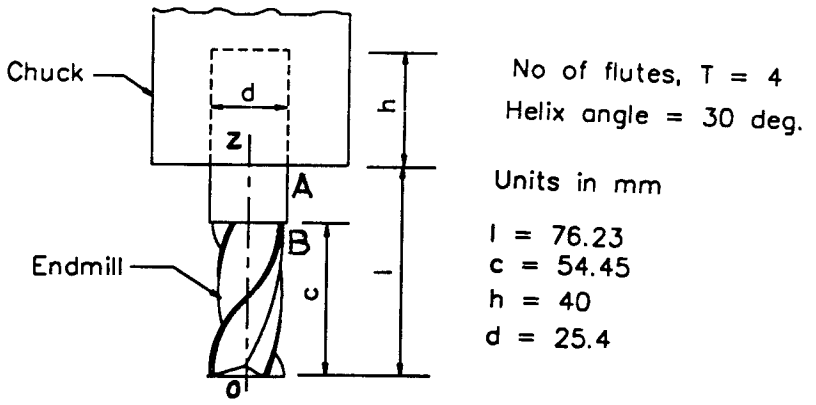

Figure 5.1: Schematic diagram of an end mill

is considered in Section 5.4.

5.2 Shank stresses in an end mill

5.2.1 Force distribution along end mill cutting edge

Fig. 5.1 shows a schematic diagram of an end mill and Fig. 5.2 shows its cutting operation.

When stress predicitions in the shank of an end mill are required, the section is further from the application of the cutting forces and therefore these stresses can be determined from the resultant cutting force on the tool. The resultant cutting force F on the tool acts at a distance a from the fixed end of the cutter as shown in Fig. 5.2. This resultant force can be calculated using the force distribution model of Kline et al [28], an example of which is shown in Fig. 5.3. In this figure, the forces shown are the radial and tangential forces which act on each axial elements of the end mill and

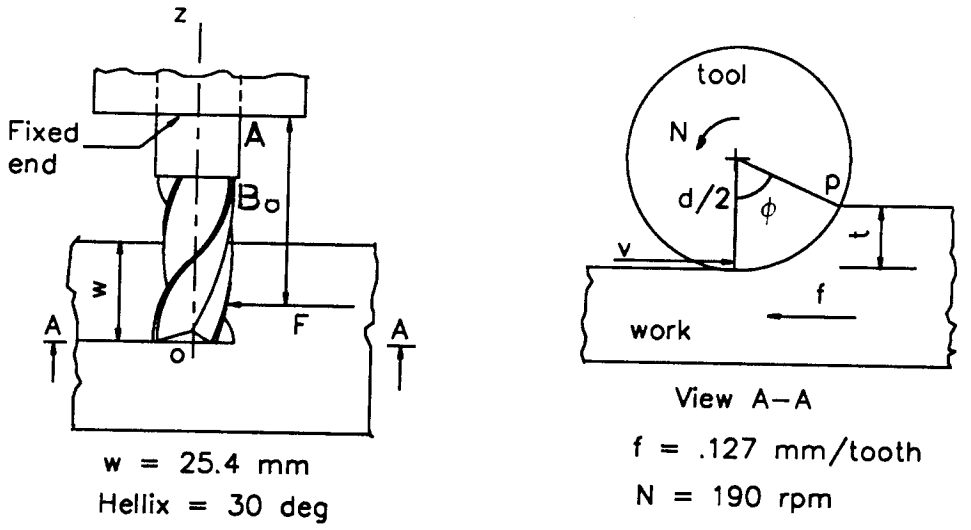

Figure 5.2: Schematics for the cutting operations of an end mill

which vary in magnitude and direction along the cutting edge. From these elemental forces the resultant cutting force F and its point of application a can be determined.

In the end mill cutting edge force distribution model (also called mechanistic model), the three-dimensional milling operation is assumed to be equivalent to an aggregation of orthogonal cuts by each axial elements of the cutter. On each axial element, as shown in Fig. 5.4, the tangential elemental cutting force is proportional to the radial depth of cut δr and the axial length of the element δz. From this figure the radial depth of cut is related to the feed rate per tooth f by $\delta r = f \sin\theta$, where θ is the position of the cutting edge of the axial element measured from the normal to the finished surface. Therefore, the elemental tangential force is given by

$$\delta F_t = K_t f \delta z \sin\theta \tag{5.1}$$

where,

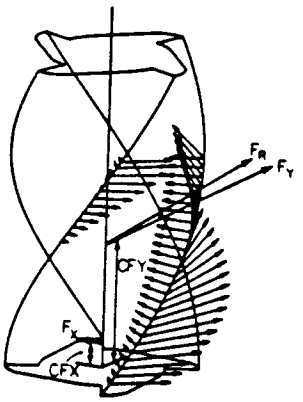

Figure 5.3: Cutting force distribution along the cutting edges of an end mill, Kline [28]

K_t = tangential force constant, MPa

The elemental radial force is proportional to the elemental tangential force and thus can be written as

$$\delta F_r = K_r \delta F_t \tag{5.2}$$

where,

K_r = radial force constant.

Kline [28], has shown that the tangential and radial force constants depend on the cutting conditions, which are mainly the feed rate, the radial depth of cut and the axial depth of cut. For the cutting conditions and the standard end mill geometry shown in Figs. 5.1 and 5.2, the values of the force constants for steel workpiece from Kline [28] are K_t = 2660 MPa and K_r = .553. These values are used in the shank

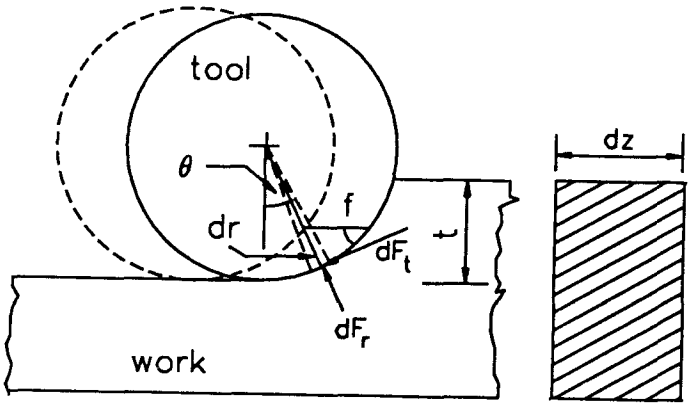

Figure 5.4: Definition of terms used in elemental force calculation

stress analysis presented here.

In Eq. 5.1, to determine the elemental tangential force, the angle θ shown in Fig. 5.4 for each axial element along the cutting edge should be determined. This angle can be determined from the equation for the swept angle ϕ of the cutter tooth shown in Fig. 5.2. The swept angle is measured about the cutter axis and is defined as the angle swept from the beginning of a cut to the end of the cut by one tooth of the end mill in one revolution. The swept angle ϕ, from the geometry of Fig. 5.5, is given by

$$\phi = \frac{360w \tan \psi}{\pi d} \tag{5.3}$$

where,

w = axial depth of cut, mm

ψ = helix angle

d = cutter diameter, mm

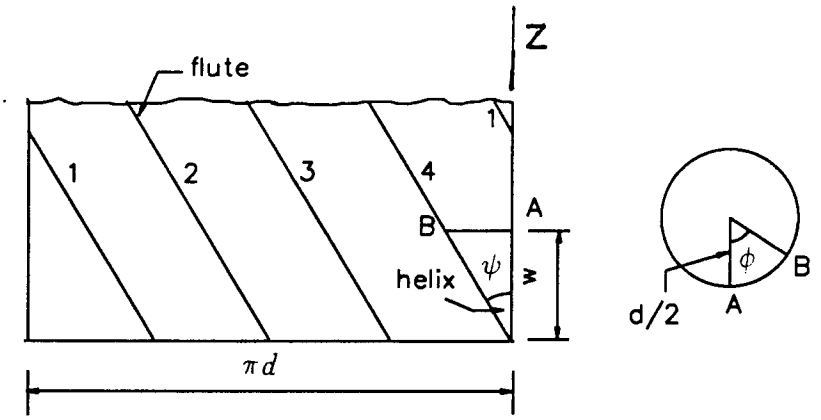

Figure 5.5: Developed surface of a four flute end mill having helix angle ψ

ϕ = swept angle, degree

From Eq. (5.3), angle θ which is required in the elemental force calculation along the cutting can be determined just by replacing w with the corresponding axial distance z ($< w$) of the element under consideration (see Fig. 5.5).

The above equations are sufficient to determine the elemental cutting forces, the resultant cutting force and its point of application on the end mill. In the following sections, these equations will be used to determine the forces to be applied on the end mill in the analytical and numerical shank stress analysis.

5.2.2 Analytical stress analysis in an end mill shank

In the literature, there is little information on the stress distribution in end mills. In this section an analytical solution for the determination of shank stresses in an end mill will be presented.

At the shank, which is far away from the application of the cutting forces, the stresses can be determined from the resultant cutting force F acting at a distance a shown in Fig. 5.2. The critical regions of the end mill for shank breakage could either be at the circular section close to the fixed end denoted by A in Fig. 5.2, or it could be across the flutes section close to the circular section denoted by B in the same figure.

Shank stress at the fixed end

At point A, the section is circular and the maximum bending stress can be determined from cantilever beam equations. If the resultant bending moment at this section is denoted by M_a, then the maximum bending stress for the circular section having diameter d is given by

$$\sigma_a = \frac{32M_a}{\pi d^3} \tag{5.4}$$

The maximum shear stress for the circular section of the end mill due to cutting torque T is given by

$$\tau = \frac{16T}{\pi d^3} \tag{5.5}$$

One of the important properties of cutting tool materials is their high hardness. With an increase in hardness, the rupture strength of materials reduces and they become brittle. Therefore the critical stress to be consider for shank failure of an end mill is the maximum (tensile) principal stress. This maximum principal stress can be determined from the normal and shear stresses using the relation

$$\sigma_1 = \sigma_a/2 + \sqrt{(\sigma_a/2)^2 + \tau^2} \tag{5.6}$$

The above equations, together with the mechanistic force distribution model given in Section 5.2.1, can be used to determine the stresses at the fixed end of the end mill.

The above equations will be used to determine the shank stresses of the end mill for the cutting conditions and tool geometry given in Figs. 5.1 and 5.2. The calculation at the fixed end for the resultant bending moment and torque, using the mechanistic model, is given in Jemal [40] (Appendix E.1). From these calculations the resultant bending moment at the fixed end is $M_a = 337$ kN-mm, and the resultant cutting torque is $T = 56.2$ kN-mm.

From the resultant moment and torque at the fixed end and from the stress equations given above, the critical stresses at point A of Fig. 5.2 can be calculated. The results of these calculations are summarized in Table 5.1.

Table 5.1: Stresses at the fixed end, point A,
of the end mill shown in Fig. 5.2, (MPa)

τ_a	σ_a	σ_1
17.5	209	210

Table 5.1 shows the difference between the bending stress σ_a and the principal stress σ_1 is only 1% and this means that the contribution of the shear stress towards the principal stress is negligible and therefore the bending stress is sufficient to predict shank breakage. These analytical results will be verified with numerical solutions in Section 5.2.3.

Shank stress at the end of the flute section

It is not easy to determine analytically the maximum bending stress at the end of the flute section closest to the circular section (point B of Fig. 5.2) because of the complicated shape of the flute. However, an approximate solution can be obtained by using the concept of equivalent diameter. The equivalent diameter is defined as the diameter of a circular bar which gives the same deflection as the end mill under the same cutting forces. Kops et al. [29] have used finite element end mill deflection

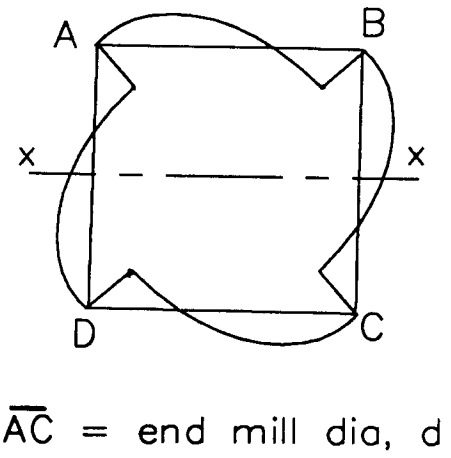

Figure 5.6: Determination of the equivalent diameter for four flute cutters

solutions and beam deflection equations to determine the equivalent diameter. An easier method of calculating the equivalent diameter for four flute cutters from Kops et al. [29] is to take the moment of inertia of the equivalent circular bar, $\pi d_e^4/64$, to be equal to the moment of inertia of a square section $ABCD$ shown in Fig. 5.6 about x-axis, $d^4/48$. Then this yields for the equivalent diameter the relation $d_e = .8d$.

When applying the equivalent diameter concept, it is imagined that the flute portion of the end mill is replaced by a circular section of the same length but smaller diameter, $d_e = .8d$, as shown in Fig. 5.7.

Once the flute section at point B is approximated by a circular section as shown in Fig. 5.7, the stresses can be determined in exactly similar manner as described above for shank stresses at the fixed end. The resultant moment and torque at section B are also given in Jemal [40] (Appendix E.1), and the value for the bending moment is $M_b = 231$ kN-mm, while the resultant cutting torque is still $T = 56.2$ kN-mm.

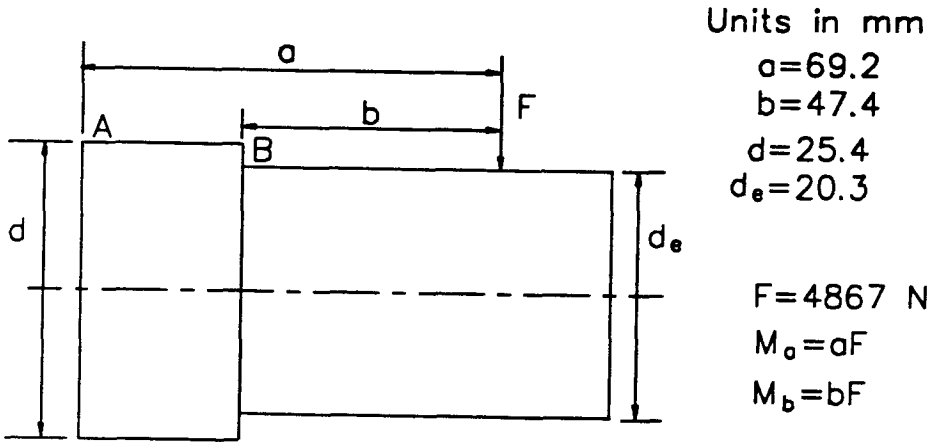

Figure 5.7: Representation of an end mill by an equivalent solid stepped bar

From the resultant moment and torque at section B and from the stress equations (5.4) to (5.6), the critical stresses at point B of Fig. 5.7 can be calculated. The results of this calculation are summarized in Table 5.2.

Table 5.2: Stresses at point B of the equivalent end mill shown in Fig. 5.7, (MPa)

τ_b	σ_b	σ_1
34	281	286

Table 5.2 shows the difference between the bending stress σ_b and the principal stress σ_1 is less than 2% and this means that the contribution of the shear stress towards the principal stress is negligible and therefore the bending stress is sufficient to predict shank breakage. The reason for the negligible effect of the shear stress on the shank principal stress is due to the large cutter axial length to cutter radius

ratio found in end mills. Comparison of the results in Tables 5.1 and 5.2 shows that the bending stress at the critical flute section is higher than that at the fixed end. This is because the effective section modulus of the flute section is much lower than the section modulus of the circular section. This lower section modulus at the flute section offsets the smaller bending moment at this section and makes it the most critical point for shank breakage of the end mill for the cutting condition and tool geometry considered in this analysis.

The analysis above can be extended to more complex end mills such as tapered end mills. However, in this case, or when the number of flutes of the cutter are different from four, the equivalent diameter has to be determined using finite element deflection solutions and beam deflection equations as described by Kops et al. [29].

In the next section numerical solutions will be used to verify the analytical solutions presented above for shank critical stresses.

5.2.3 Finite element stress analysis in an end mill shank

In the previous section analytical methods were used to determine critical shank stresses for the end mill geometry and cutting conditions shown in Figs. 5.1 and 5.2. In this section these analytical solutions will be verified using the finite element method (FEM) for the same cutting condition and tool geometry. The ANSYS [25] finite element software will be used in this analysis.

The finite element model of the end mill shown schematically in Fig. 5.1 will be developed from the geometry of the cross-section of one flute at the free end of the end mill shown in Fig. 5.8. In this figure the co-ordinate positions of nodal points that define the geometry of the cross-section are also given. From this cross-section the flutes of the end mill can be developed. The flute has a helix angle, therefore as

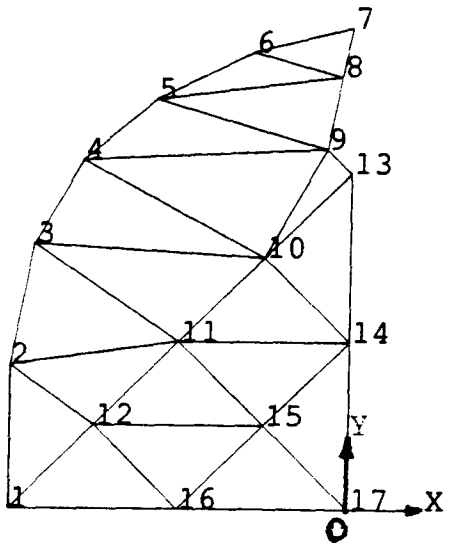

NODE	X (mm)	Y (mm)
1	-8.8900000	0.00000000
2	-8.8900000	3.8100000
3	-8.2550000	6.9850000
4	-6.9850000	9.2075000
5	-5.0800000	10.795000
6	-2.5400000	12.065000
7	0.00000000	12.700000
8	-0.25400000	11.430000
9	-0.63500000	9.5250000
10	-2.2225000	6.6675000
11	-4.4450000	4.4450000
12	-6.6675000	2.2225000
13	0.00000000	8.8900000
14	0.00000000	4.4450000
15	-2.2225000	2.2225000
16	-4.4450000	0.00000000
17	0.00000000	0.00000000

Figure 5.8: Cross-sectional geometry of one flute of a four flute cutter at $z = 0$, Fig. 5.1

we move along the axis of the end mill (z-axis) to generate new nodes, the flute cross-section shown in Fig. 5.8 has to be rotated. The amount of this rotation in degrees per axial distance can be calculated from Eq. 5.3 and is given by $\theta/z = 360 \tan \psi/(\pi d)$, where ψ is the helix angle and d is the diameter of the end mill. From this angle and the nodes of the flute cross-section shown in Fig. 5.8, the nodes for one flute model having any axial length c can be made. Fig. 5.1 shows, after the end of the flute section $z = c$, the end mill has a circular cross-section. This circular section can be made by adding nodes to the flute cross-section at $z = c$ (this cross-section has rotated by some angle relative to the free end's cross-section shown in Fig. 5.8) as shown in Fig. 5.9. From these nodes, the nodes for the circular portion of the end mill are generated. This results in nodes for one quarter of the four flute end mill, and to obtain its finite element model these nodes are filled with six-node triangular prism elements. These elements are selected because they take less computer time,

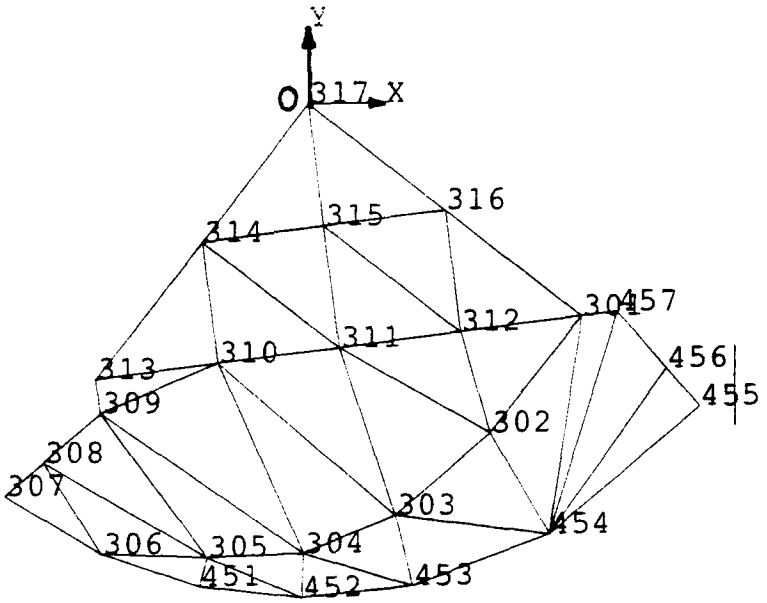

NODE	X(mm)	Y(mm)
301	6.99	-5.48
302	4.64	-8.48
303	2.18	-10.59
304	-.18	-11.55
305	-2.66	-11.62
306	-5.36	-11.51
307	-7.83	-9.99
308	-6.85	-9.15
309	-5.37	-7.88
310	-2.36	-6.61
311	0.755	-6.24
312	3.87	-5.86
313	-5.48	-6.99
314	-2.74	-3.49
315	0.377	-3.12
316	3.49	-2.74
317	0.000	0.000
451	-2.85	-12.37
452	-0.221	-12.69
453	2.64	-12.42
454	6.15	-11.10
455	9.99	-7.83
456	9.15	-6.85
457	7.88	-5.37

Figure 5.9: Circular cross-section of a flute at the beginning of the circular section at z=c, Fig. 5.1

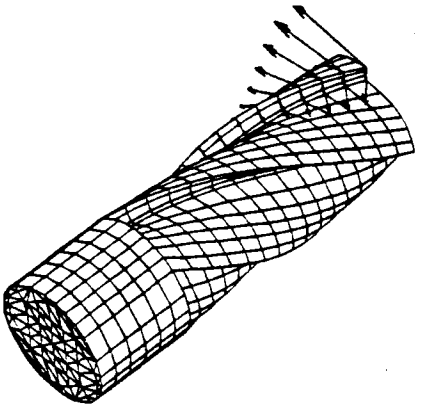

Figure 5.10: Finite element model of an end mill with elemental forces applied

and because the stress gradients in the shank are low so they can be modeled with sufficient accuracy using these linear elements. Finally, to obtain the complete finite element model of the four flute end mill, new nodes are generated from the nodes already defined by rotating them by 90^0 about the end mill axis four times and filling them with elements. This results in the finite element model of the complete end mill shown in Fig. 5.10. The finite element ANSYS input used to generate this end mill model is given in Jemal [40] (Appendix E.2). In this model the nodes and elements were generated manually and the numbering kept systematic in order to simplify the generation of elements and to enable identification of their position in the model when the boundary conditions are to be applied.

The concentrated forces to be applied along the cutting edge can be calculated from the mechanistic model described in Section 5.2.1. For the cutting condition and end mill geometry given in Figs. 5.1 and 5.2, An example of cutting force calculation

is given in Jemal [40] (Appendix E.1). The calculated tangential and radial cutting edge forces are then applied on the model as indicated in Fig. 5.10 to obtain the shank stresses in the end mill using the finite element approach.

Results

The finite element results obtained for shank stresses are discussed here. In Section 5.2.2 it was shown that for end mills, due to its large axial length to radius ratio, the contribution of the shear stress towards the maximum principal stress is negligible, and as a result the bending stress distribution is similar to the maximum bending stress distribution. The finite element solution for the bending stress distribution, σ_z, of the end mill is shown in Fig. 5.11. From this figure, the bending stresses are maximum at the fixed end, point A, and at the flute end close to the circular section, point B. Thus, this finite element solution predicts shank failure in these two regions.

Comparison of the stress results at points A and B of Fig. 5.11 shows the bending stress at the critical flute section is higher than that at the fixed end. This is because the effective section modulus of the flute section is much lower than the section modulus of the circular section at the fixed end. This lower section modulus at the flute section offsets the smaller bending moment at this section and makes it the most critical point for shank breakage. Another contribution to a higher stress at point B could be stress concentration. In our FEM end mill model the transition from the flute section to the circular section is not continuous and this results in higher stresses. The relative magnitude of the critical stresses at points A and B depends on the effective section modulus of the flute, the section modulus of the circular section, and the axial length of the circular section. Therefore, in general, it is not possible to say the stress in this region is always higher than in the other

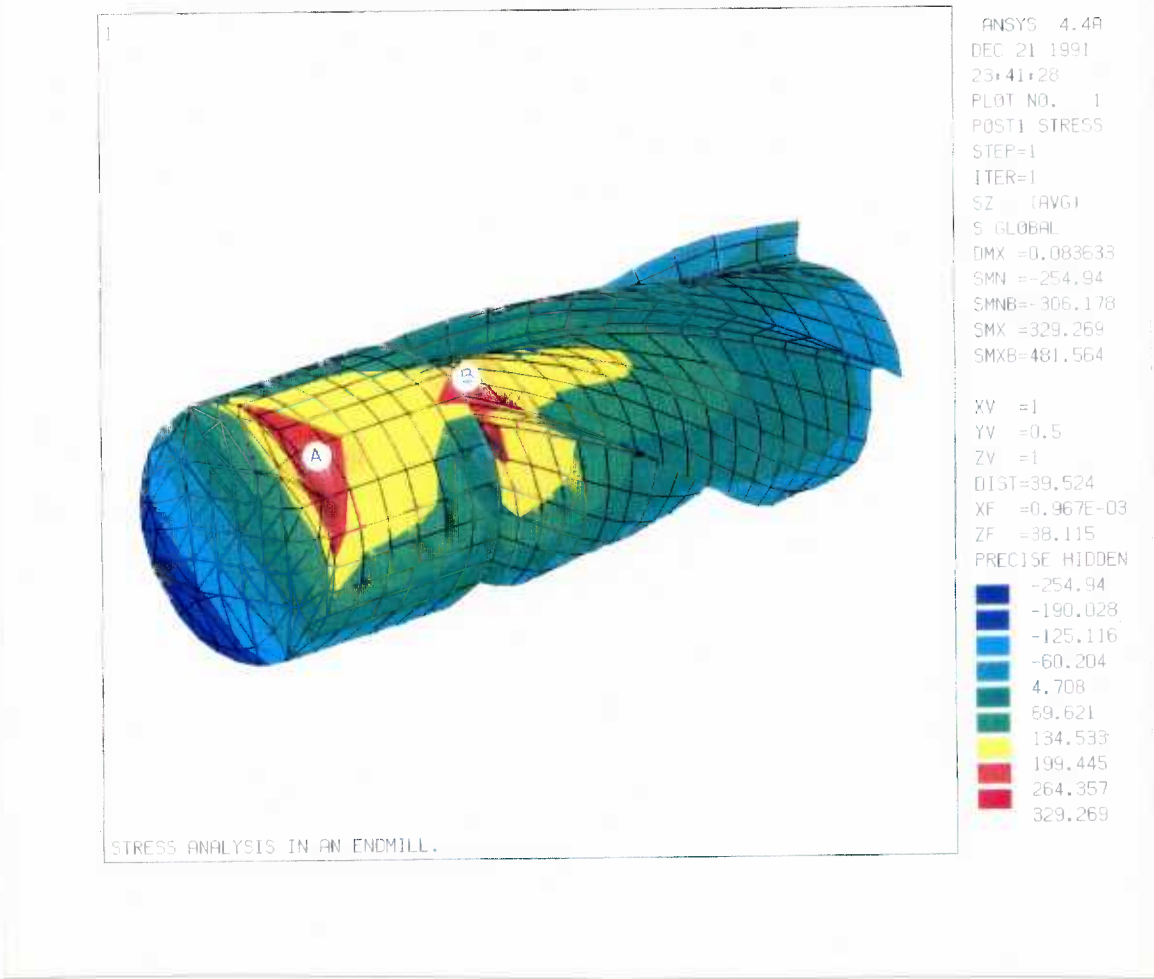

Figure 5.11: Finite element solution for end mill bending stress distribution

region. So in determining shank stresses both the critical regions shown in Fig. 5.11 must be checked.

5.2.4 Discussions and conclusions

In the previous sections analytical critical shank stresses for an end mill were determined, and for the same cutting condition and tool geometry finite element bending stress distribution were obtained. The analytical results are summarized in Tables 5.1 and 5.2, and the finite element solution is shown in Fig. 5.11. Both of the analytical results lie within the range of values corresponding to the red coloured regions of the finite element solution and therefore they are in good agreement. Calculations show that the difference in the critical stresses between the two solutions are less than 9%, and this verifies the applicability of the analytical approach presented in Section 5.2.2. Improved solution could be obtained by reducing the element size used in the finite element analysis. However, this lead to the need for larger computer memory and time so a compromise element size was taken.

The analysis above gives the location for shank breakage of end mills. This result could be compared with common types of end mill shank breakage observed during the manufacture of turbine components by Bouse [33] of General Electric Company which is shown in Fig. 5.12. Comparison of this figure with Fig. 5.11 shows the solutions obtained in this study correctly predict the location of end mill shank in-service breakages.

From the results obtained, the allowable cutting force F_{all} corresponding to the allowable tensile stress σ_{all} of the tool material could be obtained from the linear force-stress relationship. This relation gives $F_{all} = (F/\sigma)\sigma_{all}$, where F and σ are the resultant cutting force and critical tensile stress relations obtained in this study for

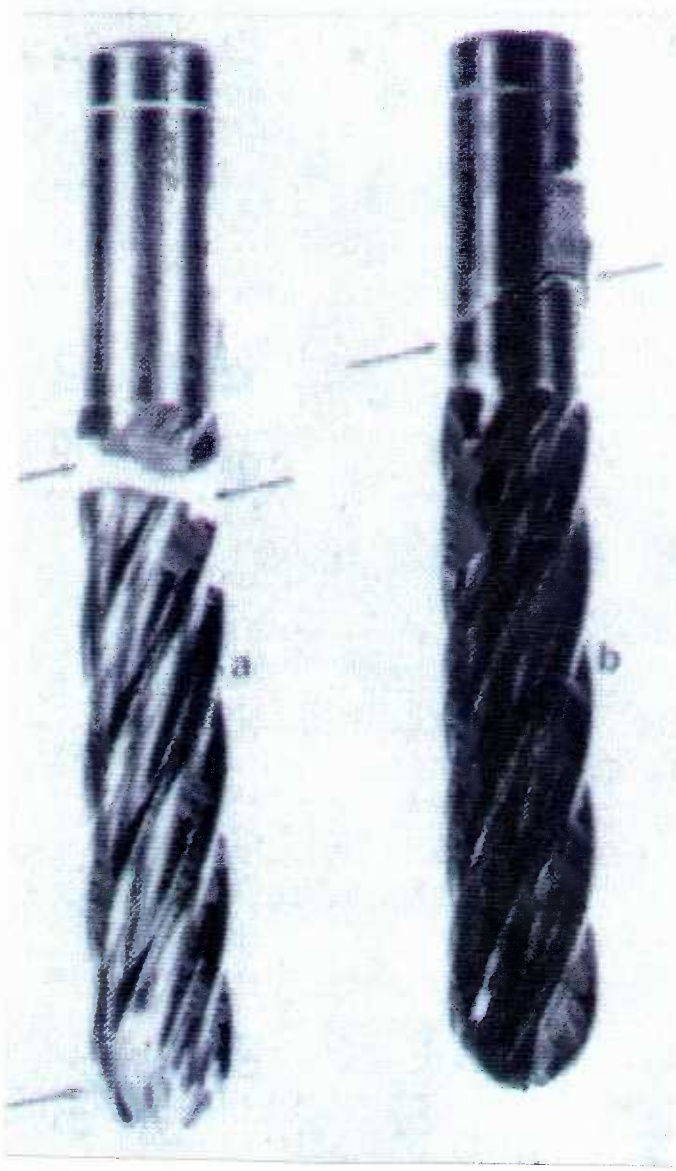

Figure 5.12: Common types of end mill shank breakages, Bouse [33]

the cutting condition and tool geometry considered. This allowable force gives the optimum force for maximum production without the danger of tool shank breakage.

5.3 End mill flute stresses

The general objective of this study to investigate how far the analytical solutions can go in determining the critical end mill stresses. In the previous sections, an analytical approach was presented which was used to determine shank stresses, and it was found that the solutions obtained are in reasonable agreement with numerical results. The second critical region for an end mill failure is its flute. In this section end mill flute stresses will be considered.

Comparison will be made between the two-dimensional cutting tool stress solutions already obtained in Section 4.3 and finite element solution of a *straight* end mill flute for the same wedge angle of 62^0 and boundary load distribution shown in Fig. 4.2. The simple straight flute is selected because it is the most likely end mill flute geometry where its stress distribution could be approximated by the two-dimensional solution. If the two solutions are similar then helical end mills will be considered, but if the solutions are different then it can be concluded that end mill flute stresses can not be determined from two dimensional solutions and their solutions have to be obtained using three-dimensional numerical methods.

The same procedure as described in Section 5.2.3 was used to develop the finite element model of the flute shown in Fig. 5.13. Since in flute stress analysis the concern is for local stresses, only two flutes of a four flute end mill near the loaded region was considered. The ANSYS input used in generating the model and determining the stress distribution is given in Jemal [40] (Appendix F.1). The boundary loads were applied on face $ABCD$ where AB is the active cutting edge (also equal to the axial

depth of cut), while AD and BC are equal to the chip-tool contact length. The applied distributed loads along any plane perpendicular to the cutting edge AB are identical and are as shown in Fig. 4.2. The chip-tool contact length for this boundary load distribution is 1 mm. This length denoted by BC and AD in Fig 5.13 is divided into 20 elements of length 0.05 mm. The length of the elements along the cutting edge is 0.5 mm. The boundary normal stresses were calculated at each of the elements along the contact length. The normal stresses were applied directly as pressures on the element faces. The shear stresses at each element was first converted to forces by multiplying them by the element area (0.025 mm^2 in this case) and they were applied at the nodes. Very small elements were used to accurately represent the distributed shear and normal boundary load distribution shown in Fig. 4.2.

Fig. 5.13 also shows the minimum principal stress distribution in the loaded region. This figure clearly shows the increase in the magnitude of the minimum principal stress on the flank and rake faces when moving towards the cutting edge. The minimum compressive stress value given in this figure agrees with the two-dimensional solution given in Fig. 4.7. Therefore, the critical cutting edge stress for straight end mill flutes can be determined from two-dimensional solutions. It is also interesting to see how the stress distribution is uniform along the cutting edge, and how the stress variations are localized to the loaded region alone. This observation verifies the validity of considering only a portion of the end mill in flute stress analysis.

The rake face maximum principal stress distribution of the flute model is compared with the two-dimensional result in Fig. 5.14. From this figure the critical maximum principal stress in the end mill flute is less (by 35%) than that in the two-dimensional cutter. Therefore, two-dimensional solutions cannot be used to accurately determine the maximum principal stress in the loaded region of an end mill flute. However, they

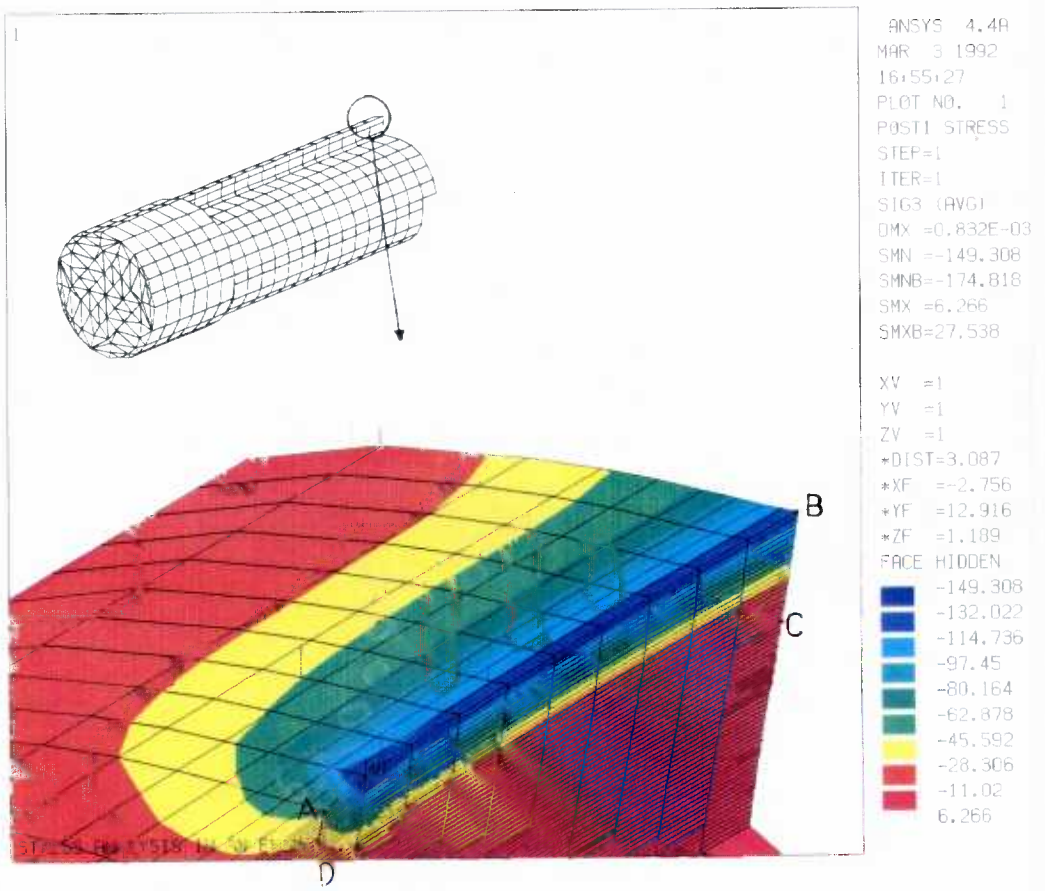

Figure 5.13: End mill FEM flute model and its minimum principal stress σ_3 distribution for the boundary load distribution shown in Fig. 4.2

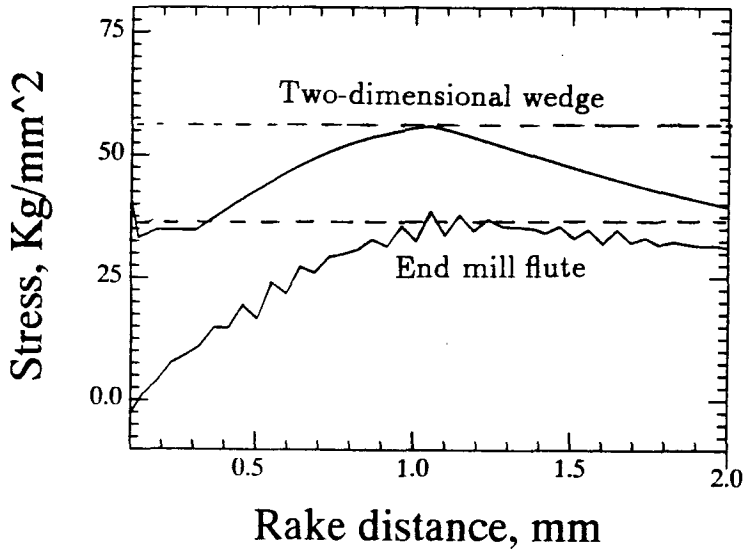

Figure 5.14: Comparison of maximum principal stress distributions σ_1 for a two dimensional wedge and an end mill flute for the boundary load distribution shown in Fig. 4.2

can give an upper bound value as shown in Fig. 5.14. Fig. 5.14 also indicates that in both two-dimensional wedge and end mill flute, the maximum principal stresses reach their peak at the end of chip-tool contact (in this case at $l_c = 1$ mm).

The reason for the difference between the end mill flute and the two-dimensional cutting tool solutions observed in Fig. 5.14 may be explained as follows: In two-dimensional cutting tools the planes perpendicular to the cutting edge (side faces of the tool) are free from resisting stresses. On the other hand, in the end mill flute, resisting stresses act on the sides faces and provides support for the cutting edge. This effect results in lower deflection of the loaded region and lower tensile stress at the end of chip-tool contact as shown in Fig. 5.14.

A finite element solution was also obtained to see the effect of change in axial depth of cut AB on the flute stress distribution. Results of this flute stress distribution for

the same boundary load distribution, but different axial depth of cut show similar stresses. From this result, flute failures and shank failures could be compared for the end mill geometry given in Fig. 5.1. For the axial depth considered in Fig. 5.13, the maximum tensile stress in the flute is found to be four times the stress at the fixed end. Therefore, with further increase in radial depth of cut, the flute fails first compared to the shank. If, however, the axial depth of cut is increased to more than four times, then the shank stress becomes higher, and in this case with further increase in radial depth of cut the shank fails first. At moderate axial depth of cut, failures at either the shank or flute is possible.

The results from the two methods for the maximum principal stresses as shown above are different even for the simple straight end mill, and therefore when these stresses are required in the complex *helical* end mill a three-dimensional numerical solution has to be used.

5.4 End mill cutting edge stresses

In the previous section stresses for straight flute end mill were considered. These results show two dimensional solutions can be used to determine cutting edge stresses in straight end mill flutes. To complete the investigation for the possible use of analytical solutions in end mill stress analysis, the effect of the shape of the cutting edge on the stress distribution is considered in this section. For this analytical two-dimensional cutting edge stresses will be compared with numerical stresses for a curved cutting edge.

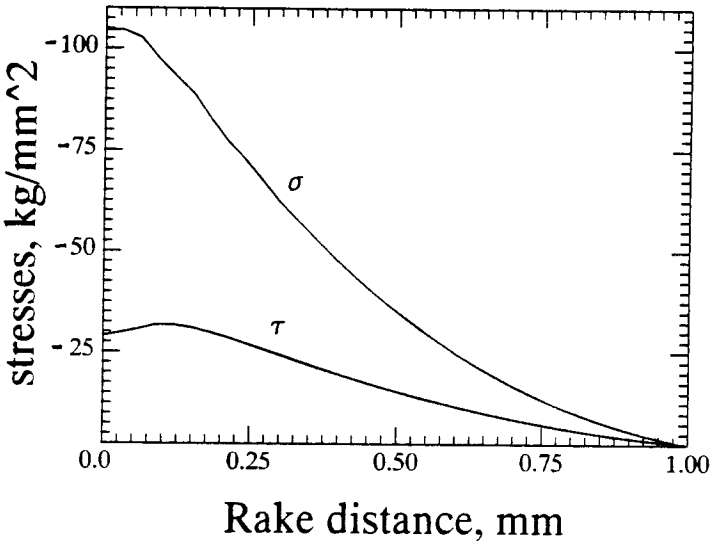

Figure 5.15: Boundary stress distribution considered for cutting edge stress analysis

5.4.1 End mill cutting edge stresses using elasticity

In this section the analytical equations for cutting edge stresses will be discussed. Then as an example, this equations will be used to determine the cutting edge stresses for the boundary load distribution shown in Fig. 5.15 and a wedge angle of a standard 1 inch end mill. The analytical solution to be found will then be compared with finite element solutions for the same boundary load distribution and wedge angle in order to verify the applicability of the analytical solutions in cutting edge stress analysis.

Analytical solution for the cutting edge stresses are discussed in Section 2.5.1. The solution for the radial rake face stress is given by Eq. (2.40) and is

$$\sigma_r = \frac{\alpha}{\tan\alpha - \alpha}|\sigma_0| - \frac{\tan\alpha(\alpha\tan\alpha + 1) - \alpha}{(\tan\alpha - \alpha)\tan\alpha}|\tau_0| \tag{5.7}$$

where,

σ_r = radial stress parallel to the rake face

α = wedge angle, radians

$|\sigma_0|$ = magnitude of normal stress at the cutting edge on the rake face

$|\tau_0|$ = magnitude of the shear stress at the cutting edge on the rake face

The wedge angle of the end mill to be analyzed is $\alpha = 76^o$ and it is measured from a standard 1 inch diameter end mill. The boundary stress distribution to be applied on the tool is the high speed photoelastic boundary (Section 2.3.2) shown in Fig. 5.15. For the wedge angle considered, from Eq. (5.7), the radial stress at the cutting edge is given by $\sigma_r = .5|\sigma_0| - 2.2|\tau_0|$. Once this stress component is determined, the principal stresses can be determined using Eq. (3.24). These stress results at the cutting edge are summarized in Table 5.3.

Table 5.3: Cutting edge stresses for the boundary of Fig. 5.15 and wedge angle of 76^0, (kg/mm^2)

σ_r	σ_2	σ_3	$SI = \sigma_1 - \sigma_3$
-12	-4	-113	113

In Table 5.3 since both the principal stresses in the cutting tool plane are negative, the maximum principal stress for the plane stress problem $\sigma_1 = 0$ was taken.

Examination of Eq. (5.7) shows that the cutting edge stresses are functions of the applied normal and shear stress at the cutting edge and the wedge angle only. The magnitude of the shear stress at the cutting edge on the rake face is close to the yield shear strength of the workpiece material being machined and is independent of the cutting conditions. The normal stress at the cutting edge on the rake face is approximately related to the shear stress at the cutting edge. This relation by Loladze [37] is given by Eq. (2.25) in Section (2.3.3) which is

$$\sigma_0 = 2k(1/2 + \pi/4 - \gamma) \tag{5.8}$$

where k is the yield shear strength of the workpiece material and γ is the rake angle of the tool. Since the rake angle is directly related to the wedge angle for a given clearance angle, the applied normal stress is a function of only the yield shear strength of the workpiece material and the wedge angle. This means that for the same work material and wedge angle, a change in cutting conditions or change in tool geometry (meaning change in cutting forces) do not result in a change in cutting edge stresses. For the same work material and tool wedge angle, a change in cutting conditions results in a change in chip-tool contact length or a change in the shape of the boundary load distribution while the boundary stresses at the cutting edge remain approximately constant.

5.4.2 End mill cutting edge stresses using FEM

In the previous section cutting edge stresses using elasticity solutions were considered. In this section the elasticity solutions obtained will be verified with finite element results for the same boundary load distribution shown in Fig. 5.15 and wedge angle of 76^0.

The finite element results shown in Fig. 5.13 show that the flute stresses, and more so the cutting edge stresses, are localized and therefore when stresses in these regions are required, only a portion of the end mill flute near the loaded region need be considered for the finite element model.

The same procedure as described in Section 5.2.3 was used to develop the finite element model of the flute shown in Fig. 5.16, which is a portion of the ball end of the end mill shown schematically in Fig. 5.17. In this model because of the steep stress gradient in the loaded region finer elements were used (an average area of 0.0125 mm^2). The ANSYS input used in generating the model and determining the stress

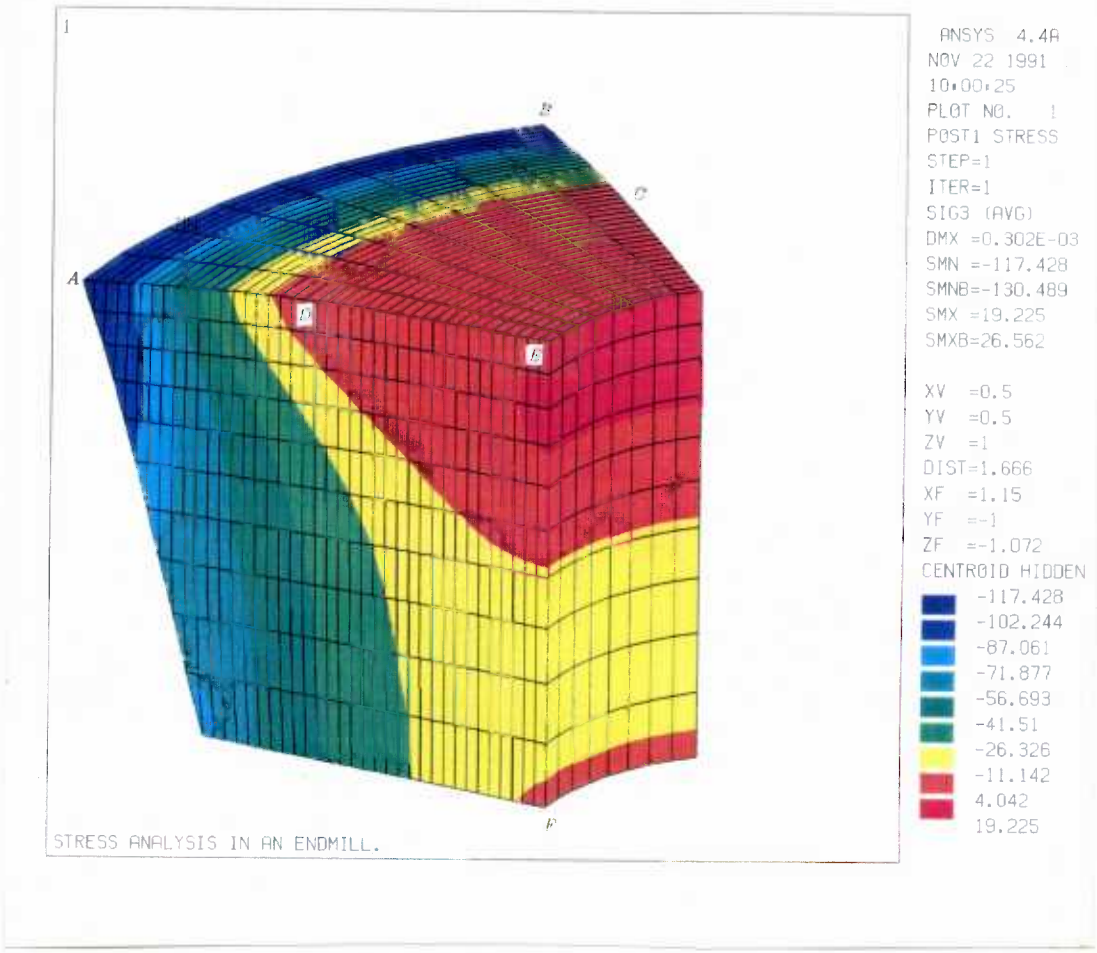

Figure 5.16: Finite element solution for the minimum principal stress σ_3 at the cutting edge

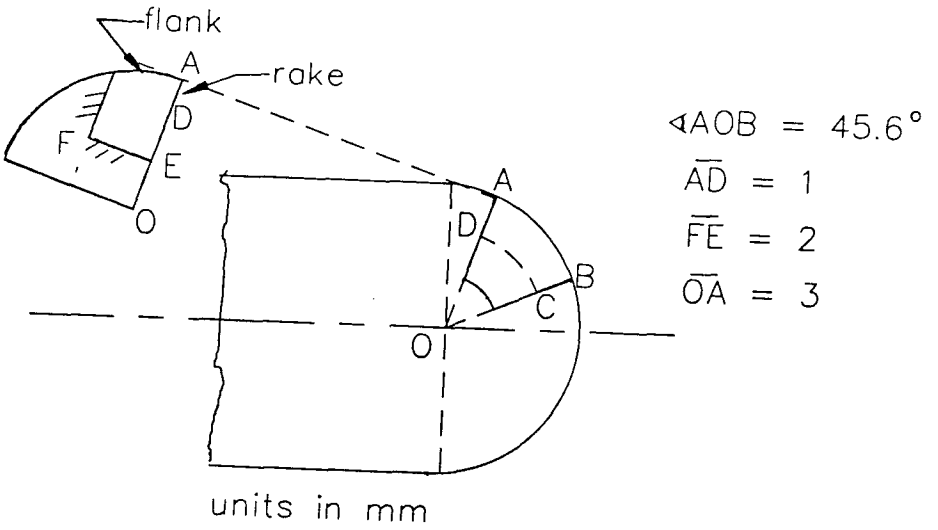

Figure 5.17: Schematic diagram showing the portion of the ball end mill considered for cutting edge FEM model

distribution is given in Jemal [40] (Appendix F.2). The boundary loads were applied on face $ABCD$ where AB is the circular cutting edge and AD and BC are equal to the chip-tool contact length. The applied distributed loads along any radial plane perpendicular to the cutting edge AB are taken to be identical and are shown in Fig. 5.15. The same procedure were used to apply the boundary load distributions on the element faces as described in the straight flute finite element stress analysis.

Fig. 5.16 also shows the minimum principal stress distribution near the cutting edge. The minimum principal stress occurs at the cutting edge and has the value $\sigma_3 = -117$ kg/mm^2. The other stress which is responsible for end mill cutting edge failure is the maximum shear stress. Twice the maximum shear stress distribution close to the cutting edge is shown in Fig. 5.18. From this figure the maximum shear stress in the loaded region occurs at the cutting edge and twice the maximum stress

has the value $2\tau_{max} = SI = 112$ kg/mm^2.

A comparison of the above numerical solutions with analytical results given in Table 5.3 show less than 4% difference and therefore they are in very good agreement. Thus, the analytical solution can be used to determine cutting edge stresses, and end mill cutting edge failures could be explained by the two-dimensional cutting tool failure analysis discussed in Section 4.5.

The rake face maximum principal stress distribution of the ball end model is compared with the two-dimensional result in Fig. 5.19. From this figure the maximum principal stress in the ball end is much less than the two-dimensional solution. Therefore, two-dimensional solutions cannot be used to accurately determine the maximum principal stress in the loaded region of the ball end of an end mill flute. However, they can give an upper bound estimate as shown in Fig. 5.19.

5.5 Conclusions

An analytical approach for shank stress was presented and the solution obtained was compared with finite element solution. Good agreement was obtained. Therefore, shank stresses can be determined using analytical solutions. The critical regions for shank failures obtained from these solutions were also found to reasonably predict the location of end mill shank failures observed in practice.

The possible use of two-dimensional solutions to determine maximum principal stresses in an end mill flute was studied. It was found that for the same load distribution and wedge angle, the maximum stress in the two-dimensional cutting tool is much higher than that in the end mill flute. Therefore, when accurate stress predicition near the end of chip-tool contact of an end mill is required, a three-dimensional numerical solution should be employed. If only approximate values are required,

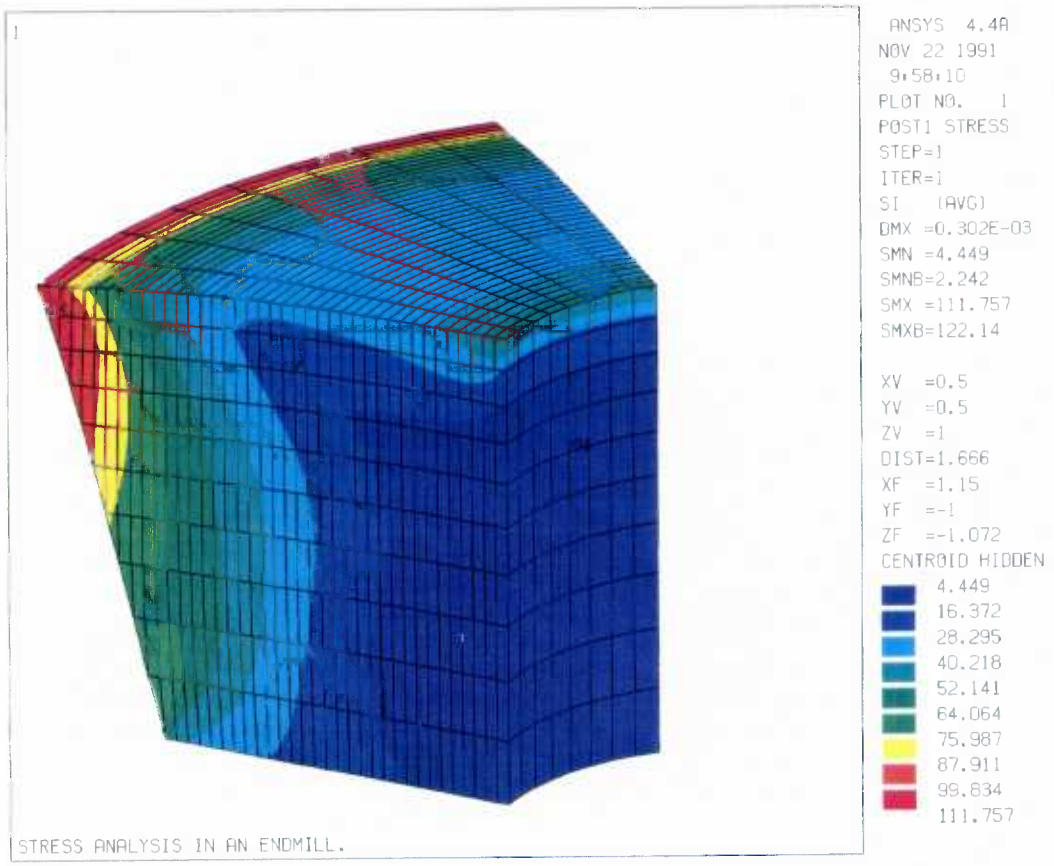

Figure 5.18: Finite element solution for the maximum shear stress at the cutting edge

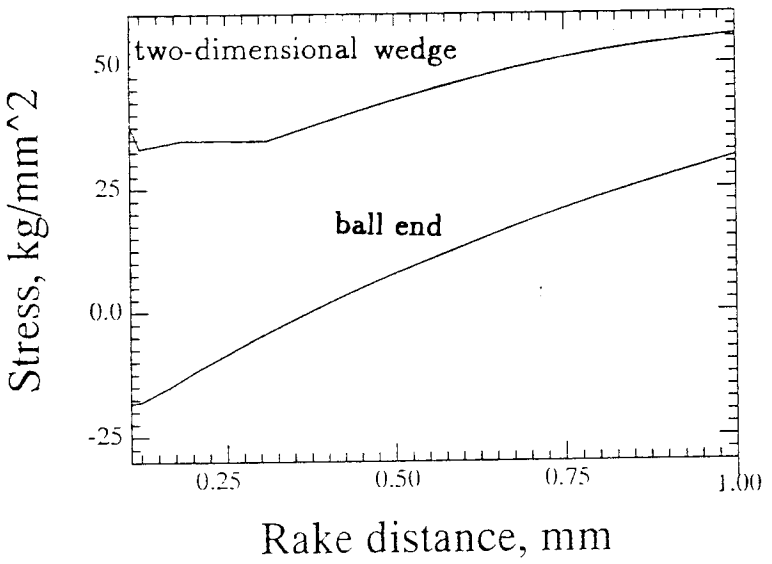

Figure 5.19: Comparison of maximum principal stress distributions σ_1 for a two-dimensional wedge and a ball end mill

however, then the two-dimensional analytical solution may be used to provide upper bound estimates.

The second critical region of an end mill flute is its cutting edge. Analytical and finite element cutting edge stress solutions were compared, and it was found that there is good agreement. Therefore, end mill cutting edge stresses can be determined using analytical solutions.

Chapter 6

Concluding Remarks

6.1 Summary

In this study, the stresses within cutting tools (orthogonal cutting tool and an end mill) were analyzed. The stress distributions from the analytical solutions were compared with numerical solutions in order to investigate the possible use of analytical solutions in cutting tool stress analysis. The analytical and numerical results obtained for the location and modes of tool failure were also compared with observed cutting tool in-service failure in order to see the correlation between predictions and actual cutting tool failures.

6.2 Conclusions

For accurate determination of the stress distribution in a cutting tool, the actual mechanical and thermal boundary loads are required. Because of the complexity of the cutting process, the knowledge of the boundary load distributions and therefore the stress distribution in the cutting tool is approximate. In this study stresses due to mechanical loads only are considered and these stresses can be superposed on the

thermal stresses to obtain the overall stress distribution in the cutting tool.

From the results obtained in the previous chapters, the following conclusions can be made

- Previous analytical stress distribution results near the end of chip tool contact were shown to be incorrect. This was found to be due to the direct use of the infinite wedge solution to determine stresses in the loaded region of the cutting tool.

- An analytical stress distribution in an orthogonal cutting tool which agrees with numerical and previous experimental stress distribution results was obtained. This was done by satisfying the boundary condition beyond the loaded region.

- Analytical stresses at the critical shank sections of an end mill were found to agree well with numerical solutions. This indicates the applicability of analytical methods in shank stress analysis.

- Comparison of two-dimensional stress distribution with numerical solution of an end mill flute show good agreement at the cutting edge, but at the end of chip-tool contact the two-dimensional solution gave a significantly higher critical maximum principal stress.

- The analytical and numerical prediction of cutting tool (orthogonal cutting tool and end mill) failure locations and modes of failure were found to correlate well with observed cutting tool in-service failure.

From the results obtained in the previous chapters, the following conclusions can be made of the stress distributions and deformations in cutting tools

- During cutting, the loaded region of a cutting tool deforms, causing shortening of the flank face close to the cutting edge and bending of the rake face at a point near the end of chip-tool contact.

- The shortening of the flank face results in the critical minimum principal stress to be in this face, close to the cutting edge. The rake face bending about the point near the end of chip-tool contact results in the critical maximum principal stress to be at this point. Within the cutting tool the principal stresses are within these two extreme values, increasing algebraically from the flank face to the rake face.

- The magnitude of the critical compressive stress is much higher than the critical tensile stress. Since the maximum shear stresses on free surfaces (at the critical points) is proportional to the non zero principal stress, the critical maximum shear stress occurs at the flank face near the cutting edge.

- With increase in cutting forces the critical maximum principal stress results in initiation of cracks near the end of chip-tool contact and final fracture of the whole loaded region of the cutting tool. The critical minimum principal stress results in permanent deformation of the cutting edge, while the critical maximum shear stress results in chipping of the cutting edge.

- For both low and high speed photoelastic boundary load distributions, for the geometries of the cutting wedge considered, the critical maximum principal stress occurs at the end of chip-tool contact.

- The magnitude of the critical maximum principal stress, minimum principal and maximum shear stress decrease with increase in the wedge angle of the tool.

- When prediction of stresses further from the loaded region of the cutting tool are required the cantilever beam equations can be used to determine the maximum principal stress which may cause cutting tool fracture.

6.3 Recommendations

The following recommendation are suggested for future work in order get an improved approximation of the stress distribution in cutting tools.

- The cutting tool stress distribution due to flank loading should be included in future cutting tool stress analysis. In this study the cutting tool was assumed to be sharp with no flank face loads. The stresses due to flank face loads could be easily added by using the same procedure used for the rake face loads and superposing the results. The stress distributions due to the flank and rake face loads have opposing effects and therefore when the flank face stresses are included the magnitude of the stresses should be lower. Thus the stress distribution obtained in this study is the worse case. However, to get an improved solution the stress distribution due to flank loading should also be considered. Unfortunately, experimental flank face boundary load distribution data are sparse and therefore the shape of the distribution must be assumed to be similar to the rake face boundary load distribution but with smaller average loads and smaller contact length.

- The cutting tool stress distribution due to thermal effects should be included in future cutting tool stress analysis. In this study the temperature effects were not considered. The temperature effects should be considered in order to explain failures due to thermal effects observed in cutting tools at higher cutting speeds.

To accomplish this, the boundary temperature distribution on rake and flank faces must be known or assumed. The temperature distribution along these faces can be estimated from the inserted thermocouple technique (Chao [30], Kusters [35]) or using the metallographic method (Smart at el. [31]) where the temperature distributions are deduced from the structural change of the high speed tool. Based on this temperature distribution, the thermal stresses could be estimated and then superposed on the mechanical stress distribution to enable prediction of cutting tool failure and stress levels at higher cutting speeds.

- Future cutting tool stress analysis results should be verified experimentally. In this study, the conclusions reached for cutting tool failures was found to correlate well with observed in-service failures of cutting tools. However, to quantitatively predict tool failures it is necessary to compare the value of the predicted critical stresses at cutting tool failure with the strength of the cutting tool material. For this analysis, the cutting tool strength at the temperature that the tool experiences, as determined by Kreimer [39], should be used. It will also be important to compare the predicted location for initiation of cracks on the rake face with the location observed from actual cutting tool failures. Finally, when doing this analysis it is important to note, as discussed by Shaw [38], that the variability in the strength of cutting tool materials is large and therefore the agreement between the predicted critical stress values and the tool material strength might not be that close.

Bibliography

[1] M. M. Frocht, *Photoelasticity*, John Wiley & Sons, Inc., Vol. I & II, 1948.

[2] S. Kaldor, *A Common Denominator for Optimal Cutting Tool Geometry*, Annals of the CIRP, Vol. 35, No. 1, pp. 41-44, 1986.

[3] H. Chandrasekaran, *Tool Fracture Model for Peripheral Milling*, NAMRC, Vol. 10, pp. 15-20, 1982.

[4] J. H. Michell, *proc. London Math. Soc.*, Vol. 31, p. 100, 1899.

[5] S. P. Timoshenko and J. N. Goodier, *Theory of Elasticity*, McGraw-Hill, 1982.

[6] F. R. Archibald, *Analysis of the Stresses in a Cutting Tool*, Trans. ASME, pp. 1149-1154, August 1956.

[7] A. I. Betaneli, *A Method of Calculating Tool Strength*, Russian Engineering Journal, Vol. 45, pp. 71-75, 1965.

[8] R. D. Cook, D. S. Malkus and M. E. Plesha, *Concepts and Applications of Finite Element Analysis*, John Wiley & Sons, 1989.

[9] C. J. Tranter, *The Use of the Mellin Transform in Finding the Stress Distribution in an Infinite Wedge*, Q. Jl. Mech. appl. Math., Vol. 1, p. 125, 1948.

[10] P. F. Thomason, *The Stress Distribution in a Wedge-Shaped Metal-Cutting tool for Triangular Distributions of Load on the Rake-Face Contact Length*, Journal of Mechanical Engineering Science, Vol. 16, No. 6, pp. 418-424, 1974.

[11] G. B. Airy, *Brit. Assoc. Advan. Sci. Rept.*, 1862.

[12] M. C. Shaw, *Metal Cutting Principles*, Clarendon Press, Oxford, pp. 125-129, 1984.

[13] E. M. Trent, *Metal Cutting*, Butterworths, 1977.

[14] G. Boothroyd, *Fundamentals of Metal Machining*, Edward Arnold Ltd., 1965.

[15] S. Kato, K. Yamaguchi and M. Yamada, *Stress Distribution at the Interface Between Tool and Chip in Machining*, Journal of Engineering for Industry, Trans. ASME, pp. 683-689, May 1972.

[16] G. Barrow, W. Graham, T. Kurimoto and Y. F. Leong, *Determination of Rake Face Stress Distribution in Orthogonal Machining*, Int. J. Mach. Tool Des. Res., Vol. 22, No. 1, pp 75-85. 1982.

[17] T. H. C. Childs and M. I. Mahdi, *On the Stress Distribution Between the Chip and Tool During Metal Turning*, Annals of the CIRP, Vol. 38, No. 1, pp. 55-58, 1989.

[18] E. Usui, *A Photoelastic Analysis of Machining Stresses*, Journal of Engineering for Industry, Trans. of ASME, pp. 303-308, November 1960.

[19] H. Chandrasekaran and D. V. Kapoor, *Photoelastic Analysis of Tool-Chip Interface Stresses*, Journal of Engineering for Industry, Trans. of ASME, pp. 495-502, November 1965.

[20] E. Amini, *Photoelastic Analysis of Stresses and Forces in Steady Cutting*, Journal of Strain Analysis, Vol. 3, No. 3, pp 206-213, 1968.

[21] M. M. Ahmad, R. T. Derricott and W. A. Draper, *A Photoelastic Analysis of the Stresses in Double Rake Cutting Tools*, Int. J. Mach. Tools Manufact., Vol. 29, No. 2, pp. 185-195, 1989.

[22] T. N. Loladze, *Problems of Determining Stresses at Cutting Edge of a Tool*, Proceedings of the Seventh Congress on Theoretical and Applied Mechanics, Bombay, India, pp. 323-348, 1961.

[23] W. Johnson and P. B. Mellor, *Plasticity for Mechanical Engineers*, D. Van Nostrand Company Ltd., pp 259-264, 1962.

[24] N. N. Zorev, *Metal Cutting Mechanics*, Pergamon Press, p. 73, 1966.

[25] ANSYS, *Engineering Analysis Systems Manual*, Vol. I & II, Swanson Analysis Systems, Inc., P. O. Box 65, Houston.

[26] M. E. Merchant, *Journal of Applied Physics*, Vol. 16, No. 5, pp. 267-324, May 1945.

[27] J. Tlusty, *Chipping and Breakage of Carbide Tools*, Journal of Engineering for Industry, Vol. 100, No. 4, pp. 403-412, 1978.

[28] W. A. Kline, R. E. DeVor, and J. R. Lindberg, *The prediction of cutting forces in End Milling with Application to cornering Cuts*, Int. J. Mach. Tool Des. Res., Vol. 22, No. 1, pp. 7-22, 1982.

[29] L. Kops and D. T. Vo, *Determination of The Equivalent Diameter of an End Mill Based on its Compliance*, Annals of the CIRP, Vol. 39, No. 1, pp. 93-96, 1990.

[30] B. T. Chao and K. J. Trigger, *Temperature Distribution at the Tool-Chip Interface in Metal Cutting*, Journal of Engineering for Industry, Trans. of ASME, pp. 139-151, May 1959.

[31] E. F. Smart and E. M. Trent, *Int. J. Prod. Res.*, Vol. 13, No. 3, p. 265, 1975.

[32] William H. Press et al., *Numerical Recipes*, The Art of Scientific Computing (Fortran Version), Cambridge University Press, p. 31, 1986.

[33] G. K. Bouse, *Metallurgical Investigation of Several High Speed Tool Steel Failures*, Cutting Tool Materials. American Society for Metals. pp. 77-92, 1981.

[34] E. M. Trent, *Proc. Int. Conf. M.T.D.R,* Manchester, p. 629, 1967.

[35] K. J. Kusters, *Industrie Anzeiger*, Vol. 89, p. 1337, 1956.

[36] P. K. Wright and E. M. Trent, *Metals Technology*, Vol. 1, No. 13, 1974.

[37] T. N. Loladze, *Requirements of Tool Materials*, Proceedings of the 9^{th} MTDR Conference, Pergamon Press, Manchester, England, 1968.

[38] M. C. Shaw and T. C. Ramaraj, *Brittle fracture of cutting tools*, Annals of the CIRP Vol. 38, No. 1, 1989.

[39] G. S. Kreimer, *Strength of Hard Alloys*, Scientific research Institute for Hard Alloys, Moscow, translated from Russian, Consultants Bureau, New York, 1968.

[40] G. Jemal, *Investigation of Stresses in Cutting Tools*, University of British Columbia, Department of Mechanical Engineering, Stress Analysis and Biomechanics Laboratory (SABIL) Report 92-1, April, 1992.